Doctoral Thesis

Stretch and shrink flanging of AA2024-T3 sheet by single point incremental forming

José Andrés López Fernández

Dpto. De Ingeniería Mecánica y Fabricación
Escuela Técnica Superior de Ingeniería
Universidad de Sevilla

Sevilla, 2021

José Andrés López Fernández

Stretch and shrink flanging of AA2024-T3 sheet by single point incremental forming

2021

Doctoral Thesis

Stretch and shrink flanging of AA2024-T3 sheet by single point incremental forming

José Andrés López Fernández

Supervisors:

Dr. Carpóforo Vallellano Martín
Dr. Gabriel Centeno Báez

Dpto. de Ingeniería Mecánica y Fabricación
Escuela Técnica Superior de Ingeniería
Avda. De los Descubrimientos s/n. 41092
Universidad de Sevilla

Sevilla, 2021

A mi familia

Agradecimientos

Quiero agradecer a mi familia, amigos, directores de tesis y compañeros el apoyo prestado sin el cual no habría podido acabar este trabajo.

Resumen

El rebordeado de flancos es un proceso de conformado de chapa ampliamente usado en industrias como la aeronáutica o la automobilistica para la fabricación de componentes estructurales de chapa delgada. Este tipo de proceso se suele realizar sobre metal, normalmente aplicando presion a través de una almohadilla de goma o directamente usando una matriz y un punzón metálicos. Estos dos métodos tienen la ventaja de ser rápidos y rentables en la fabricación de grandes lotes. Sin embargo, son cada vez más los trabajos que estudian el uso de procesos no convencionales, como el conformado incremental monopunto o SPIF (por sus siglas en inglés), en aplicaciones tales como el rebordeado de agujeros, aprovechando así la flexibilidad y el ahorro de utillaje que proporciona esta técnica.

En este contexto, esta tesis presenta un estudio sobre el conformado incremental monopunto aplicado al rebordeado de flancos abiertos de AA2024-T3 para geometrías cóncavas y convexas. Este trabajo se centra en la evaluación de la conformabilidad en el diagrama límite de conformado (FLD), teniendo en cuenta differentes parámetros tales como el radio principal del flanco, la velocidad de giro de la herramienta o el tamaño de la misma. Así mismo, se han obtenido las ventanas de proceso para las dos geometrías propuestas, analizando las características de los diferentes modos de fallo.

Además, se ha usado un modelo numérico junto con un marco teórico basados en el criterio de plasticidad de Barlat 89 para analizar la conformabilidad de los flancos cóncavos en el espacio de la triaxialidad, mostrando que este enfoque puede ser más adecuado para la predicción del fallo que el basado en el analysis de deformaciones en el FLD.

Por otro lado, se ha realizado un análisis geométrico de los flancos convexos, evaluando los efectos de la recuperación elástica en flancos exitosos y fallidos.

Finalmente, se ha propuesto para este tipo de flancos un nuevo enfoque basado en la predicción del fallo mediante el análisis de las tensiones de compresión. En este sentido, los resultados muestran que existe un límite de compresión en términos de tensiones a partir del cual este tipo de flancos falla por arrugamiento.

Abstract

Flanging is a forming process widely used to increase the stiffness of sheet parts in industrial applications such as the production of aircraft and automobile components. Flanges are usually formed by rubber forming or using a punch and a die, as these processes are fast and economical for producing a large number of parts.

However, there is increasing interest in the manufacturing of flanges using non-conventional processes, such as single point incremental forming (SPIF), that allow cost savings due to their flexibility and low tooling.

This thesis studies the manufacturing of open stretch and shrink flanges of AA2024-T3 sheets by SPIF for a wide range of process parameters, including the flange principal radius, spindle speed and tool diameter. In this context, an experimental campaign was performed for each type of flange, classifying the principal modes of failure in the sheet and assessing its formability within the forming limit diagram (FLD).

For stretch flanging, FE modelling in combination with a theoretical framework based on Barlat's 89 anisotropic yield criterion was used to evaluate the formability in the stress triaxiality space. The fracture forming limit (FFL) obtained for proportional loading and the evolution of the flanges were compared in the average stress triaxiality versus equivalent strain space, showing that this space might be the most appropriate for making failure predictions in SPIF.

A geometry analysis of shrink flanges obtained by SPIF was carried out to evaluate their formability in terms of their tendency to develop wrinkling. The elastic recovery in successful and failed is also studied. Finally, a new approach based on the analysis of compression stresses was proposed to predict the onset of failure in this type of flange. In this regard, it was shown that there exists a stress limit at which the flanges analysed fail by wrinkling.

Contents

List of Figures

List of Tables

List of symbols

Symbols

$\bar{\eta}$	Average stress triaxiality
Δr	Additional clearance in the tool trajectory
L_s	Characteristic length
$^\circ$	Degree
d	Diameter
ϕ	Diameter of the forming tool
R_{die}	Die principal radius
$\bar{\varepsilon}$	Equivalent strain
$\bar{\sigma}$	Equivalent stress
(E)	Experimental
$F(IW)$	Failure by incipient wrinkling
$F(W)$	Failure by wrinkling
h	Flange height
$F(C)$	Fracture at the corner
$F(E)$	Fracture at the edge
n	Hardening exponent

HCl Hydrochloric acid

HFl Hydrofluoric acid

l_0 Initial length of the flange

t_0 Initial thickness

w_0 Initial width of the flange

r Lankford coefficient

r_{45} Lankford coefficient in the diagonal direction

r_0 Lankford coefficient in the rolling direction

r_{90} Lankford coefficient in the transverse direction

$log.$ Logarithm

ε_1^{ip} Major principal in-plane strain

ε_1^{arg} Major principal in-plane strain obtained using the CGA system Argus

ε_1^p Major principal plastic strain

ε_1 Major principal strain

ε_{1f} Major principal strain at fracture

mm Millimetre

mm/min Millimetres per minute

mm/s Millimetres per second

ε_2^{ip} Minor principal in-plane strain

ε_2^{arg} Minor principal in-plane strain obtained using the CGA system Argus®

ε_2^p Minor principal plastic strain

ε_2 Minor principal strain

ε_{2f} Minor principal strain at fracture

HNO_3 Nitric acid

w_p Plastic work

ν Poisson's coefficient

σ_i Principal component of the stress tensor in the 'i' direction

R_t Radius of the trajectory described by the tool

rpm Revolutions per minute

(S) Safe

c Sound speed in a specific material

S Spindle speed

Δz Step down

β Strain ratio

K Strength coefficient

σ Stress

α Stress ratio

η Stress triaxiality ratio

τ_{ij} Tangential component of the stress tensor

(T) Theoretical

t Thickness

t_f Thickness at fracture

ε_3^p Through-thickness principal plastic strain

ε_3 Through-thickness principal strain

ε_{3f} Through-thickness principal strain at fracture

ε_t^{arg} Thickness reduction obtained using the CGA system Argus®

ε_t Thickness reduction strain

Δt Time increment in explicit simulations

σ_{UTS} Ultimate tensile strength

σ_0 Uniaxial tensile yield stress

V Volt

H_2O Water

σ_Y Yield stress

E Young's modulus

Acronyms

AC Alternating current

AA2024-T3 Aluminium alloy, series 2000, heat treated and naturally aged

ASTM American Society for Testing and Materials

BCC Body centred cubic

CPU Central processing unit

CGA Circle grid analysis

CAD Computer-aided design

CNC Computer numerical control

DOFs Degrees of freedom

DIC Digital image correlation

DC Direct current

FCC Face centred cubic

FE Finite element

FEA Finite element analysis

FEM Finite element method

FLC Forming limit curve

FLD	Forming limit diagram
FFL	Fracture forming limit
HER	Hole expansion ratio
HF	Hole flanging
HG	Hourglassing
ISF	Incremental sheet forming
ISO	International Organization for Standardization
LFR	Limiting forming ratio
MF	Multiplying factor
PC	Polycarbonate
PVC	Polyvinyl chloride
SFFL	Shear fracture forming limit
SPIF	Single point incremental forming
3D	Three dimensional
2D	Two dimensional
TPIF	Two point incremental forming
UTS	Ultimate tensile strength
UNE	Una Norma Española
US	Universidad de Sevilla
WLC	Wrinkling limit curve

Chapter 1

Introduction

This chapter contains a brief introduction to the document. The first section presents a general overview of this work. The second section outlines the main objectives of this work. The third section contains a brief description of each chapter.

1.1 General overview and motivation

Sheet flanging is a forming process widely used in the manufacturing industry in which a workpiece, usually a pre-cut metal sheet blank, is subjected to the application of loads to obtain a flanged part. Although it is possible to apply this process to other materials such as polymers or composites, most common applications utilize metal sheets to produce components for the aerospace and automotive industries. Hole flanges and open flanges are, for example, common in aircraft components for different purposes, such as providing a surface suitable for riveted joints or contributing to increasing the stiffness of the parts.

To reduce costs, the processes selected to carry out the flanging operations are usually hydroforming or conventional press working, which entail an initial high investment to produce dedicated tools but maintain low cost per unit in large batch production. However, when a small number of parts need to be manufactured, as is the case for small batch products or prototypes, the cost per unit using conventional processes increases notably, making the exploration of alternative forming processes reasonable.

Single point incremental forming (SPIF) is a manufacturing process that con-

sists of the incremental deformation of a sheet blank using a forming tool with only one contact point transferring the force. During this process, the blank is clamped peripherally, and the tool follows programmed trajectories usually driven by a CNC machine. This technology reduces the use of dedicated dies commonly employed in conventional flanging and increases the flexibility in the part geometry, which only involves changing the tool path. However, its incremental nature makes the process very time consuming compared to conventional processes. These characteristics, among others, make SPIF suitable for prototyping and small batch production but less viable for producing a large number of parts.

The present work analyses the manufacturing of open flanges via SPIF. The formability limits of this process in stretch and shrink flanging with different initial geometries and process parameters are experimentally and numerically studied, as are the deformation mechanisms involved during the flanging process.

1.2 Objectives

The main objective of the present work is to investigate the flanging process by SPIF with the purpose of increasing the current knowledge of this technology. Concretely, this study focuses on the analysis of stretch and shrink flanges, which are geometries common in industrial applications. In a more practical sense, the aim of this investigation is to help future designers make profitable decisions related to the capabilities of the SPIF process in the manufacturing of flanged parts of AA2024-T3. This general objective was realized through the following individual objectives:

1. Characterization of the formability and tensile properties of AA2024-T3 sheets using Nakazima tests and tensile tests.

2. Assessment of the SPIF process windows for shrink and stretch flanging by performing an experimental campaign involving different parameters and providing a critical analysis based on the evaluation of principal strains.

3. Design and validation of finite element models for stretch and shrink flanging by SPIF that reproduce the experiments performed in the experimental campaign.

4. Provision of predictions of failure for stretch and shrink flanging based on the analysis of the stress triaxiality and compression stresses obtained from the FE models.

1.3 Thesis framework

This thesis is divided into six chapters, including the present introduction as chapter 1. First, chapter 2 reviews the state of the art of SPIF and describes the sheet flanging processes hole flanging, stretch flanging and shrink flanging. Then, chapter 3 details the experimental procedures and methodologies used in this study. In addition, chapter 4 describes the stretch and shrink flanging numerical models and the methodology followed to obtain the principal strains in the plane of the sheet. The analytical framework regarding the plasticity criterion used in the finite element models is revealed in chapter 5, describing how the FFL curves in the stress triaxiality versus equivalent strain space are obtained. In chapter 6, the results obtained from the stretch and shrink flanging experimental tests and the results corresponding to the numerical simulations are analysed critically. Finally, chapter 7 summarizes the main contributions of this doctoral thesis and outlines a future work proposal.

Chapter 2

State of the art

This chapter provides a review of the literature related to incremental sheet forming, especially focusing on single point incremental forming and its applications to flanging. The first section in this chapter presents an introduction to sheet metal forming, describing conventional sheet metal techniques and incremental sheet metal forming processes. The second section describes the SPIF process, focusing on the formability background and the main parameters related to this technique. In the last section, an approach to the practical application of SPIF is presented, focusing on industrial applications related to hole flanging and open flanging processes.

2.1 Sheet metal forming

Sheet metal forming comprises those operations in which a sheet blank is shaped permanently by applying a force instead of removing material. In most sheet metal forming processes, the part is produced by direct contact of tools and dies, although in some modern variants, this is not strictly necessary. The material is usually under cold conditions, but sometimes, the process can be performed at increased temperatures, taking advantage of the lower resistance to deformation. In conventional sheet metal forming processes, products are usually almost finished parts generated in a short period of time after a single press stroke, producing little scrap. Consequently, these processes offer the potential for cost savings and reduced energy and material consumption and are appropriate for intensive manufacturing of functional parts with a wide range of dimensions from the microlevel

to large structures (Altan and Tekkaya, 2012).

Parts produced by sheet metal forming possess high strength and relatively low weight owing to the high moment of inertia given by their shape. This, combined with good geometric and surface tolerances, leads to sheet metal forming products being commonly selected to supply light structural components in aircraft and automotive industries where the weight-strength relation is important to reduce fuel consumption. In these industries, flanged parts are usually present in many structural components.

The main core of this work focuses on flanging operations using non-conventional incremental forming techniques. The next sections describe the main conventional sheet metal forming operations related to the manufacturing of flanges and present a historical overview of the incremental forming method and processes existing in the literature.

2.1.1 Non-incremental processes

This section describes the main forming processes related to the manufacturing of flanges. First, a description of the bending process is presented. Second, the principal characteristics of the conventional flanging process are described. Finally, the section concludes with other techniques also used in the manufacturing of flanged parts, such as fluid forming and rubber forming.

2.1.1.1 Bending

Bending is defined as the process of forming a sheet to obtain an angled part. It constitutes a process by itself, but sometimes, it is considered a feature present in any manner in all sheet forming operations. Bending is one of the most common sheet forming operations, which is easy to prove by looking at automobile parts, structural or aesthetic profiles, appliance casings and many other products. Having corrugations or a bent perimeter contributes to increasing the stiffness of the part without adding weight. These characteristics are present in almost every formed part.

Figure 2.1 shows a bent sheet and its principal features. Sheets subjected to pure bending present tensile stress at the outer face and compression stress at the inner face, with the neutral axis being the theoretical line that is subjected to neither tension nor compression (Kalpakjian and Schmid, 2009).

Typical failure in bending occurs when small cracks appear at the outer face,

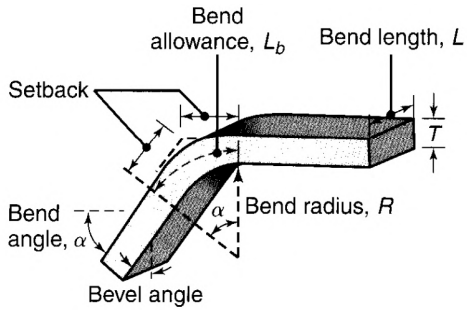

Figure 2.1. Bending terminology described in Kalpakjian and Schmid (2009).

which may be only a superficial defect or the beginning of unstable fracture. Another relevant aspect of bending operations is the elastic recovery after bending, which is commonly called springback. This phenomenon occurs as a consequence of the elastic behaviour of the material and has to be taken into account to achieve a specific final shape. Springback appears more intensively in thick sheets than in thinner sheets and as the bending radius increases. Springback is usually mitigated by bending the part in excess to achieve the desired geometry. This is known as overbending.

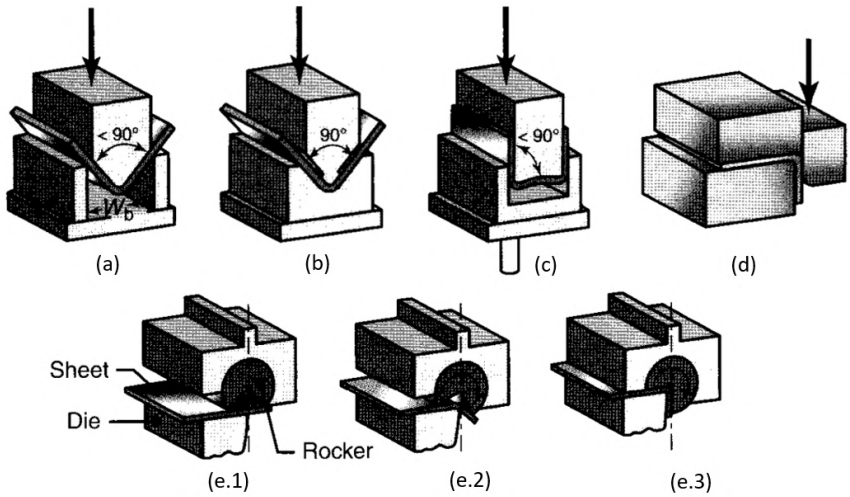

Figure 2.2. Basic sheet bending processes: (a) air bending, (b) V-bending, (c) U-bending, (d) wiping bending and (e) rotary bending (Kalpakjian and Schmid, 2009).

Figure 2.2 shows basic bending operations such as air bending, V-bending, U-

bending, wiping bending and rotary bending. The use of dies in U- and V-bending and blank holders in wiping bending has the purpose of reducing springback, which is lower in these operations compared to air bending. Rotary bending also contributes to reducing springback and is able to produce bending angles higher than 90 degrees.

2.1.1.2 Flanging

Flanging is the forming operation in which the edge of a sheet part is usually folded at 90 degrees. The main difference from a bending operation is the additional curvature of the die on which the sheet is folded. Sometimes, bending is also indistinctly called straight flanging when the die curvature does not exist. Figure 2.3 shows different flanging types depending on the final shape of the flange. In the case of producing a concave or a convex radius at the part edge, the process is called stretch flanging or shrink flanging, respectively. Additionally, when both types are concatenated, reverse flanging is performed. A jogged flange is the junction of two straight flanges at different levels, as shown in figure 2.3d. Finally, a hole flange consists of reproducing the stretch flanging process on the edges of a previous hole.

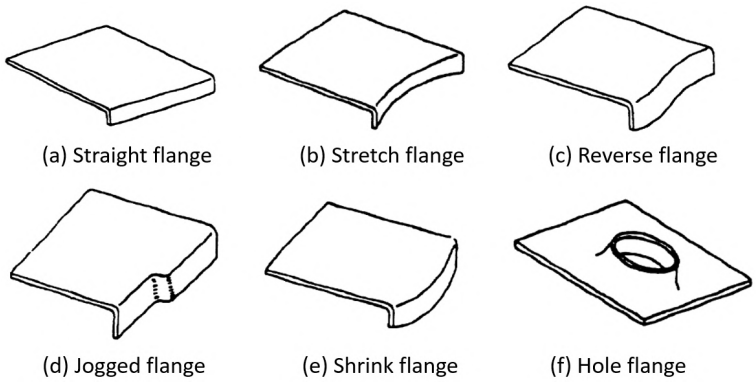

Figure 2.3. Sheet flanging types (Smith, 2009).

Most common flanging applications have the purpose of adding stiffness, increasing the strength or simply giving a smooth edge to a component. The process itself can be used as an independent operation or as a previous stage in a more complex process, as in the case of hemming, where flanging is usually the first stage.

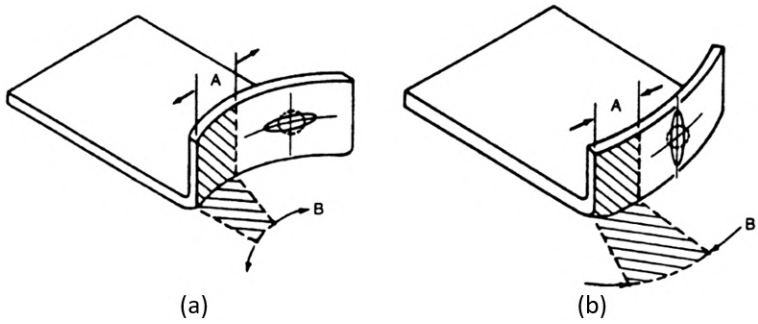

Figure 2.4. Scheme of material behaviour in (a) shrink flanging and (b) stretch flanging AISI (1988).

In stretch flanging, the material to be formed experiences tension in the circumferential direction due to the transition of the material from the initial arc to a larger final arc, as shown in figure 2.4a. In these cases, the stress is higher at the flange edge, being greater in flanges with a higher ratio between the final and initial radii, while the material does not experience any circumferential straining. Due to these stretching conditions, the characteristic failure is tearing, which appears at the edge of the flange wall. Actions such as reducing the flange height or increasing the sheet thickness can be adopted to reduce tearing, although sometimes, the only available option is splitting the flange into several parts.

In shrink flanging, the material is under compression and experiences a transition to a smaller arc, as shown in 2.4b. In this case, the effect of bending is the opposite of that in stretch flanging. The stresses are compressive at the edge and null near the die bending zone. Failure in shrink flanging occurs when excessive compression occurs, producing wrinkling. This effect can be mainly avoided by reducing the flange height. It is also related to the flange width, so it can be reduced by splitting the flange. In the case of flanging produced by press working, the buckling effect can also be diminished by reducing the clearance between the forming tool and the die or ironing out the wrinkles.

2.1.1.3 Fluid forming

Fluid forming is a process based on the use of pressurized liquid media to execute forming operations. In this section, only fluid forming using rubber pads will be described due to the use of this process as an alternative to conventional flanging by press working (Asnafi, 1999).

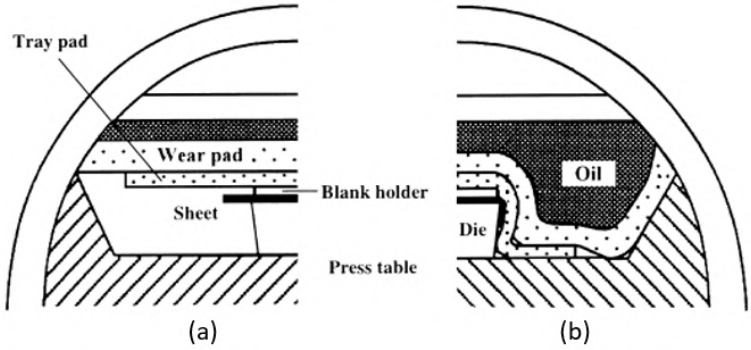

Figure 2.5. Scheme of a fluid forming process: (a) prior to the forming operation and (a) after forming (Asnafi, 1999).

Figure 2.5 depicts a fluid forming scheme corresponding to a flanging operation prior to and after the forming process. On the left part of the drawing, the elements of the die, sheet, pads and forming oil are arranged in ascending order. When the oil pressure is increased, the flexible pads progressively fill the lower cavity, and the sheet clamped between the die and blank holder is pressed against the die, acquiring its shape. The main advantage of this process is the absence of an upper die, which allows a sensible cost reduction in low batch production and the capability to produce complex shapes. However, additional effort is needed to design the process variables to predict the behaviour of the flexible pad and avoid unwanted results in the final part.

2.1.1.4 Rubber forming

The principle of rubber forming is similar to that of fluid forming except that in this case, hydrostatic pressure is applied using a deforming elastomer. The sheet is forced against a female die or wrapped over a punch (male die), acquiring the shape of the non-rubber part, as shown in figure 2.6. The rubber forming process has a low tooling-manufacturing cost because only one die is metallic. As in fluid forming, this feature increases the flexibility and reduces costs in the production of a low number of units, such as in the aircraft industry, where this technique is widely employed to produce flanges (Chen *et al.*, 2015a). Nevertheless, the flexibility of this process is faced with the complexity of involving a non-linear approach due to the rubber medium and the complexity of avoiding instabilities during sheet deformation. Furthermore, as in any flanging operation, the height of

the flange is a key factor determining whether the process will be successful, and the bending die radius has to be large to avoid fractures in the bending region.

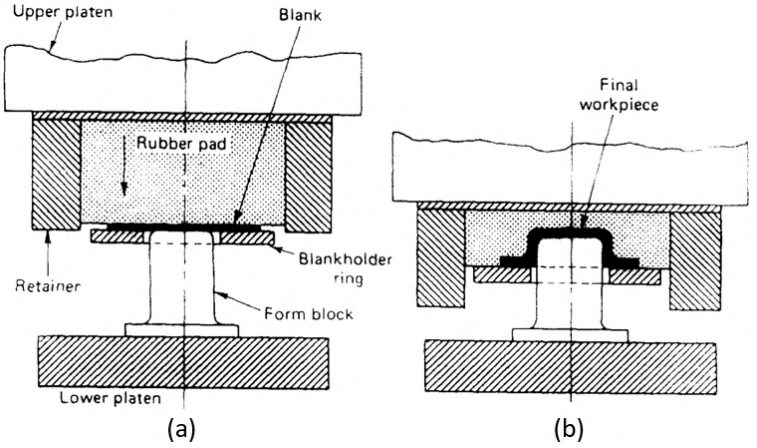

Figure 2.6. Scheme of a rubber forming process: (a) prior to the forming operation and (b) after forming (Venkatesh and Goh, 1986).

2.1.2 Incremental sheet forming (ISF)

Incremental sheet forming techniques include those methods that allow progressive deformation of a workpiece, producing localized permanent strains, and satisfy the requirement of having a small contact area between the tool and the surface to be formed. Over the years, ISF has been in the background of forming processes mostly due to the use of more common processes such as stamping or deep drawing. However, in recent decades, incremental processes have gained attention due to an increasing interest in more flexible technologies and tool cost savings. This has also been intensified by the evolution of CAD/CAM technologies, which have been decisive in the development of incremental techniques. To better understand ISF processes, the most important techniques will be covered.

2.1.2.1 Spinning

Many research papers have reviewed the recent history of modern incremental sheet forming processes, e.g., Hagan and Jeswiet (2003) or Jeswiet *et al.* (2005), and they all agree that before the second half of the 20th century, these processes were more an art than a science. Spinning is considered to be the precursor of

what today is known as incremental sheet forming, and until the 1950s, skilful human operators were required to carry out the process manually.

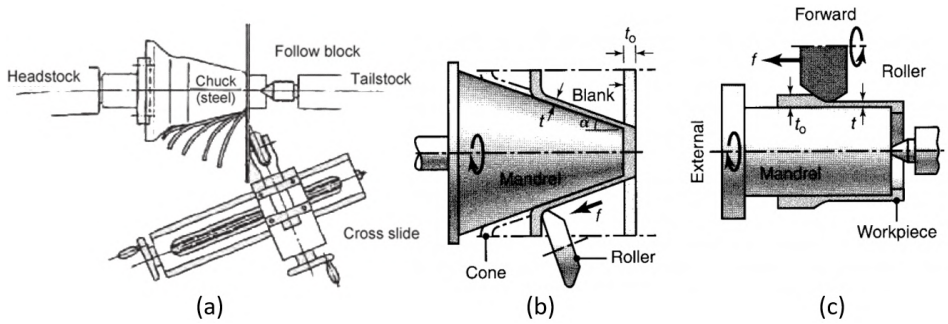

Figure 2.7. Spinning variants: (a) conventional spinning by Wong *et al.* (2003), (b) shear forming and (c) flow forming (Kalpakjian and Schmid, 2009).

Spinning is commonly described as the process of forming a rotary sheet metal blank with the help of a tool that presses the sheet usually against a mandrel. Although the general concept is clear, the term spinning is commonly used to refer to a group of incremental processes: conventional spinning, shear forming and flow forming. In spinning, the supplied material is a flat sheet, and the thickness remains constant during the process, as shown in figure 2.7a. In a shear forming process, the raw material can be a preformed sheet that is ironed against the mandrel, reducing the initial thickness, as depicted in figure 2.7b. Finally, in flow forming, also called cylindrical flow forming, the process starts from a cup or bush of metal that is ironed against the mandrel, as in shear forming, as shown in figure 2.7c.

2.1.2.2 Two point incremental forming (TPIF)

The typical spinning parts used to be axisymmetric, and a mandrel was needed to wrap the sheet blank around. Works by Kitazawa *et al.* (1996, 1997 and 1997) showed that controlling the deformation in symmetric spinning without a mandrel was possible and contributed to the first step toward asymmetric forming. These advances, together with computer-aided machines and the development of CAD software, definitely made asymmetric incremental sheet forming (AISF) possible. The AISF technique was first patented by Leszak (1967) and is characterized by the absence of dedicated dies and tools always in contact with the part. The first method of AISF was developed by Powell and Andrew (1992) and was then called

the backward bulge method by Matsubara (1994). Figure 2.8 shows the scheme of the backward bulge method first presented by Matsubara, in which the sheet is only pressed by the forming tool on one side at a time, with the inner part of the sheet being free except for the region in contact with a fixed support post.

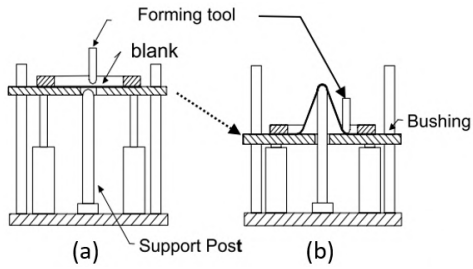

Figure 2.8. Backward bulge method: (a) prior to the forming process and (b) during the process (Matsubara, 1994).

In similar studies, Jeswiet *et al.* (2005) applied CNC technology to create asymmetric geometries. Two point incremental forming (TPIF) was a consequence of the development of asymmetric forming processes, CNC-driven machines and computer-aided technologies. This process has the same elements as the backward bulge method but adds a CNC-driven tool.

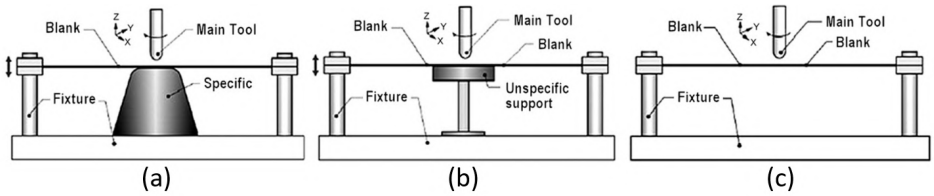

Figure 2.9. Asymmetric incremental forming methods: (a) TPIF with a specific die, (b) TPIF with a partial die and (c) SPIF (Shankar *et al.*, 2005).

In TPIF, the metal blank is held between the blank holder and a fixed support, while the forming tool shapes the sheet metal. The vertical die can be a specific support, and therefore, the tool has to keep pressing the blank against the die. When the die is only partial, the sheet does not always have to be in contact with the tool on the two sides. See figure 2.9a and b.

2.1.2.3 Single point incremental forming (SPIF)

Single point incremental forming was developed as a variant of TPIF in which the support opposite to the face in contact with the tool was removed. The idea of forming without a die was already included in the patent of Leszak (1967), but the absence of the technology needed to accomplish this process delayed the first studies about this method until the work of Jeswiet and Hagan (2002), who first applied this technique.

The SPIF process is, in many aspects, very similar to the ISF processes already described. A blank is used to clamp a sheet at its perimeter, while a single tool describes programmed trajectories and deforms the material, obtaining a final tridimensional part. Laboratory examples of this process can be seen in figure 2.10, which contains different pictures of a common experimental set-up for SPIF configurations.

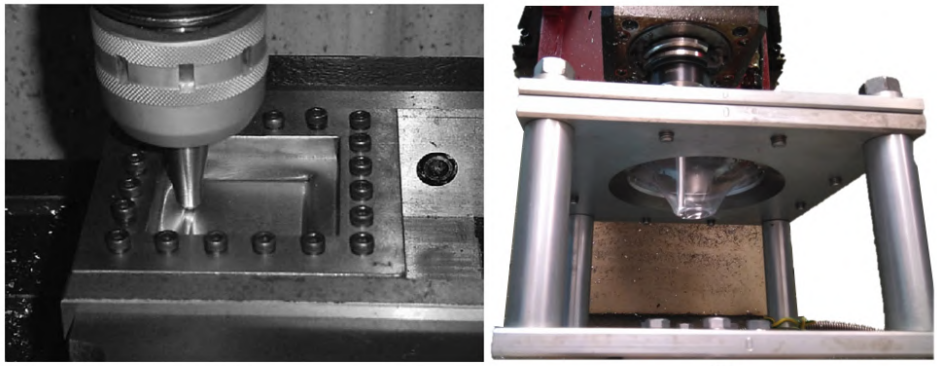

Figure 2.10. Two examples of laboratory experiments performed by SPIF: (a) manufacturing of an aluminium pyramid by SPIF (Jong-Jin and Yung-Ho, 2003) and (b) polycarbonate truncated cone from a lower view.

The simple idea of removing the die is attractive because it can be accomplished in any factory with a CNC milling machine, making sheet forming accessible to different levels of manufacturing. Using this method, it is possible to achieve complex surfaces using standard equipment while providing a solution to adapt the production to very different shapes. An example of the achievable geometries is given in figure 2.11, which demonstrates the viability of the process in producing different shapes. Furthermore, this method makes it feasible to produce custom manufactured parts, such as the car hood shown in figure 2.12 or small batch

productions.

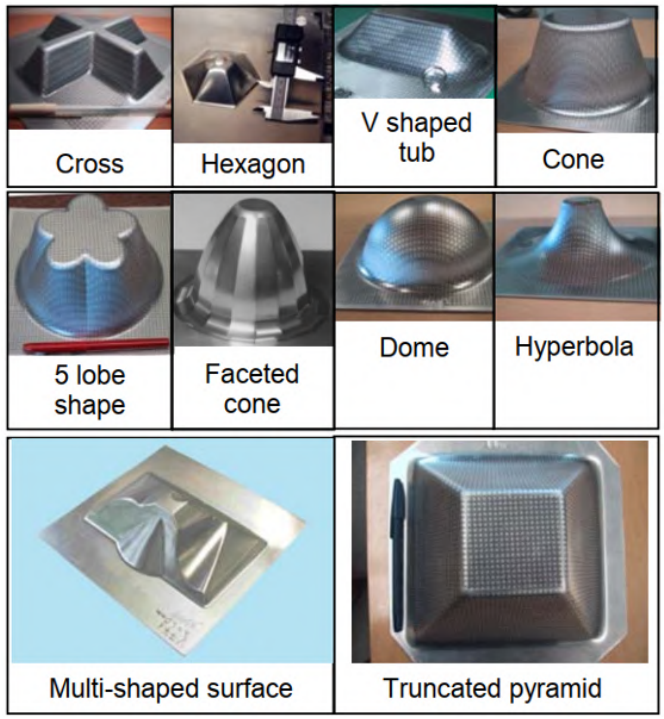

Figure 2.11. Different shapes used to demonstrate the viability of the process Jeswiet *et al.* (2005).

Figure 2.12. Honda S800 hood made by Amino in a small series (Maki, 2006).

The next sections more deeply explore the different attributes of single point incremental forming, describing the different process parameters involved in the process, reviewing the principal approaches regarding the mechanism that confers one of its main advantages, the increased formability, and analysing the geometric accuracy.

2.2 Fundamentals of single point incremental forming

The simplest SPIF configuration consists of a sheet clamped at its perimeter, which is incrementally deformed using a tool that describes programmed trajectories with the purpose of achieving a desired geometry. Based on this definition, many factors that are involved in the process should be considered since they determine the result of this forming process, such as the process parameters themselves, the characteristics attributable to the deformation mechanics and formability in SPIF and the geometric accuracy of the resulting parts. These factors will be described in this section with the purpose of serving as a theoretical basis for the following chapters.

2.2.1 Process parameters

The properties of the resulting part are determined by the selection of a wide variety of process parameters related to the incremental process. A simple classification of these parameters divides them into qualitative parameters, e.g., the selected sheet material, the shape of the tool or the toolpath strategy, and quantitative parameters, such as the feed rate or the step down increment of the tool. In this regard, this section presents the different options and values of the most relevant parameters in the SPIF literature.

2.2.1.1 Material and thickness

The ductility and high formability at room temperature have led to metals being widely used in incremental forming. Many studies focus on copper, magnesium, steel and titanium, but aluminium alloys are by large the most studied material in SPIF (McAnulty *et al.*, 2016), although polymers such as PVC, PC and PE (Le *et al.*, 2008),(Martins *et al.*, 2009) and other composite materials such as sandwich panels (Jackson *et al.*, 2008) have also been studied.

The thickness of the sheet material is also an important parameter because it affects the formability and the forces required in the forming process. Sheet thicknesses in the range of 0.3-2 mm are common for metals, while higher values up to 3 mm have been studied for polymers (Silva *et al.*, 2010). Microincremental forming has also been performed with sheet thicknesses below 0.1 mm.

2.2.1.2 Tool parameters

The forming tools are usually made of hard steel, and their shape is typically selected among the three types shown in figure 2.13. The simplest tool is a hemispherical tool (figure 2.13a) made in a single part (Hagan and Jeswiet, 2003). Another typical tool shape variant (figure 2.13b) consists of a rolling ball embedded in a socket that moves freely during the forming process with the purpose of reducing friction between the tool and sheet (Shim and Park, 2001); (Lu *et al.*, 2014). Additionally, other tool shapes have been used as the SPIF process has been developed, obtaining different advantages, such as the flat-ended tool (figure 2.13c) or the tools proposed by Allwood and Shouler (2007) in the process called "paddle forming".

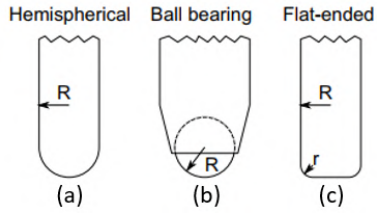

Figure 2.13. Main types of tools used in SPIF: (a) hemispherical tool, (b) rolling ball tool, and (c) flat-ended tool (McAnulty *et al.*, 2016).

In the case of the rolling ball tool, the moving part is the ball itself, and no spindle speed is applied, with the relative displacement between the ball and the tool subject to the tribological conditions. In contrast, for the rest of the tool types, a spindle speed is usually applied in the range of 0 to 25000 rpm, although it can also be set as "free rotation". The rotation direction can be set clockwise or counter-clockwise. In general, little difference has been found at high spindle speeds (Obikawa *et al.*, 2009), with effects only on the surface finish and forces (Durante *et al.*, 2011). With respect to the geometry, not only is the shape relevant, but also, the dimensions of the tool influence the result of the SPIF

process. Usually, tool radii are in the range of 4-20 mm. Lower tool radii reduce the contact area with the sheet, concentrating the zone of deformation, while large tool radii have the inverse effect.

2.2.1.3 Lubrication

The use of a lubricant reduces the forces involved in the process as well as the temperature of the surfaces that are in contact during the SPIF process. As mentioned, it is usual to employ a different lubricant depending on the sheet material to be formed. Therefore, the use of grease (Duflou *et al.* (2007b), Jackson and Allwood (2009), Kopac and Kampus (2005)) or oil (Bambach *et al.* (2009), Li *et al.* (2015), Park and Kim (2003), Takano *et al.* (2008), Verbert *et al.* (2008)) is the most common option for metals, while some authors use a water soap emulsion in incremental forming of polymers (Franzen *et al.* (2009), Marques *et al.* (2012), Silva *et al.* (2010)). Furthermore, solid powders such as graphite and MoS_2 powder have also been employed in studies carried out by Fan *et al.* (2009), Husmann and Magnus (2016) and Zhang *et al.* (2010).

2.2.1.4 Trajectories

The path strategy, step down and feed rate are process parameters specified in the CNC program that define the translation of the tool.

Regarding the toolpath, there are three basic strategies (Jeswiet *et al.*, 2005). The simplest and most common strategy, shown in figure 2.14a, is to apply a toolpath defined by fixed Δz increments between consecutive discrete contours. This technique can be modified by defining different Δz as a function of the slope of the forming geometry. It should be noted that a higher step down Δz reduces the surface quality. The position of the z movement can be designed to occur at different locations each time with the purpose of avoiding undesired marks in the final part, which can be observed in figure 2.15. At the same time, the direction of the path can be modified to alternate in subsequent contours to reduce a possible twisting effect in the part.

Another option is to use helical trajectories (see figure 2.14b) where the z increment is progressively applied. This strategy avoids the force peak derived from punctual Δz decrements and step down marks (Hirt *et al.*, 2004) and (Filice *et al.*, 2002). More sophisticated strategies are based on intermediate forms that apply the process in two different stages (figure 2.14c), with the first stage similar to a roughing step with higher Δz decrements and a subsequent finishing pass

performed using the contour strategy with low step down or a helical toolpath, also reducing the excessive strains in areas with high slope (Young and Jeswiet, 2004).

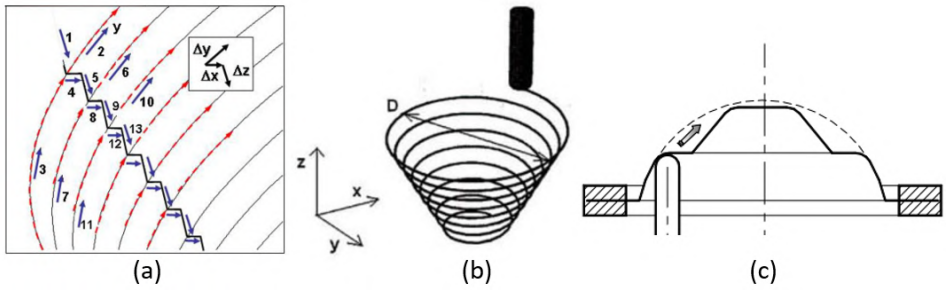

Figure 2.14. Different toolpath strategies in SPIF: (a) constant Δz (Jeswiet, 2004), (b) spiral toolpath strategy (Filice *et al.*, 2002) and (c) two-stage forming of a hemisphere Kitazawa and Nakane (1997).

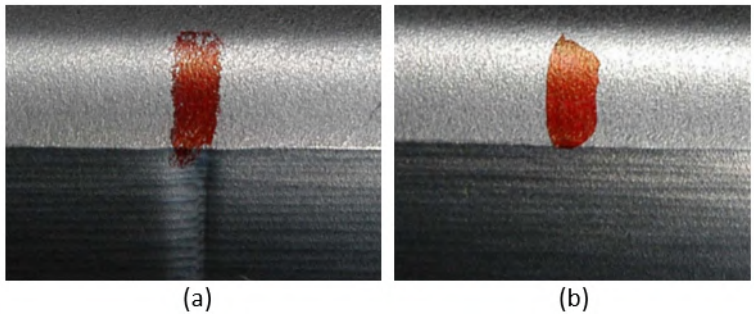

Figure 2.15. Inner surface of a cone formed by SPIF: (a) using constant Δz and (b) with a spiral toolpath strategy Skjoedt *et al.* (2007).

With respect to the size of the step down Δz, values in the range of 0.2 to 0.6 mm are the most employed in the literature. Outside this range, some authors have studied higher values, up to 2 mm, and values below 2 μm in microincremental forming (McAnulty *et al.*, 2016). The strategy followed may use constant step down, where a single value of Δz is set for the entire process (Attanasio *et al.* (2006), Attanasio *et al.* (2008)); constant scallop height, where the parameter that determines the z movement is an established maximum scallop, as defined in figure 2.16b-c (Callegari *et al.*, 2006); or a constant angular increment, as depicted in

figure 2.16d (Fiorentino *et al.*, 2009). These three toolpath strategies and a detail of the scallop height are shown in figure 2.16.

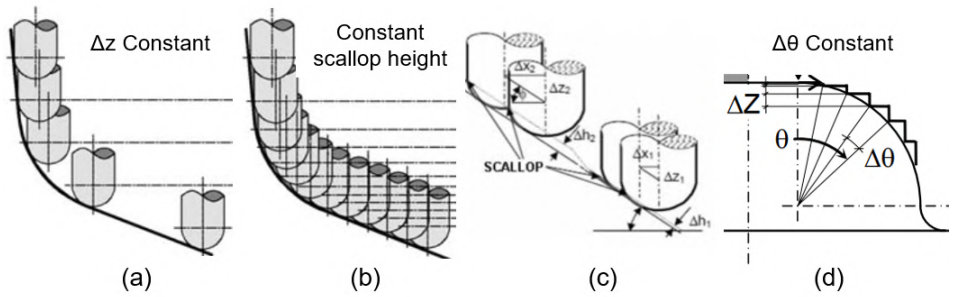

Figure 2.16. Step down strategies in incremental forming: (a) constant Δz, (b) and (c) constant scallop height and (d) constant θ (Callegari *et al.*, 2006), (Fiorentino *et al.*, 2009).

The last parameter related to the CNC trajectories is the feed rate, which is the name given to the linear speed of the tool usually measured in mm/min. The effect of this parameter seems to be quite small based on the number of publications on this topic. For example, the small effects of the feed rate on formability were shown by Pereira Bastos *et al.* (2016) at different rates from 1500 to 12000 mm/min for four different materials. Consequently, the feed rate is set as high as can be afforded by the different elements involved in the SPIF process to decrease the production time. However, it should be taken into account that for very high speeds, the lubrication and stiffness of the different elements may be redesigned.

2.2.2 Formability in SPIF

Formability is the term used to define the degree of deformation that a material can be subjected to during a forming process. Over the years, the extent of this deformation has been graphically evaluated in conventional sheet forming processes via the evaluation of the major and minor strains (ε_1 and ε_2) in the forming limit diagram (FLD). The FLD was initially developed by Keeler and Backofen (1963) in the biaxial region and then extended to the tension-compression region by Goodwin (1968). Figure 2.17a schematically shows the fracture forming limit (FFL) originally proposed by Atkins (1996), which represents the initiation of fracture in a sheet. The forming limit curve (FLC) defines strains at which

necking occurs in a sheet forming process.

The straining of sheet metal induces an increase in the number of dislocations and their interaction, which leads to fracture (Pohland *et al.*, 1985). In the FLD, the FFL represents the fracture locus in mode I for strain ratios $\beta = \varepsilon_2/\varepsilon_1$ between -0.5 and 1. This curve has a theoretical slope of -1 and, therefore, defines a region of constant through-thickness strains in the FLD. In addition to the theoretical definition of the FFL, the nature of the process influences the maximum strain achievable. For example, in forming processes that principally involve compression, e.g., rolling, the damage mechanism is slowed down, obtaining large strain levels. This phenomenon is a consequence of void squeezing caused by compressive hydrostatic stress Emmens (2011). In contrast, this compression effect is not present in other processes, such as conventional stamping or deep drawing. In these processes, necking appears at strains below the FFL (at the FLC), triggering fracture prematurely.

The FLC usually has the v-shape shown in figure 2.17a. It represents the limit at which necking occurs for ductile materials and is usually below the FFL. The region between the FLC and the FFL is unstable, and any strain point in the middle is achievable without triggering fracture. Nevertheless, tensile fracture may precede necking under specific forming conditions, and in that case, the FFL instead of the FLC applies, as reported by Embury and Duncan (1981). The studies performed by Vallellano *et al.* (2008) and by López-Fernández *et al.* (2019) also showed that for AA2024-T3 sheets, the FFL can be very close to the FLC, even acquiring a v-shape as shown in figure 2.17b.

The most common method to obtain the FLC consists of performing drawing tests using a hemispherical punch and evaluating the strains at necking (Nakazima tests). Although the use of the FLC is widely accepted in conventional sheet forming, it is effective only if four hypotheses are fulfilled: (1) proportional loading, (2) absence of bending, (3) negligible through-thickness shear and (4) plane stress (Emmens and Van den Boogaard, 2009). These conditions are not met in ISF, where strains above the FLC are stably obtained. Numerous studies on ISF and specifically on SPIF demonstrate that there exists an increase in formability and necking stabilization compared to conventional processes. For example, Iseki *et al.* (1993) used aluminium, and more recently, Centeno *et al.* (2017) used AISI304. The reason is well discussed in many research papers that attempt to explain this phenomenon, focusing on the understanding of the deformation mechanism in ISF processes. The next sections review the main theories about the increased

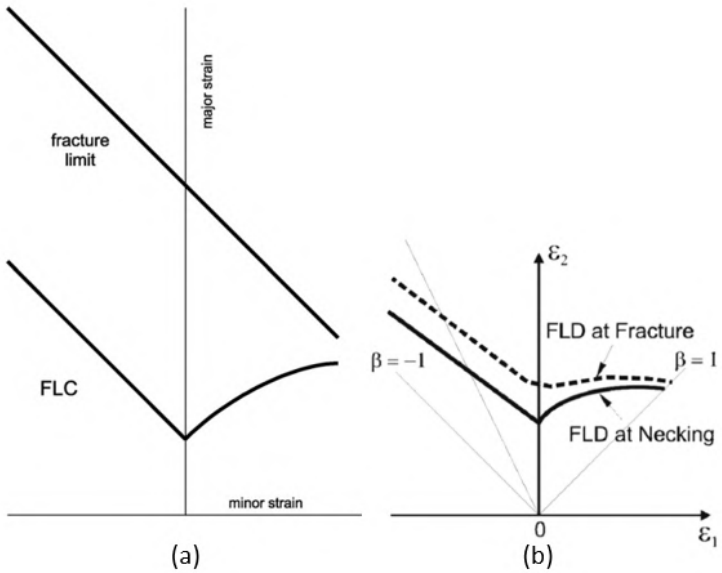

Figure 2.17. Representation of the FLD containing the FLC and FFL: (a) for a ductile material (Emmens and Van den Boogaard, 2009) and (b) for a low ductility material (Vallellano *et al.*, 2008).

formability in SPIF and how the different parameters affect this forming process.

2.2.2.1 Shear

The contribution of shear stress to stabilizing necking can be directly deduced from the von Mises yield criterion. The effect of additional shear stress in an in-plane stress state modifies the yield locus as shown in figure 2.18a. If a sheet metal is subjected to shear stress, then the material flows at curve C before reaching the yield stress represented by curve A. This causes localization of strains. However, strain localization reduces the shear stress and enlarges the yield locus from curve C to a point between curve C and curve A. As a consequence, more straining can be added before unstable strain localization (necking) occurs. Larger straining will cause shear stress to appear, and the cycle starts again. This phenomenon of strain localization followed by stabilization repeats until the in-plane stresses are sufficient to cause fracture in addition to the effect of shear (Emmens and Van den Boogaard, 2009). The effect of shear stress on both the yield stress and necking limit is presented in 2.18b.

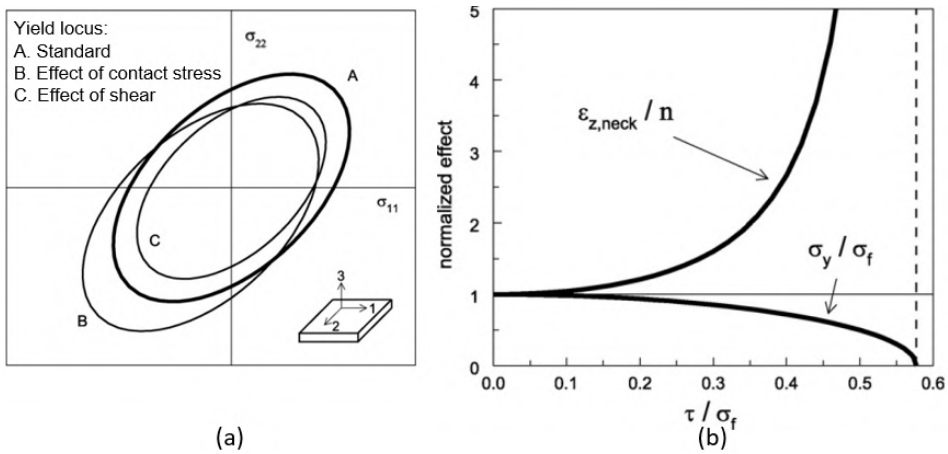

Figure 2.18. (a) Schematic representation of shear in the von Mises yield locus and (b) effects of shear on both the yield stress and necking limit (Emmens and Van den Boogaard, 2009).

Many authors have studied the necking stabilization caused by shear stress in ISF. Some of them pointed to out-of-plane shear, schematically represented in figure 2.19a), as being responsible for necking stabilization (Sawada, 1999). However, as shown by (Jackson and Allwood, 2009), this was more based on intuition than experimentation.

Allwood and Shouler (2007) used finite element analysis to simulate a process called "paddle forming". They showed the existence of through-thickness shear in the tool direction and concluded that it increases the effective stress and enhances the formability. Similar results were obtained by Jackson *et al.* (2008) and Jackson and Allwood (2009) in the SPIF of sandwich panels and copper sheets, respectively. The latter publication established that in terms of deformation mechanisms, SPIF and TPIF must be considered separately. Malhotra *et al.* (2012) also supported these through-thickness shear theories, adding that local bending, especially the strains at the outer face of the sheet, should be taken into account and proposed his "noodle theory". This theory affirms that different passes of the tool create successive regions of local stable deformation before fracture occurs.

Additionally, some of the authors supporting the through-thickness shear theory also found relations between shear and the stress triaxiality. Lu *et al.* (2014) claimed that the through-thickness shear caused by friction has contrary effects. It acts as a stabilizer of necking but also increases the stress triaxiality.

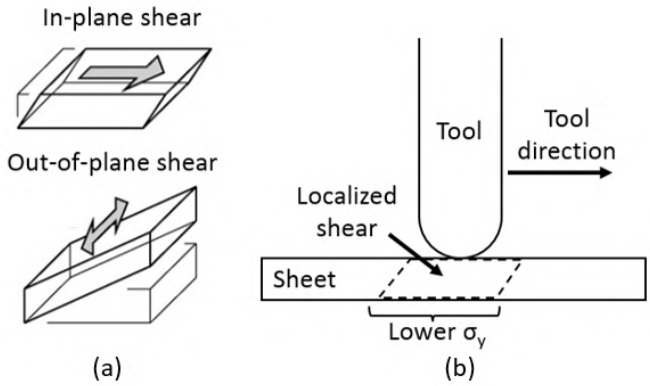

Figure 2.19. (a) Representation of in-plane and out-of-plane shear and (b) scheme of localized shear induced by the tool in SPIF.

2.2.2.2 Bending

The effect of bending is also claimed by many authors to be responsible for the increased formability in ISF. In SPIF, the material is subjected to bending due to the tool radius as well as stretching, and this mechanism is supposed to act as a necking stabilizer.

Figure 2.20a shows a schematic representation of the through-thickness strain present in bending processes with different degrees of stretching. Additionally, the relation between stress (σ) and strain (e) in the centre fibre is presented in figure 2.20b. In a pure bending process, whose strain distribution is represented in figure 2.20a number 1, the outer fibre of the sheet experiences tensile strains of $e_b \simeq t/2R$, where e_b is the strain at the outer fibre in a pure bending process of constant radius. The centre fibre is subjected to zero strain ($e = 0$), and the compression strain at the inner fibre is t/2R. This stress-strain state is represented by number 1 in figure 2.20b, where σ and e are zero. If stretching is added, as in figure 2.20a number 2, e and σ increase, inducing localized deformations. This creates the situation of stable elongation represented by the segment between 1 and 3 in figure 2.20b. However, for $e > e_b^*$, the process becomes unstable, and e increases indefinitely, as no more stress is needed to increase the strain at the centre fibre. Based on this hypothesis, the length of the auto-stabilizing regime depends on both the sheet thickness and the die radius, and it is limited by the expression $e_b = t/2R$. Consequently, the process can be repeated only if, at every pass of the tool, the strain increments are in segment 1-3.

The effect of bending under tension was examined by Emmens and Van den Boogaard (2008), who concluded that in ISF, only the material under bending, i.e., the region of the sheet in contact with the forming tool, is subjected to deformation. They showed that large stable deformations can be achieved if low amounts of bending are added to the stretching process, with little effect on the material hardening due to the cyclic character of the process. A detailed analysis of the effect of bending on the appearance of necking and fracture in the stretch-bending process was performed by Morales-Palma et al. (2009, 2013). Additional research on bending and strain hardening was performed by Fang *et al.* (2014). This study analysed the strains in the vicinity of the contact area and concluded that the deformation affects the regions surrounding this zone. Based on stress triaxiality evaluations, they also determined that fracture occurs at the outer face of the sheet in the zone where the contact region ends.

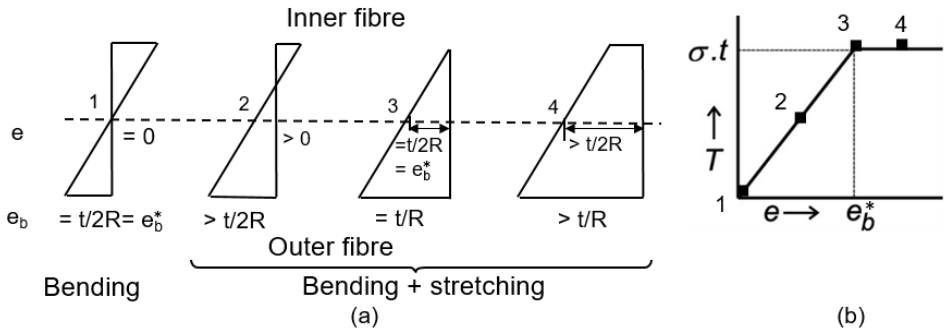

Figure 2.20. (a) Schematic representation of the strain distribution along the sheet thickness under different stretch-bending conditions: (1) pure bending and (2)-(4) gradual increments of stretching. (b) Relation between tension and elongation of the centre fibre under different stretch-bending conditions (adapted from Emmens and Van den Boogaard (2009)).

In addition to the bending-under-tension theory, some researchers claim that localized bending around the forming tool produces contact compressive stresses, reduces the yield stress and increases the formability (e.g., Emmens and Van den Boogaard (2009), Silva *et al.* (2008) and Martins *et al.* (2008)). This is deduced from the von Mises yield criterion because the contact stress reduces the yield stress in the biaxial region, as depicted by the B curve presented in figure 2.18a. Regarding this theory, (Silva *et al.*, 2008) and (Silva *et al.*, 2009) presented an analytical model for SPIF based on membrane analysis, contrasted using exper-

imental and numerical results that pointed to stretching rather than shearing as the dominant deformation mode.

Along this line, numerous research papers have attributed the increased formability in SPIF to the postponement or suppression of necking. For example, Silva *et al.* (2011) studied the sheet thickness, tool diameter and failure mode and concluded that, for small tool diameters, fracture occurs by direct ductile fracture, while for larger diameters, necking is only postponed. Madeira *et al.* (2015) confirmed this behaviour, supporting dynamic bending as the cause of necking stabilization, and proposed that the strains at failure should be obtained through thickness measurements along the cracks. They observed that even for large tool radii, in the presence of necking, the fracture strains were located at the FFL.

More recently, Centeno *et al.* (2014) performed a formability analysis on AISI304 sheets and compared stretch-bending with SPIF. The formability limits obtained were above the FLC and showed that the formability increase was much larger in SPIF than in the S-B tests. For this reason, the enhanced formability cannot be explained only by the bending effect. They also found that the fracture points in the S-B tests were in the scatter band of the FFL obtained by Nakazima tests, while the fracture points in SPIF were actually above the FFL. The authors also hypothesized that triaxiality could be related to the observed increased formability.

2.2.2.3 Stress triaxiality

Many authors have discussed the role of stress triaxiality in the increased formability. Apart from the strain intensity, it is probably the most important factor upon which the initiation of ductile fracture depends. The reason is that triaxiality is directly related to void growth, conditioning ductile fracture, as noted by McClintock (1968) in a publication that analysed cylindrical and spherical voids subjected to different loads. Rice and Tracey (1969) also analysed this phenomenon and suggested that increasing stress triaxiality results in an exponential decrease in fracture ductility, i.e., in formability. From this perspective, Bao and Wierzbicki (2004) linked the triaxiality level to the mechanism leading to fracture in ductile materials. Using experimental and numerical results, they affirmed that in processes involving negative stress triaxiality, ductile fracture is governed by the shear mode, while for high positive triaxiality levels, void growth drives the failure mode, and between these triaxiality extremes, both shear and void growth are present, as shown in figure 2.21 (Bao and Wierzbicki (2004), Wierzbicki *et al.* (2005)).

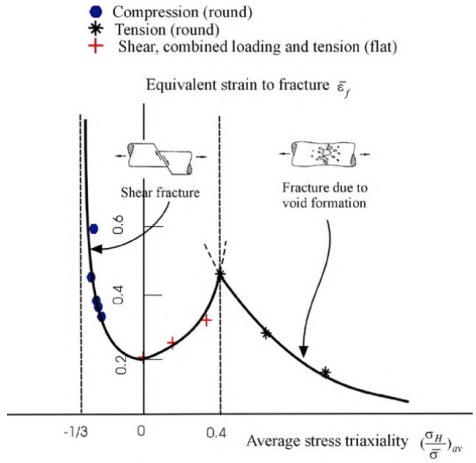

Figure 2.21. Dependence of equivalent fracture strain on average stress triaxiality (Bao and Wierzbicki, 2004).

Consequently, as in SPIF, the dominant mode that leads to fracture is mode I (Martins *et al.*, 2014), and knowing the relation between triaxiality and void growth, some authors have tried to explain the increased formability from the triaxiality perspective. For example, Malhotra *et al.* (2012) showed that the hydrostatic pressure is negative at the inner face and positive at the outer face and suggested that not only shear but also local bending explains the increased formability in SPIF. Similar results were obtained by Martínez-Donaire *et al.* (2019), who monitored the stress triaxiality evolution for both faces of the sheet in hole flanging by SPIF, showing that higher values correspond to the outer face. They concluded that the levels of triaxiality in SPIF are on average lower than those in conventional processes. This contributes to decreasing the level of damage in the material and, consequently, to increasing its formability.

2.2.3 Failure prediction in SPIF

As shown in the previous sections, the debate about the mechanism that causes the increased formability in SPIF is not closed at all. Based on the most recent studies, shear is the less supported mechanism, while bending and triaxiality effects can be considered predominant. In addition to the increasing knowledge about the deformation mechanics, failure prediction is also under study because, in the most practical sense, designers need to know the formability limits beforehand. In this

regard, failure prediction is approached basically from two different sides that are, to some extent, related to each other.

The most common experimental approach is based on modification of the well-known forming limit diagrams (FLDs) using fracture information obtained from SPIF experiments. Specifically, the SPIF formability limits of a sheet material are obtained by carrying out different SPIF tests with the purpose of obtaining fracture strains for different global relations of $\beta = \varepsilon_2/\varepsilon_1$. In this regard, a new methodology was proposed by Isik *et al.* (2014) that determines the FFL directly by means of SPIF experiments instead of measuring the gauge length in conventional Nakazima tests assuming vertical strain paths from the FLC to the FFL. The geometries employed to perform this analysis are truncated cones for the plane strain region and truncated pyramids for the biaxial zone. Both geometries have variable drawing angles, as depicted in figure 2.22, because they ensure controlled proportional strain paths up to the point of fracture.

Isik *et al.* (2014) also proposed a methodology to define the formability limits in the in-plane shear domain, i.e., the shear fracture forming limit (SFFL). The procedure is based on the realization of two tests, the twin bridge shear test proposed by Brosius *et al.* (2011) and plane shear test (figure 2.22). This ensures almost straight strain paths and the evaluation of the strains at fracture by means of thickness measurements. Later, Soeiro *et al.* (2015) proposed a simpler method to obtain the SFFL based on a new geometry produced by SPIF. The test consists of the manufacturing of a truncated lobe conical shape with a variable drawing angle (see figure 2.22) whose strain pairs at fracture determine the shear fracture limit. The main advantage of this geometry is that fracture occurs in the absence of necking; therefore, it is not necessary to perform additional thickness measurements.

A second approach to obtain the FFL was developed from the triaxiality point of view (Martins *et al.*, 2014). In a research paper, the authors reviewed the relation between the -1 slope and damage mechanics through the non-coupled damage criterion based only on void growth of McClintock (1968), also referred to as the Ayada criterion (Ayada *et al.*, 1987). This insight establishes that the stress triaxiality ratio $\eta = \sigma_m/\bar{\sigma}$ can be introduced into a modified version of the effective strain fracture criterion, obtaining equation 2.1, which can be developed and expressed as a function of the Lankford coefficient r and the strain pairs at fracture, as shown in equation 2.2.

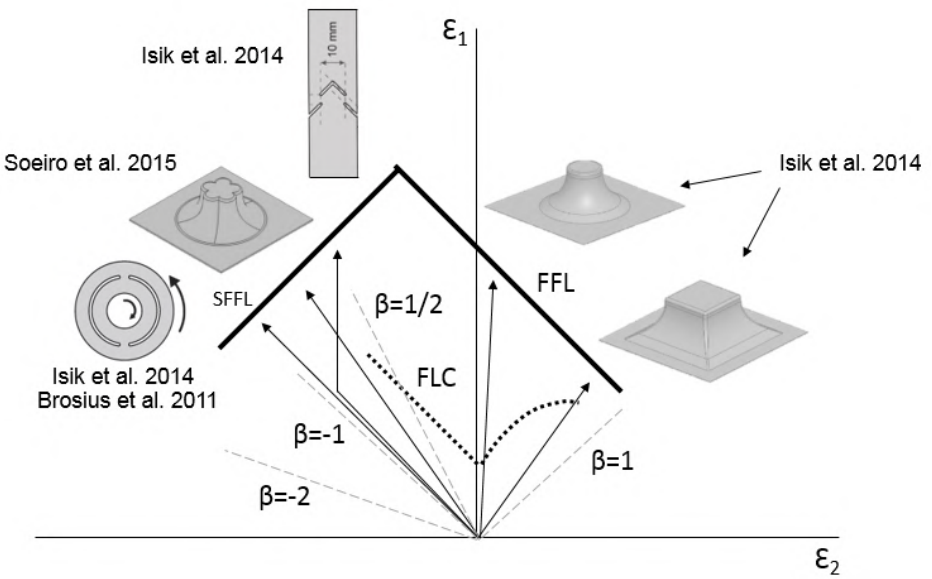

Figure 2.22. Schematic representation of the different tests proposed as a function of the strain paths obtained.

$$D_{crit} = \int_0^{\bar{\varepsilon}_f} \frac{\sigma_m}{\bar{\sigma}} \, d\bar{\varepsilon} \tag{2.1}$$

$$D_{crit} = \frac{(1+r)}{3}(\varepsilon_{1f} + \varepsilon_{2f}) \tag{2.2}$$

Equation 2.2 can be used to represent the FFL in the FLD as a line of slope -1. This agrees with the metal forming approach, which assumes that fracture occurs at a specific thickness reduction. This relation was suggested by Isik *et al.* (2014) for obtaining reliable FFL curves by using only one fracture point obtained in SPIF.

Based on the damage mechanics and triaxiality approach, some authors used SPIF FE simulations to understand the increased formability and make adjusted failure predictions. Centeno *et al.* (2017) presented an experimental study of the strain evolution of truncated conical parts and developed an FE model that was used to make failure predictions using the McClintock damage criterion. The

results showed increased formability with respect to the FFL obtained by Nakazima tests. Furthermore, the FE model was used successfully to make fracture predictions based on the evaluation of the accumulated damage D_{crit} based on dilatational void growth.

More recently, Martínez-Donaire *et al.* (2019) also showed increased formability in hole flanging by SPIF and performed a numerical FE analysis of the stress triaxiality evaluated at fracture. The results were analysed in the average stress triaxiality $\bar{\eta}$ versus equivalent plastic strain $\bar{\varepsilon}$ space (see figure 2.23), showing that the stress triaxiality involved in hole flanging by SPIF is much lower than the values obtained in Nakazima tests for a similar amount of straining. Based on the authors' description, the fracture limits in SPIF are not comparable in terms of stress triaxiality to the FFL obtained conventionally. They suggested that performing fracture predictions in the $\bar{\eta} - \bar{\varepsilon}$ space should be considered.

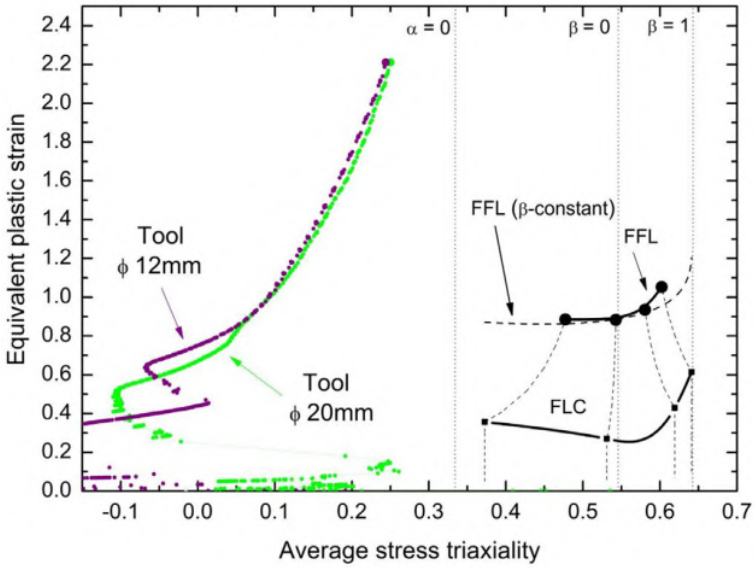

Figure 2.23. Analysis of formability in terms of the average stress triaxiality vs. equivalent plastic strain of the fracture point at the outer face for hole flanging performed by SPIF (Martínez-Donaire *et al.*, 2019).

2.2.4 Geometric accuracy

Currently, the industrial manufacturing of SPIF products is still a challenge mainly due to limitations in geometric accuracy. Simply comparing the geometric specifications in the sheet metal industry, typically close to ±0.2 mm over the hole surface of a part, with the geometric tolerances in ISF of over ±2 mm reported by Allwood *et al.* (2005) gives an idea of the magnitude of the challenge. In a review on the applications of ISF, the authors analysed the process windows of SPIF regarding, among other aspects, the geometric tolerances and feature definition for a wide range of products. They considered different parts and industrial sectors (from a car body panel to a barometric unit for aerospace), showing that 40% of the products could feasibly be produced by ISF according to feature definition criteria. The quantity was reduced to 7% when considering geometric tolerances, and only 3.5% were suitable according to both specifications.

In a further publication, Allwood *et al.* (2010) classified the geometric accuracy into three groups: the clamped accuracy when the part is still fixed in the blank holder, unclamped accuracy when it has been released and final accuracy when the part has been cut from the unwanted material. They focused on the unclamped accuracy and pointed to residual stress as the factor that most affects deviations due to the unclamped and final accuracy. In this regard, they found a way to improve the geometric accuracy consisting of starting the process from shapes partially pre-cut in their contour, as shown in figure 2.24, but with poor results. The use of a backing plate that firmly clamped the sheet during the forming process yielded better results. Micari *et al.* (2007) also made an accuracy categorization based on three defects depicted in figure 2.25: a bending effect close to the undeformed part of the sheet, a sheet springback produced after the tool retraction and a pillow effect in the base. The techniques widely used to measure these geometric deviations are 3D scanning (Ham and Jeswiet (2008), Li *et al.* (2015)) or measurement systems based on coordinates (Silva and Martins (2013a), Lu *et al.* (2016)).

Many efforts have been made to predict the shape of parts manufactured by incremental processes. Ambrogio *et al.* (2004), Ambrogio *et al.* (2007) and Han *et al.* (2013) performed experimental research on determining the influence of process parameters in ISF and used FE simulations to perform shape predictions and springback analyses. Finite element simulations were also used by Guzmán *et al.* (2012) to study the geometric accuracy. They found that the general elastic recovery of the part causes large shape deviations. In contrast, small deviations

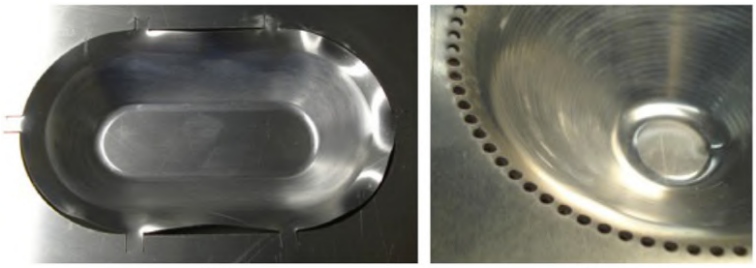

Figure 2.24. Pre-cut SPIF parts produced by Allwood *et al.* (2010) as a strategy to avoid residual stress and improve the geometric accuracy.

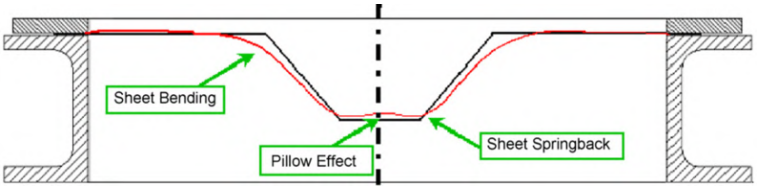

Figure 2.25. Categorization of SPIF accuracy defects as described by Micari *et al.* (2007).

were found due to localized bending caused by the tool radius.

The geometric inaccuracies found in incremental processes are counteracted by the use of different strategies presented in the literature. Some efforts have focused on the investigation of toolpath strategies to prevent shape deviations either through optimization of trajectories in a single pass or by performing multiple-pass strategies. For example, an over-depth forming tool was proposed by Ambrogio *et al.* (2007) after studying the relation between the z-increment size and springback in conical parts. Ambrogio *et al.* (2013) proposed a method based on modifying the toolpath strategy to improve the thickness distribution along the profile of the final part. Some authors observed that reducing the scallop height (Attanasio *et al.*, 2008) and variable z-increment (Attanasio *et al.* (2008) and Wang and Duncan (2011)) can be implemented in a toolpath optimization process to improve the geometric accuracy and quality. Optimization algorithms were used by Wang and Duncan (2011) and Malhotra *et al.* (2010), whose studies were based on feedback between a CAD program and measurements obtained from the part. Regarding multiple-pass strategies, Duflou *et al.* (2007a) analysed simple and double-pass strategies, performing a pre-shape pass followed by a finishing pass to improve the geometric accuracy. An industrial application of multi-pass strategies was suc-

cessfully applied by Bambach *et al.* (2009) to manufacture a car fender in a cyclic process based on stress relief and forming steps.

Finally, additional research has also been carried out on modifying the process itself by introducing additional tools or dies. For example, Attanasio *et al.* (2008) and Franzen *et al.* (2009) used extra dies to optimise the toolpath with the purpose of improving the dimensional accuracy and surface quality in TPIF.

2.3 Sheet flanging by SPIF

The application of SPIF to produce flanged parts is a relatively new process under development over the last decade. In this period, the interest of the scientific community in flanging by SPIF increased, with the aim of benefiting from the advantages of incremental deformation.

A priori, SPIF can be applied to produce the principal types of flanges previously shown in figure 2.3. Nevertheless, most investigations focus on hole flanging, and much fewer studies are found on stretch flanging or shrink flanging.

This section aims to summarize the main contributions related to these three types of geometries available in the literature. To contextualize flanging by SPIF, conventional flange forming processes such as rubber forming or press working are also analysed.

2.3.1 Hole flanging

The hole flanging process by SPIF transforms a previously holed sheet into a flanged part. This operation is carried out incrementally using a forming tool that follows pre-established trajectories, typically on a non-dedicated CNC machine.

Pioneering research in this field was presented by Cui and Gao (2010). They analysed three different strategies based on multi-stage forming and discussed the effects by comparing the results in terms of the maximum flange height achievable, forming limit ratio and uniformity of the wall thickness. Figure 2.26 shows the different results obtained from three forming strategies performed on a pre-cut hole. In strategy a), the wall angle is kept constant and equal to 90°; in strategy b), θ increases with each step up to 90°, and strategy c) combines a) and b). In this analysis, strategy a) achieved a higher limiting forming ratio (LFR_max) and a more uniform thickness distribution.

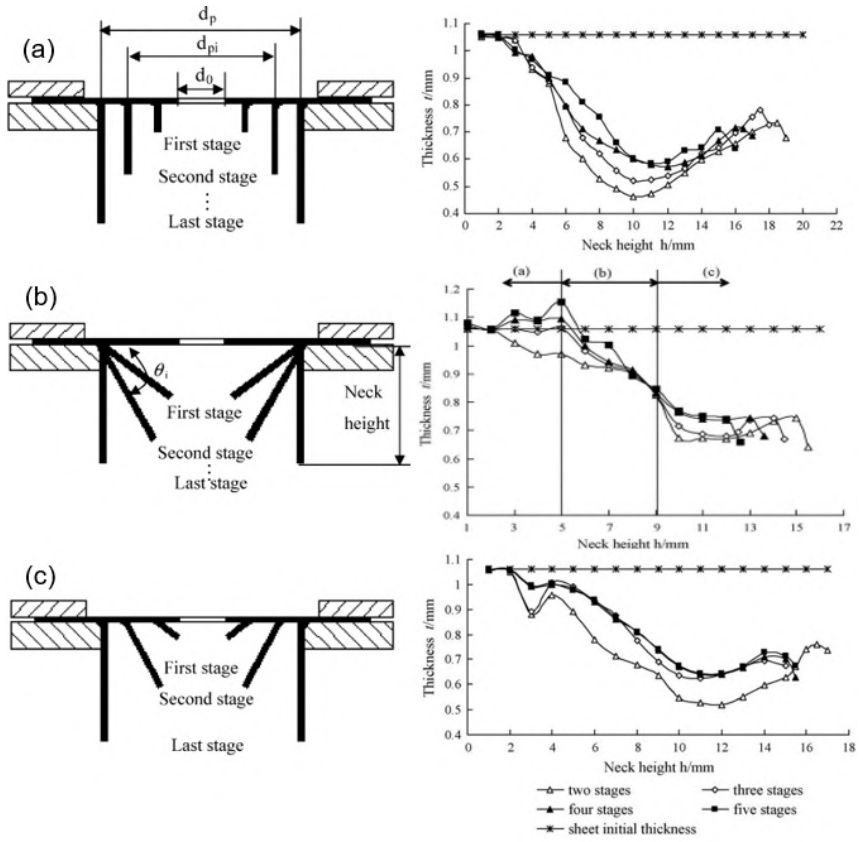

Figure 2.26. Different strategies analysed by Cui and Gao (2010) and obtained results in terms of thickness distribution and neck height.

Later, in 2012, Centeno *et al.* (2012b) published a reference study on hole flanging that analysed the relation of the hole flanging ratio, the strain evolution and the mode of failure. The authors manufactured conical (figure 2.27a) and cylindrical (figure 2.27b) hole flanges using multi-stage strategies to experimentally evaluate the strains in the FLD. It was concluded that the pre-cut hole diameter does not influence the formability of the process for the hole flanges that fractured at the edge. In contrast, for large pre-cut holes, the strains achieved at the edge were responsible for failure by fracture, as is typical in conical parts without pre-cut holes.

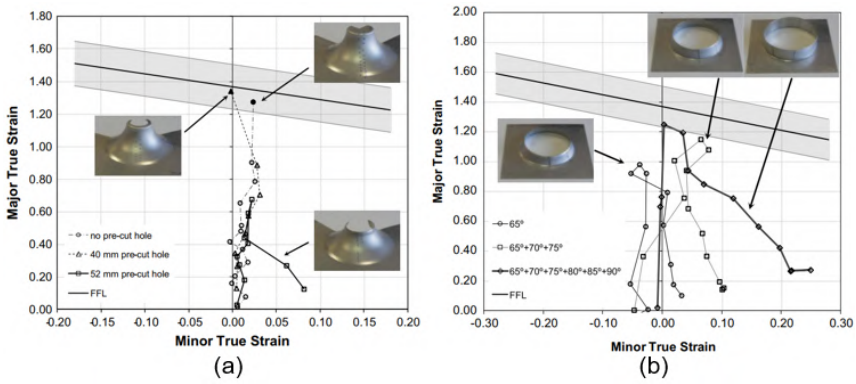

Figure 2.27. Results obtained by Centeno *et al.* (2012b) from different hole flanging experiments using SPIF multi-stage strategies applied to (a) conical hole flanges and (b) cylindrical hole flanges.

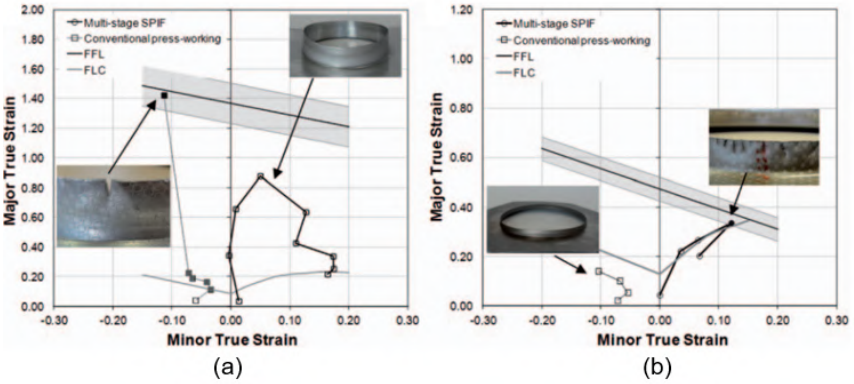

Figure 2.28. Results from conventional and incremental hole flanging for two different materials presented by Silva *et al.* (2013b): (a) aluminium with a higher limiting forming ratio achieved in SPIF compared to the conventional process and (b) titanium, with the opposite effect.

Additionally, based on multi-stage strategies, the works of Silva *et al.* (2013b) and Montanari *et al.* (2013) provided interesting contributions to the understanding of the plastic flow and modes of failure in the hole flanging process by SPIF of aluminium sheets. Silva *et al.* (2013b) showed that the limiting forming ratio is not always higher in incremental forming compared to the conventional hole flanging process, an affirmation that is contrary to the information found in the

literature. They found that under specific operating conditions, higher formability can be observed in conventional hole flanging for some materials, such as the titanium they analysed. Cristino *et al.* (2014) analysed the fracture mechanism and crack initiation in hole flanging by SPIF and proposed a new technique to evaluate the critical values of fracture toughness using different damage laws based on accumulated damage criteria.

From a technological point of view, Bambach *et al.* (2014) made two important contributions to the incremental flanging process. The first was the use of a localised backing plate acting in the vicinity of the forming tool, which enabled a reduction of unwanted deformations and therefore undesired deviations in the final geometry. The other contribution was the design of a forming set-up that allowed high-speed operations to be performed to reduce one of the drawbacks of incremental forming, the high time consumption. The set-up and tool designs are shown in figure 2.29a-b. Along this line, another experimental configuration shown in figure 2.29c-d was proposed by Cao *et al.* (2016). They designed a new flanging tool with the purpose of avoiding excessive sheet thinning and favouring a more homogeneous thickness distribution. These new designs showed a more uniform thickness distribution than the usual hemispherical SPIF forming tool.

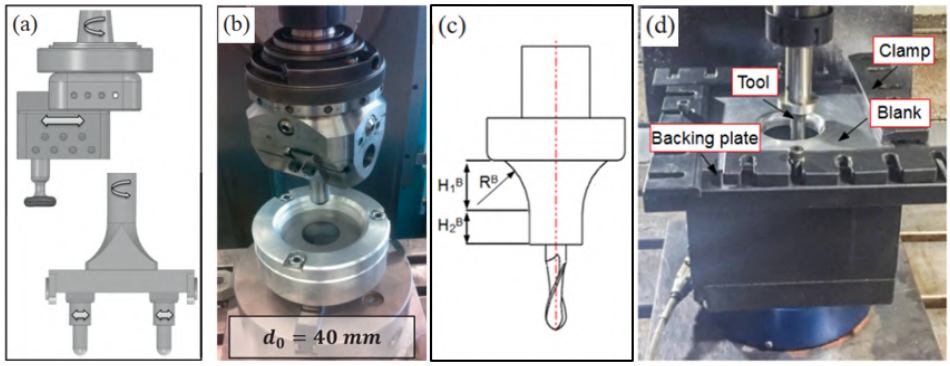

Figure 2.29. Different incremental hole flanging technological contributions: (a) and (b) principle and alternative tool designs and experimental set-up proposed by Bambach *et al.* (2014) and (c) and (d) forming tool and experimental set-up proposed by Cao *et al.* (2016).

Studies on incremental hole flanging focusing on multiple strategies are very expensive from the time consumption point of view. To avoid this disadvantage, Borrego *et al.* (2016) analysed the use of single-stage strategies in hole flanging

by SPIF. In their study, they performed multiple experiments by changing the main parameters, such as the initial and final diameters of the hole and the tool diameter. The strains and the thickness distribution of the resulting parts were analysed using circle grid analysis and microscopy, showing high amounts of thinning and stretching in the flange wall (figure2.30). In a more recent research paper of Morales-Palma *et al.* (2018), different two-stage strategies were analysed numerically. The results obtained showed more uniform thickness compared to single-stage hole flanging and shorter fabrication time compared to other multi-stage strategies.

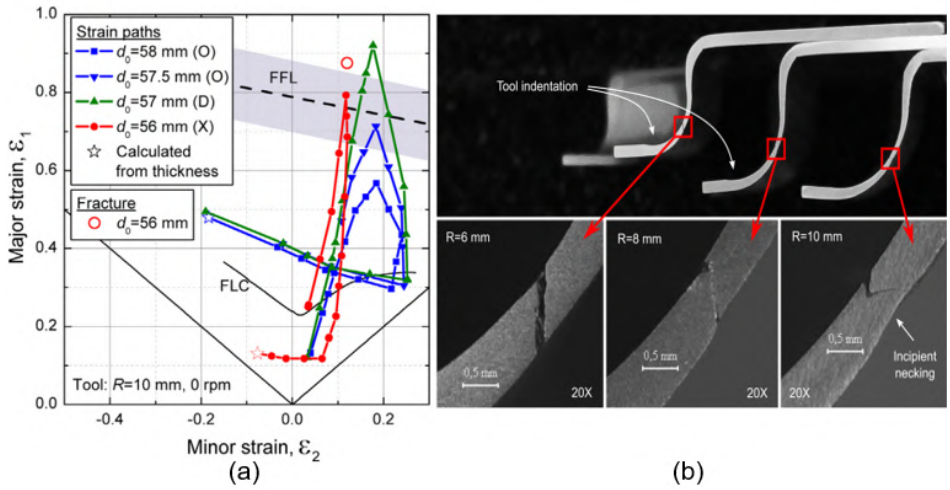

Figure 2.30. Hole flanging by SPIF in a single stage performed by Borrego *et al.* (2016): (a) strain analysis within the FLD of hole flanges processed by SPIF and (b) details of fractured specimens.

2.3.2 Open flanging: stretch and shrink

The number of studies on the fabrication of open flanges by SPIF in any of its variants (stretch or shrink flanging) is currently limited compared to the information found about hole flanging. A possible reason is that open flanges formed incrementally do not have a large presence in industry yet due to the recent development of this technology. Consequently, the manufacturing of this type of flange is already associated with more conventional processes, such as rubber forming or press working. In this context, the application of SPIF is still an interesting field

to be explored from either the scientific or industrial point of view.

One of the first investigations related to stretch flanging was performed by Wang and Wenner (1974). In this paper, the authors used numerical procedures to calculate the stress and strain distribution in sheet metals flanged by press working and obtained the maximum strain as a function of geometric variables. Although it was formulated for an axisymmetric flanging case, this approximation showed a good correlation with experimental data.

An additional effort on the prediction of strains was published by Dudra and Shan (1988). They developed a finite element model for axisymmetric stretch flanging and another model for a non-axisymmetric case (open stretch flanging). The models were used to make geometry predictions and optimize the shape of the sheet prior to the forming process to obtain the target geometry.

The first study on incremental forming of open flanges was performed by Powel (1990). In his work, Powell investigates the feasibility of producing convex geometries by repeated localized deformation. His study consisted of the simulation and experimental validation of the manufacturing of a shrink flange using the process depicted in figure 2.31a. This process was modified in Powell and Andrew (1992) using the grooved roller ball presented in figure 2.31b. Both studies demonstrated that incremental forming had sufficient potential to produce successful shrink flanges, avoiding many of the disadvantages associated with the use of dedicated tooling.

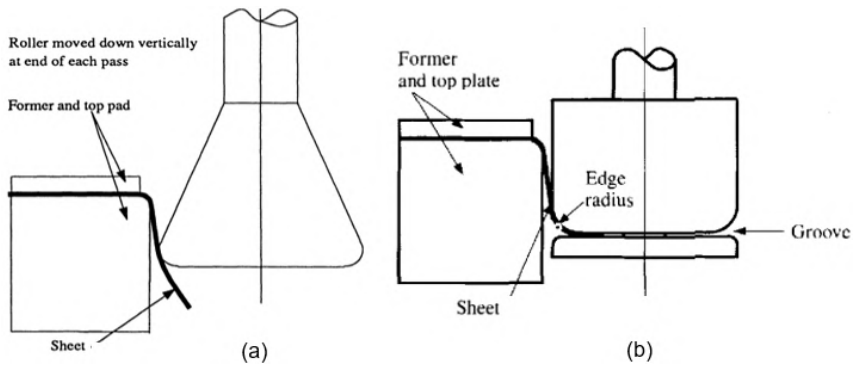

Figure 2.31. Incremental methods of forming shrink flanges without dedicated tooling: (a) first design presented by Powel (1990) and (b) second design presented by Powell and Andrew (1992).

The work presented by Asnafi (1999) studied stretch and shrink flanging by

fluid forming from different approaches. In an analytical analysis, it was noted that fracture is driven by the plastic strain at the edge of stretch flanges, which depends on the strain ratio R and the hardening exponent of the material n. Additionally, the analytical results were reproduced experimentally and using FE models to obtain the strains at the flange edge for different initial blank radii (figure 2.32a). In shrink flanging, Asnafi (1999) performed numerical and experimental analyses and studied the conditions under which wrinkling occurs on flanges formed using different die radii. The fluid pressure was found to play an important role in the formation of wrinkles, as shown in figure 2.32b. In particular, higher pressure was shown to increase the wrinkling limit.

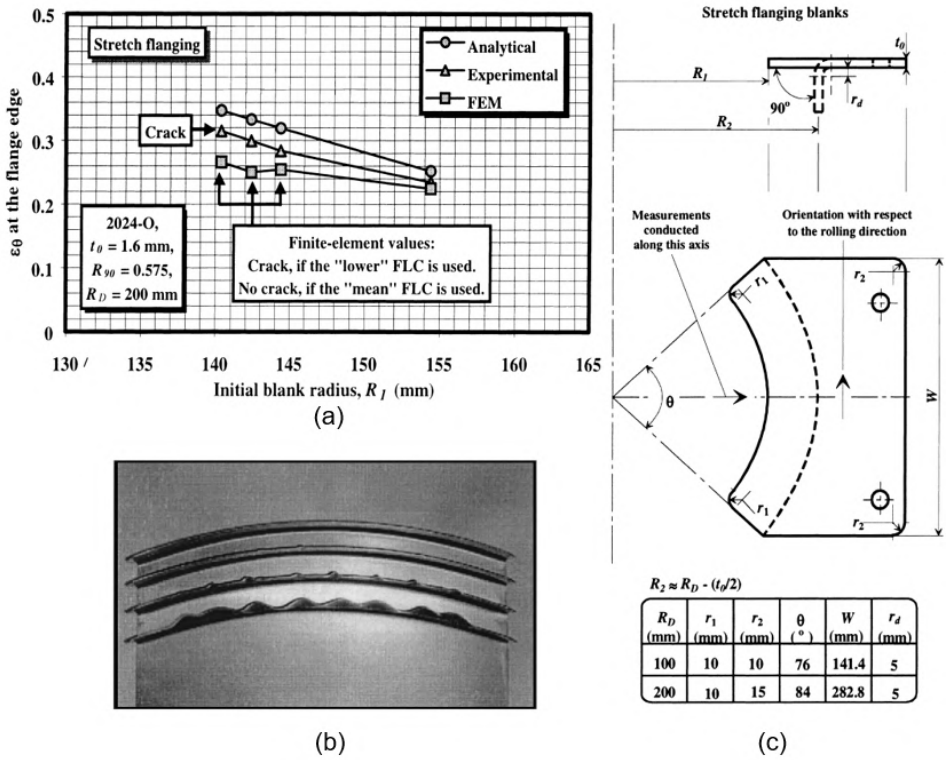

R_D (mm)	r_1 (mm)	r_2 (mm)	θ (°)	W (mm)	r_d (mm)
100	10	10	76	141.4	5
200	10	15	84	282.8	5

Figure 2.32. (a) Circumferential strain at the flange edge versus initial blank radius for stretch flanges calculated by three different paths, (b) shrink flanges with wrinkles at different maximum pressures and (c) blank design for stretch flanging. Asnafi (1999).

The wrinkling limit in shrink flanging was also studied by Wang *et al.* (2001)

using an analytical energy approach. They claimed that a large die radius and a short flange length reduce wrinkling and, in the case of failure, the number of wrinkles. Two years later, Zhang *et al.* (2003) performed experimental and analytical studies, focusing on the prediction of compression strains along the flange edge. In this case, the initial sheet metal was pre-curved, and the edge was flanged, as shown in figure 2.33.

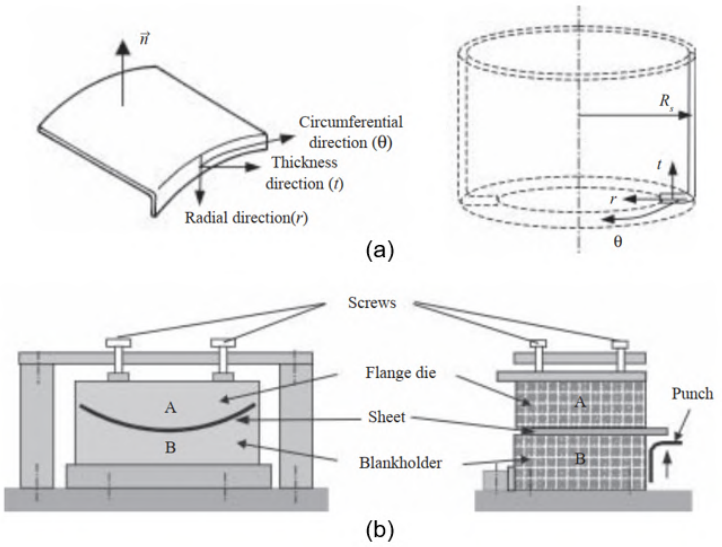

Figure 2.33. (a) Convex surface-straight edge shrink flanging and axisymmetric model and (b) experimental set-up by Zhang *et al.* (2003).

In addition to failure by fracture in stretch flanging or wrinkling in shrink flanging, some studies focusing on the elastic recovery of the flanges are found in the literature. On this topic, Chen *et al.* (2010) used FE to analyse the springback effect in stretch flanging by rubber forming. The simulations reproduced a real aircraft part and showed a good correlation with the experimental results. Similar studies on springback in shrink flanges were later performed by Chen (2011) and Chen *et al.* (2015b).

However, the paper published by Voswinckel *et al.* (2013) is the first study about the incremental stretch and shrink flanging process itself. Their analysis focused on the influence of the toolpath, flange length and flange radius and compared incremental sheet forming to conventional forming processes. They imple-

mented four path strategies, see figure 2.34b, to obtain stretch and shrink flanges using the experimental set-up depicted in figure 2.34a. In these experiments, the authors observed different modes of failure. In stretch flanges, the modes of failure observed were (i) the appearance of cracks in the region near the bending radius of the die due to the stretching and bending of the material and (ii) excessive material at the flange edge (see figure 2.35). In shrink flanges, the failures were related to bulges in the bending zone and tilting at the perimeter of the flange. As a consequence of this investigation, the incremental process was proven to increase the conventional forming limits established by Dudra and Shan (1988). The formability was measured using the ratio of the flange length to flange radii. Later, (Voswinckel *et al.*, 2014) presented a continuation of their previous work, focusing on the geometric accuracy of the flanges. The main shape deviations observed were the formation of bulges in the zone of the sheet that should be undeformed. To reduce this defect, they proposed the tool presented in figure 2.36a, which uses an adaptative moving blank holder that follows the forming punch. Figure 2.36b shows the results obtained with this new tool design.

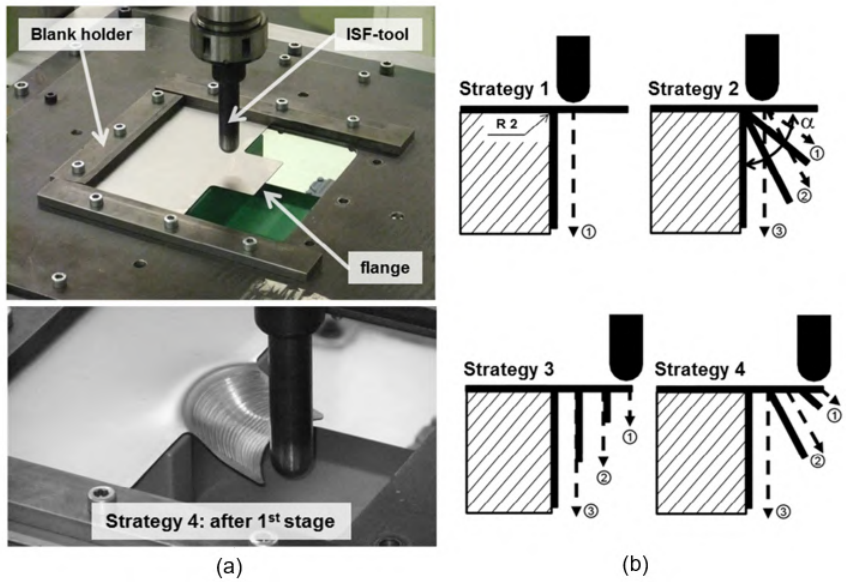

Figure 2.34. Stretch flanging process presented by Voswinckel *et al.* (2013): (a) stretch flanging set-up and incremental flanging process and (b) different toolpath strategies analysed.

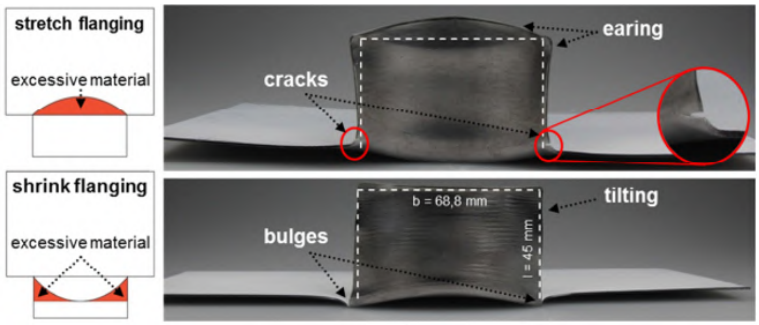

Figure 2.35. Failures in incremental forming of stretch and shrink flanges by Voswinckel *et al.* (2013).

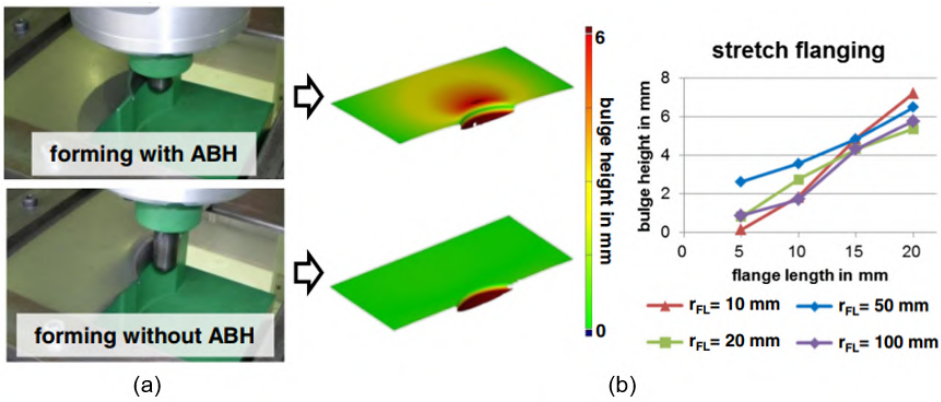

Figure 2.36. Incremental flange forming using the forming tool developed by Voswinckel *et al.* (2014). (a) Pictures of the process set-up with and without the sheet holder. (b) Comparison of the results obtained in terms of bulge height.

From a numerical perspective, Dewang *et al.* (2014c) published a review of the different parametric studies based on finite element analysis applied to open stretch flanging and hole flanging processes. They concluded that the use of explicit or dynamic methods is dominant in FE analysis of flanging processes, and most of them focused on the optimization of geometric and process parameters. Additionally, they also published three research papers based on both experimental and numerical studies of open stretch flanges (Dewang *et al.* (2014a), Dewang *et al.* (2014b), Dewang *et al.* (2017)). Very interesting results on the effect of different process parameters, such as the punch-die clearance or initial flange length, were

delivered (see figure 2.37). The typology of flanges was very similar to that in the experiments carried out in the present thesis. However, the analyses focused exclusively on non-incremental forming, opening an interesting and challenging field to be explored.

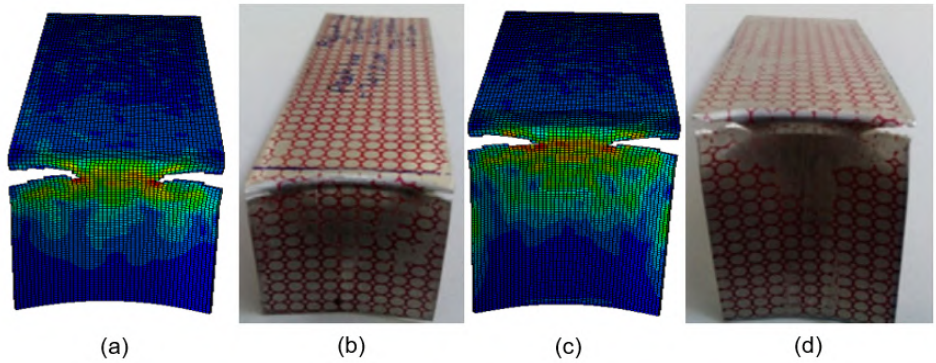

Figure 2.37. Comparison of edge crack locations for different flange lengths by Dewang *et al.* (2017). (a) Simulation (30 mm length), (b) experiment (30 mm length), (c) simulation (40 mm length), and (d) experiment (40 mm length).

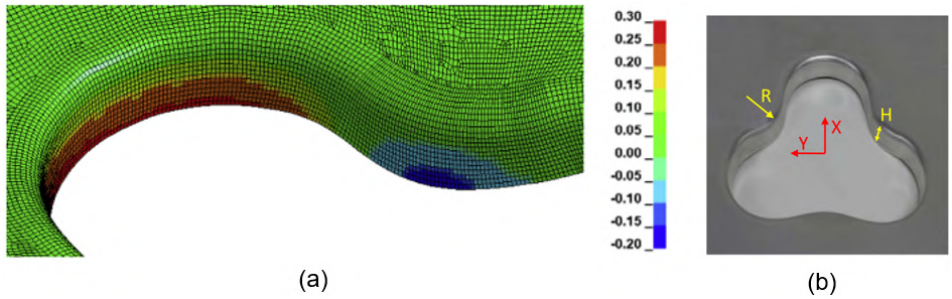

Figure 2.38. Concave and convex concatenated geometries studied by Zhang *et al.* (2018). (a) Circumferential strain obtained from the FE model and (b) formed part.

More recently, using double-sided incremental forming, Zhang *et al.* (2018) studied the deformation mechanics in fabricating a clover hole flange with complex in-plane curvatures. The part contained both stretch and shrink flange geometries. Experimental, analytical and numerical analyses were carried out, analysing the strain evolution and the failure modes observed. The strain distribution obtained from the FE analysis and one of the final flanges can be seen in 2.38. As expected,

the compression zone and the stretching zone correspond to shrink and stretch flanges, respectively (figure 2.38a).

The number of research papers focused on the study of incremental flanging and open stretch and/or shrink flanges produced by SPIF is increasing in the literature, but they are still very few compared to other common applications of ISF. Regarding the importance of the flanging processes in industry and the inherent versatility of incremental sheet forming processes, a detailed study of the capability of SPIF to produce open flanges in terms of formability, failure and strain modes and geometric accuracy deserves great interest. This analysis is the core of the current PhD thesis.

Chapter 3

Experimental procedures

This chapter describes the experimental procedures and methodology of the present work. The first section details the material properties of sheet metal AA2024-T3, including a standard tensile characterization, determination of the Lankford anisotropy coefficients and a formability analysis by using Nakazima tests. In the second section, the details of the flanging experiments are presented, describing the experimental set-up, specimen preparation and process selected. Finally, the third section presents the methodology used to analyse the flanges obtained experimentally.

3.1 Mechanical characterization

The material selected is 1.2 mm thick aluminium alloy AA2024-T3, which is widely employed for manufacturing structural components in the aircraft industry. This material has high strength and relatively low ductility and generally requires a heat treatment prior to being used in a forming process. The specimens were obtained from a single batch to guarantee homogeneity.

3.1.1 Tensile test

The tensile test is one of the most common types of mechanical tests. It consists of applying a tensile force to a piece of material and measuring the stress and strain response. The objective of applying this test to AA2024-T3 sheets is to determine the elastic modulus, yield stress and anisotropy properties.

Three tests were carried out for the rolling direction (0°), transverse direction (90°) and diagonal direction (45°), obtaining a total of nine successful tests. The testing procedure was performed using the specimens shown in figure 3.1 on an INSTRON model 1196 machine at room temperature under the specifications of the standard ASTM E8/E8M – 09 (ASTM, 2009), and the strain was measured using an extensometer of 25 mm reference length. Additional strain measurements were obtained by digital image correlation (DIC) using the commercial system Aramis®. In this regard, figure 3.2 depicts the three stress-strain curves obtained for the different directions. There is no large difference with respect to the three rolling directions. The curve at 0 degrees was fitted using least squares to the Swift law, obtaining equation 3.1 for the AA2024-T3 sheet that was used in the numerical model.

$$\sigma = 742.36(0.025 + \varepsilon^p)^{0.235} \tag{3.1}$$

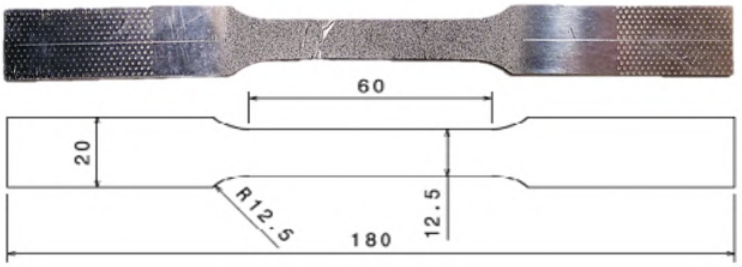

Figure 3.1. Tensile specimen.

Table 3.1 shows the average tensile properties, including yield stress σ_Y and Young's modulus E in the three rolling directions and a single averaged value of ultimate tensile strength σ_{UTS} and Poisson coefficient ν.

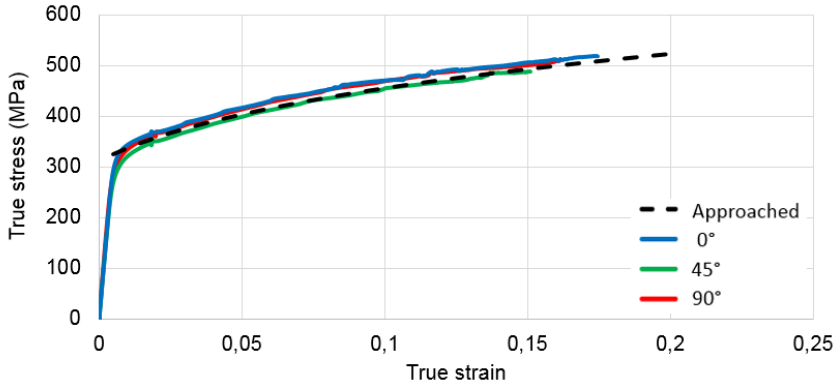

Figure 3.2. Stress-strain curve for different angles with respect to the rolling direction.

Direction	σ_Y (MPa)	σ_{UTS} (MPa)	E (GPa)	ν
r_0	336		69.4	
r_{45}	306	526	67.1	0.33
r_{90}	318		68.2	

Table 3.1. Mechanical properties at 0, 45 and 90 degrees with respect to the rolling direction.

3.1.2 Anisotropy

Previous studies by Vallellano *et al.* (2008) and later by López-Fernández *et al.* (2019) showed the anisotropic behaviour of 1.2 mm thick AA2024-T3 sheets characterized using Lankford coefficients r_i. These coefficients have been expressed by the ratio between the in-plane plastic minor strain ε_2^p and the through-thickness plastic strain ε_3^p (equation 3.2). Applying volume constancy $\varepsilon_3^p = -(\varepsilon_1^p + \varepsilon_2^p)$, the second part of the equation is obtained in terms of the in-plane plastic strains.

$$r_i = \frac{\varepsilon_2^p}{\varepsilon_3^p} \equiv \frac{-\varepsilon_2^p}{\varepsilon_1^p + \varepsilon_2^p} \tag{3.2}$$

$$r = \frac{r_0 + 2r_{45} + r_{90}}{4} \tag{3.3}$$

A series of tensile tests were carried out according to the standard ASTM (2000) at room temperature and a velocity of 1 mm/min utilizing sheet specimens with the geometry depicted in figure 3.1 3.1. The process is similar to a tensile test with three discharges equally spread along the tensile curve (see figure 3.3). At the end of each discharge, the minor strain ε_2^p and thickness strain ε_3^p were evaluated, obtaining the value of r_i (Eq. 3.2). In this case, the strain results were analysed separately using an extensometer and the DIC system Aramis® to double check the results. Furthermore, at least three valid replicates were performed for each direction with the aim of providing statistical meaning to the results. The results obtained for different directions and discharges and the average values r are summarized in Table 3.2.

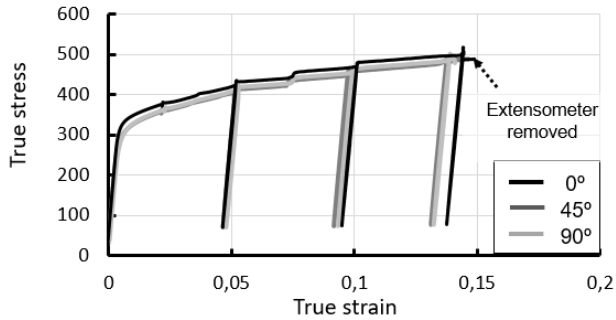

Figure 3.3. True strain vs. true stress evolution in Lankford tests for different directions with respect to the rolling direction.

	Discharge			
	1	2	3	Average
r_0	0.82	0.75	0.72	0.76
r_{45}	0.97	0.94	0.92	0.95
r_{90}	0.56	0.54	0.53	0.54
r	0.83	0.79	0.78	–

Table 3.2. Three discharge and average Lankford coefficients corresponding to 0, 45 and 90 degrees with respect to the rolling direction.

3.1.3 Formability analysis

This section describes the formability analysis carried out by means of Nakazima tests performed in the universal sheet testing machine Erichsen model 142-20 depicted in figure 3.4 using a hemispherical punch of 100 mm. The Nakazima tests were performed following the standard ISO 12004-2:2008 (2008), which describes the process for determining the forming limit curves (FLCs) under laboratory conditions. According to this standard, the velocity of the punch was set to 1 mm/s, and the rolling direction was oriented longitudinally. To guarantee minimum friction, a set of Vaseline - PTFE - Vaseline was placed between the punch and the specimens.

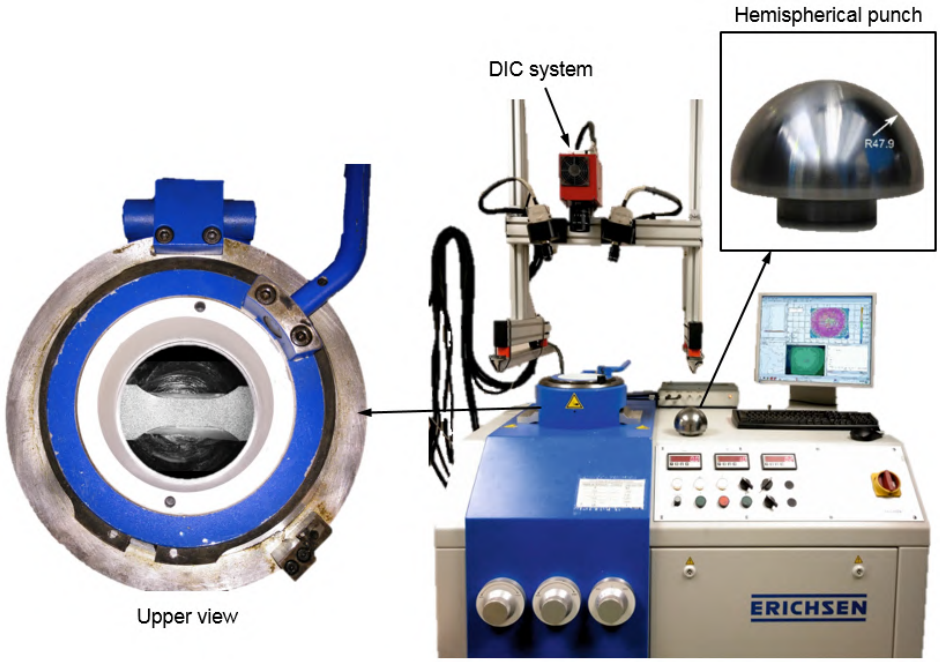

Figure 3.4. Erichsen universal testing machine.

With the aim of obtaining the FLD of the material, the 5 specimen geometries depicted in figure 3.5 were tested. Every specimen geometry was tested at less than three times, checking that fracture occurred in the region specified by the standard.

The strain evolutions corresponding to the different tests were obtained using the DIC system Aramis® version 6.3 with recording cameras of 1.3 megapixels. The frame rate was set to 12 frames per second until fracture, obtaining a number of images between 300 and 600 depending on the specimen geometry. As an example, figure 3.6 illustrates the strain analysis for a pure tension test.

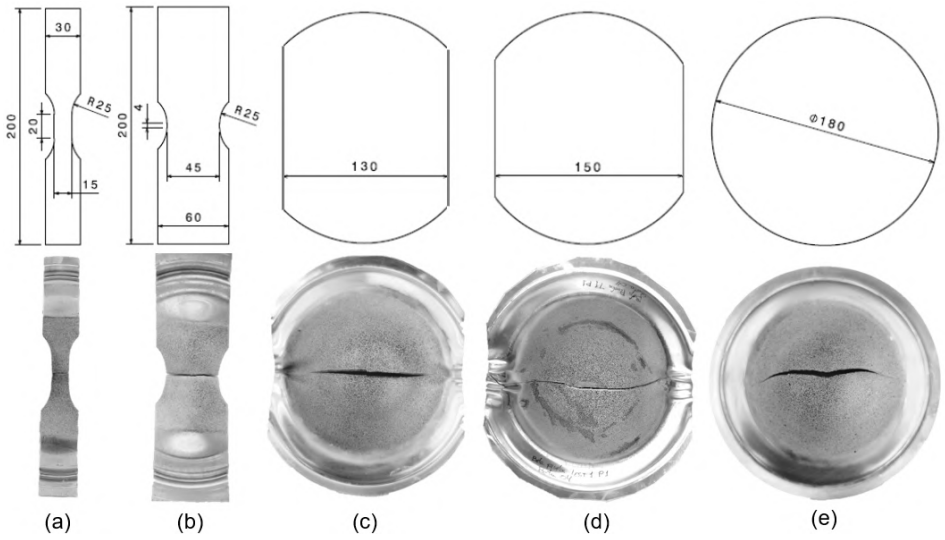

Figure 3.5. Schematic view of specimen geometries and real specimens after testing corresponding to the different strain states considered: (a) pure tension, (b) plane strain, (c) and (d) biaxial strain, and (e) equi-biaxial strain.

The methodologies followed to detect the onset of necking were both the standard ISO 12004-2:2008 (2008) and the time-dependent methodology proposed by Martínez-Donaire *et al.* (2014). Neither of them showed evidence of necking prior to fracture. Such an absence of necking agrees with the previous studies carried out by Vallellano *et al.* (2008) and Centeno *et al.* (2012a) for other batches of this material, which confirms its failure by direct ductile fracture. Consequently, this material only presents the fracture limit FFL as the formability limit within the FLD.

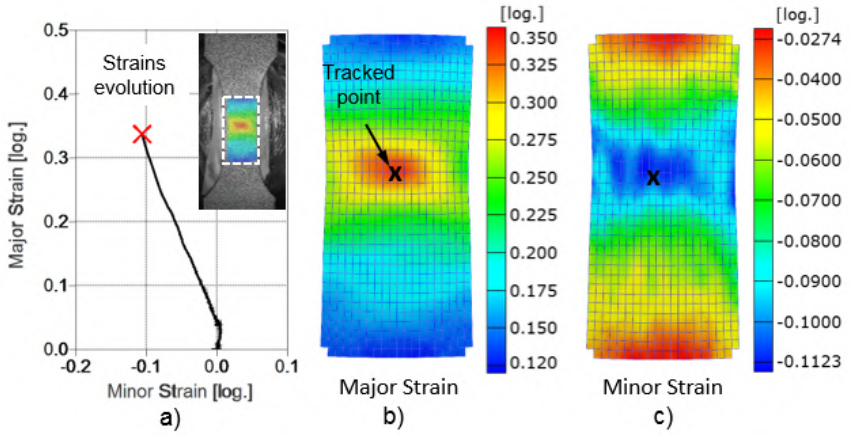

Figure 3.6. Strain analysis of the Nakazima pure tension test using Aramis®: (a) strain evolution, (b) major strain in the strain stage prior to fracture and (c) minor strain in the strain stage prior to fracture.

The strains until the instant prior to fracture were obtained using the DIC system. However, there was a time lapse between the last image recorded by the DIC system and the instant of fracture in which the information could not be processed. Due to this technical limitation and because the onset of necking and fracture occurs instantly, necking and fracture strains could not be analysed using this method. Therefore, the FLCs and FFL curves were obtained indirectly by thickness measurement.

In general, the procedure to obtain the FFL using DIC in materials with necking assumes that, at necking, the minor strain ε_2 is constant. As a consequence, there is deformation only in the direction of major strain ε_1 until fracture occurs. However, in the absence of necking, the strain evolution prior to fracture is different; therefore, other methodologies must be used. In this case, the strain evolution of the fracture point is considered proportional to the principal strains until fracture, assuming a constant value of β. Using equation 3.4) and applying volume constancy (equation 3.5), only the thickness strain ε_3 is needed to place the fracture point in the FLD.

The thickness strain at fracture was obtained by applying equation 3.6, where t_f is the thickness at fracture in the vicinity of the crack and t_0 is the initial thickness of the sheet. To obtain an average value of t_f, every specimen was cut perpendicular to the fracture. Then, a number of thickness measurements were

performed using a NICON SMZ800 microscope and the software KAPPA Image Base Metreo version 2.7.2. From these thickness measurements, the values of ε_3 corresponding to the Nakazima tests were obtained.

$$\beta = \frac{\varepsilon_2}{\varepsilon_1} \tag{3.4}$$

$$\varepsilon_3^p = -(\varepsilon_1^p + \varepsilon_2^p) \tag{3.5}$$

$$\varepsilon_{3f} = \log \frac{t_f}{t_0} \tag{3.6}$$

Finally, from the values of ε_3 obtained using equation 3.6, applying volume constancy (equation 3.5) and substituting the beta value from the Nakazima strain paths into equation 3.4, the fracture strains of the Nakazima tests were obtained. These fracture strains are represented using black filled points in the FLD depicted in figure 3.7. The FFL is represented by connecting these points, and the strain paths of Nakazima tests corresponding to different specimen geometries are shown using dotted lines. Additionally, the last strain points obtained using DIC are represented using white circles.

It must be noted that, assuming the von Mises criteria for isotropic materials, the uniaxial strain path ($\alpha = \frac{\sigma_2}{\sigma_1} = 0$) coincides in the FLD with the line $\beta = -0.5$ presented in figure 3.7. This value is obtained from the relation between α and β expressed by equation 3.7. However, if anisotropy exists, then the expression of β depends on the yield criterion. For the AA2024-T3 sheets used in this study, β was obtained using equation 5.28, which is based on Barlat's 89 anisotropic yield criterion that will be described in chapter 5. Using equation 5.28 and substituting $\alpha = 0$, the strain ratio $\beta = -0.43$ for uniaxial tension represented in 3.7 is obtained.

$$\beta = \frac{2\alpha - 1}{2 - \alpha} \tag{3.7}$$

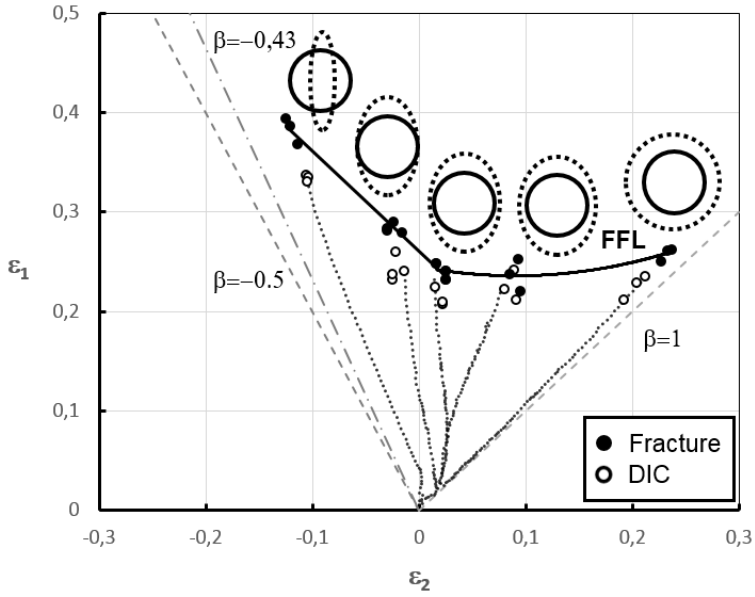

Figure 3.7. Forming limit diagram of AA2024-T3 represented by the FFL obtained from Nakazima tests considering five different strain paths.

3.2 Flanging process by SPIF

3.2.1 Experimental plan

The experimental plan consisted of different flanging experiments performed by SPIF. The tests were classified into two groups: stretch flanges (or concave flanges) and shrink flanges (or convex flanges). The objective of this experimental campaign is to provide a large set of flanges manufactured with a wide range of process parameters with the aim of providing an overall analysis of the flanging process by SPIF.

The parameters considered in the experiments were classified into geometric and process parameters. The geometric parameters are related to the specimen dimensions and the geometry of the forming dies, e.g., the initial width or length of the specimen and the die principal radius, respectively. The process parameters are related to the variables of the forming process, such as the spindle speed or the step down Δz. In this regard, six different parameters for stretch and shrink flanges were considered: die principal radius (R_{die}), initial width of the flange

(w_0), initial length of the flange (l_0), diameter of the forming tool (ϕ), spindle speed (S) and step down (Δz). These parameters and their values considered in the experiments are shown in table 3.3 for the stretch flanges and table 3.4 for the shrink flanges. It should be noted that the values of w_0 correspond to the die radius R_die multiplied by a factor between 1 and 2, e.g., $w_0 = 73$ mm is the result of $R_{die} = 45$ mm multiplied by 1.6. The experiments were carried out using a step down of 0.4 mm per pass. A smaller step down $\Delta z = 0.2$ mm was also tested, initially obtaining similar results but a longer processing time.

Note that at least two replicates were performed for each set of process parameters to provide statistical meaning. In this context, the number of possible parameter combinations is 280, resulting in more than 500 tests. However, the final number of experiments was lower because the less relevant tests, i.e., flanges far from failure, were removed from the initial experimental plan. The complete set of experiments carried out is intensively described in chapter 6.

Stretch flanges

Geometric parameters			Process parameters		
R_{die} (mm)	w_0 (mm)	l_0 (mm)	ϕ (mm)	S (rpm)	Δz (mm)
20	20, 24, 28, 32, 36	15, 20, 25	12, 20	20, 1000	0.2, 0.4
45	36, 45, 54, 63, 72	15, 20, 25, 30	12, 20	20, 1000	0.2, 0.4

Table 3.3. Experimental parameters in stretch flanging.

Shrink flanges

Geometric parameters			Process parameters		
R_{die} (mm)	w_0 (mm)	l_0 (mm)	ϕ (mm)	S (rpm)	Δz (mm)
20	20, 24, 28, 32, 36	15, 20, 25	12, 20	20, 1000	0.2, 0.4
45	36, 45, 54, 63, 72	10, 15, 20, 25	12, 20	20, 1000	0.2, 0.4

Table 3.4. Experimental parameters in shrink flanging.

The preparation of the specimens includes a number of steps. In this process, received aluminium sheets of 1x2 metres were cut into rectangles using a shearing machine, leaving an excess of material for further operations. Afterwards, the rectangles were stacked and machined in a manual drilling machine to add positioning grooves and guarantee parallelism between the corresponding edges. To remove

imperfections at the perimeter of the specimens, the edges were polished using sandpaper of successive decreasing grain size corresponding to sandpaper numbers from 500 to 4000.

As will be revealed in the following sections, the deformed flanges were analysed using circle grid analysis. This process requires the flanges to be electro-etched with a circle grid. The etching process was performed using the electrolytic marking system EU-Classic 300 from Ötsling Marking Systems shown in figure 3.8a, which provides AC/DC current from 0-24 V. This technology consists of the application of electric currents to the surface of the sheet using an electrode and an electrolytic solution. The stencil containing the pattern to be printed was placed between the electrode and the sheet. In this regard, figure 3.9 shows the two patterns with 1 mm and 1.5 mm distances between circles that were used with fair results in this study. To increase the contrast of the circle pattern and reduce the brightness, the specimens were submerged in a solution with a composition of 93.5% H2O, 1.5% HCl, 2.5% HNO3 and 2.5% HFl prior to the etching procedure. In this case, neither a thickness reduction nor a variation in mechanical properties were observed as a consequence of the etching process.

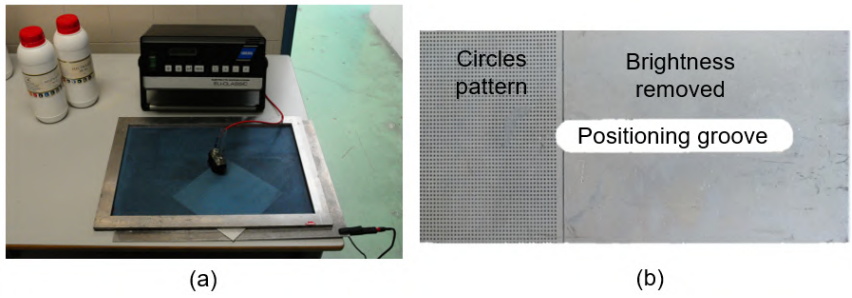

Figure 3.8. (a) Electrolytic marking machine. (b) Flanging specimen after the etching process.

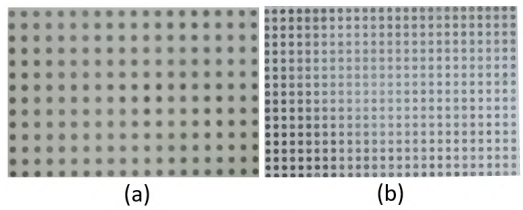

Figure 3.9. Grid patterns with (a) 1.5 mm and (b) 1 mm distances between points.

3.2.2 Experimental set-up

The SPIF flanging experiments were performed on an EMCO VMC-200 3-axis CNC milling machine. In this regard, figure 3.10 shows the different elements of the experimental set-up, including the forming die and sheet holder, the dynamometer, the forming tool, the fixing tools and the cooling system.

The two sets of forming dies and sheet holders corresponding to die radii of 20 mm and 45 mm are depicted in figure 3.11. They were obtained from a 10 mm thick steel plate using laser cutting and had a number of holes used for positioning and fixing the specimen. Each set had concave and convex radii to produce both flange geometries using a single die. The SPIF process was carried out using two hemispherical tools with 6 mm and 10 mm radii, as depicted in figure 3.12. The feed rate of the tool was set to 1000 mm/min for all experiments, and the tool rotation was set to either 20 rpm or 1000 rpm depending on the experiment.

For the selection of the lower spindle speed, the initial idea was to allow free rotation of the forming tool to guarantee as little friction as possible. However, this option was not possible on the CNC machine used for the experiments.

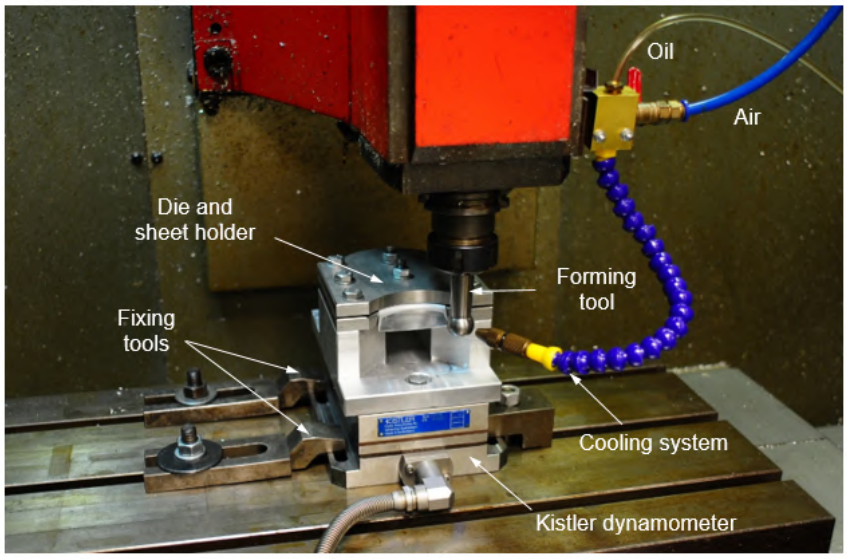

Figure 3.10. Experimental set-up used in the SPIF flanging experiments.

In this regard, a number of tests were carried out with the spindle speed set to 0 rpm, with low surface quality. Finally, the lower spindle speed was set to 20 rpm because it led to acceptable surface quality.

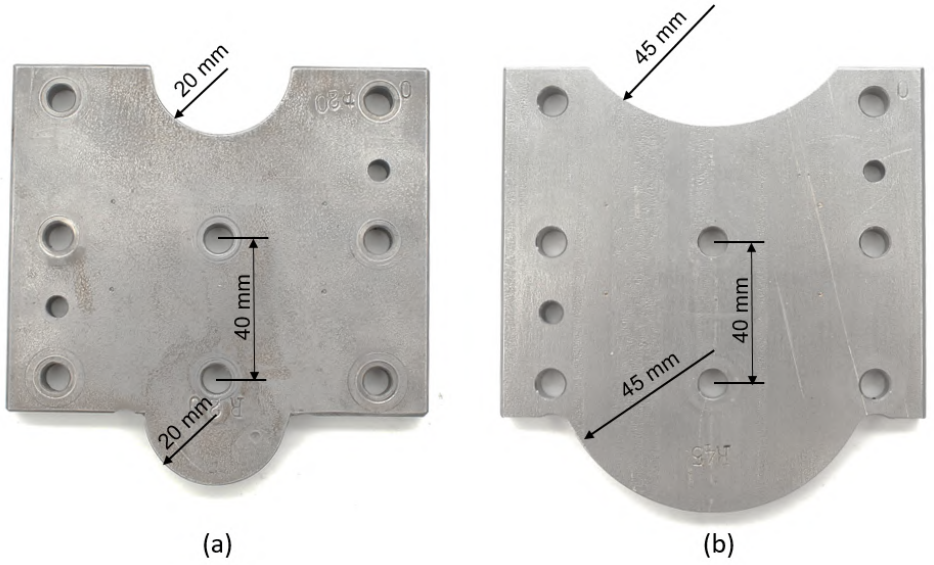

Figure 3.11. Upper view of the dies with (a) $R_{die} = 20$ mm and (b) $R_{die} = 45$ mm.

During the tests, the tool describes a pattern of circumferential arcs concentric with the die radius followed by step downs along the z axis. In this regard, at the end of each circumferential displacement, the tool loses contact with the flange, and it is at this point when the z decrement is implemented (see figure 3.13). With respect to the CNC language, ISO Code was used. However, due to the variety of geometries analysed, the trajectories for the different experiments were obtained using MATLAB®. The radius described by the tool was calculated for stretch and shrink flanges using equation 3.8. In this equation, R_t is the radius described by the tool, R_{die} and ϕ_{tool} are the radius of the die and radius of the tool, respectively, and t is the sheet thickness. Furthermore, the parameter Δr represents the clearance of 0.2 mm left to avoid possible ironing, and the symbol $\pm$ was set to $-$ or $+$ depending on the concave or convex shape, respectively. The duration of the test varied depending on the radius, width and length of the flange, although it was 3 minutes in the shortest test and 20 minutes in the longer case.

$$R_t = R_{die} \pm \phi_{tool} \pm t \pm \Delta r \tag{3.8}$$

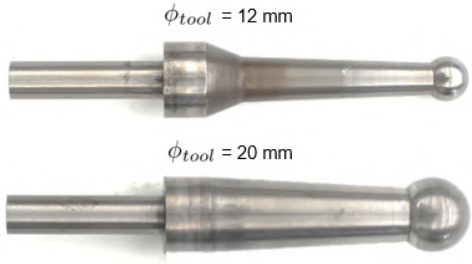

Figure 3.12. Two forming tools used in the SPIF experiments.

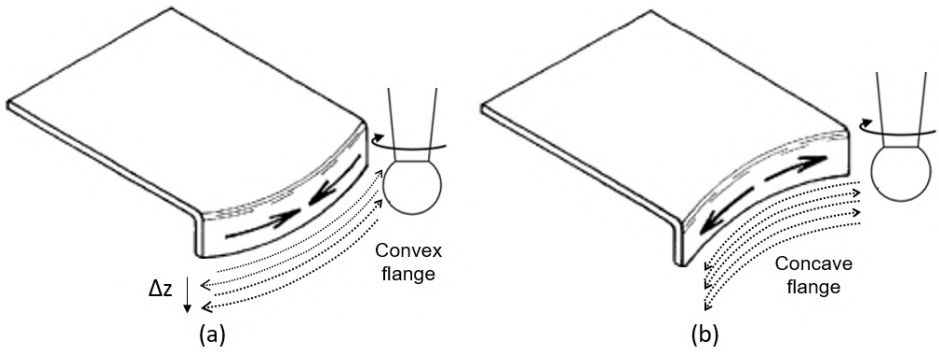

Figure 3.13. Scheme of tool trajectories for (a) a shrink flange and (b) a stretch flange.

To minimize the friction between the tool and the sheet blank, commercial lubricant Castrol Iloform TDN81 was continuously spread over the tool surface. This oil is recommended for metal forming processes and shows successful results at low spindle speeds. Nevertheless, it was observed that for a spindle speed of 1000 rpm, its viscosity increases as a consequence of the temperature. To avoid this inconvenience, the lubricant was mixed with pressurized air and spread using the device shown in figure 3.14. This system reduced the temperature, providing a more homogeneous and effective distribution of the oil.

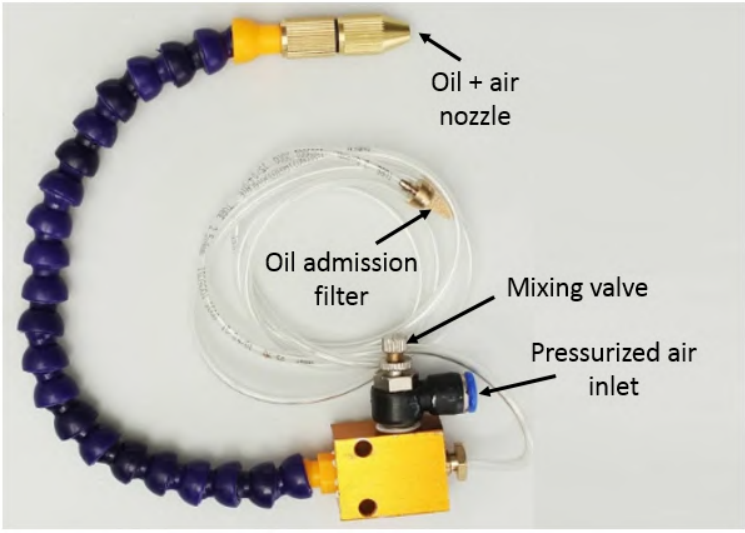

Figure 3.14. Lubrication system used in the SPIF experiments.

3.3 Formability analysis

This section details the methodologies used to perform formability analysis of the stretch and shrink flanges produced by SPIF. In the first section, the experimental techniques for the strain analysis will be discussed, showing examples of stretch and shrink flanges. In the second section, the failure modes observed for both types of flanges will be described.

3.3.1 Strain analysis

Strain analysis was performed using the circle grid analysis commercial system Argus®. The CGA technique is based on measuring the distortion of a grid etched on the surface of the sheet metal. This grid usually consists of a pattern of circular points that were drawn on the sheet surface prior to the test. After the forming process, the specimens were placed together with several coded points used as references (figure 3.15). Then, a number of photographs were taken from different positions using a high-resolution camera. Finally, these pictures were analysed using Argus® software, obtaining the principal strains from the surface of the sheets.

The results of the strain analysis for each specimen were represented using the

FLD and the principal strain contours, as depicted in figure 3.16 and figure 3.17 for a stretch flange and a shrink flange, respectively. In these examples, the major and minor strain 3D contours along with their respective directions are presented (figure 3.16b and figure 3.17b). The strain distribution of the flanges was depicted within the FLD using points coloured as a function of the thickness reduction, as shown in figure 3.16a and figure 3.17a. Additionally, the strains corresponding to the most representative sections were highlighted in the FLD. These sections were also displayed in the strain contours.

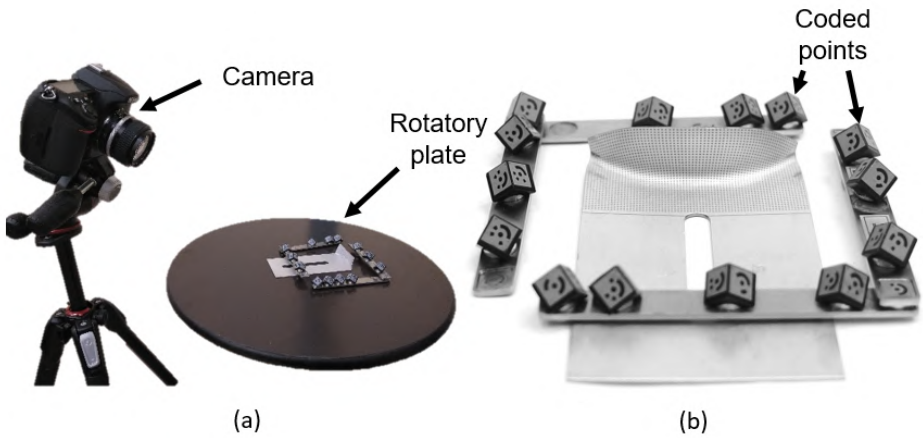

Figure 3.15. Argus® measurement configuration. (a) Elements involved in the measurement process. (b) Example of a stretch flange and coded point distribution.

It is important to remark on two additional points regarding the strain analysis. First, the strain data were obtained from the surface that was not in contact with the tool. Therefore, the strain data from the numerical model described in chapter 4 were obtained from this surface. Second, the CGA technique needs four points from the grid to interpolate the strains in between. As a consequence, the strains located at the edge of the flange cannot be analysed. For the flanges analysed, the distance from the last point measured using CGA to the edge of the flange was approximately 0.5 mm.

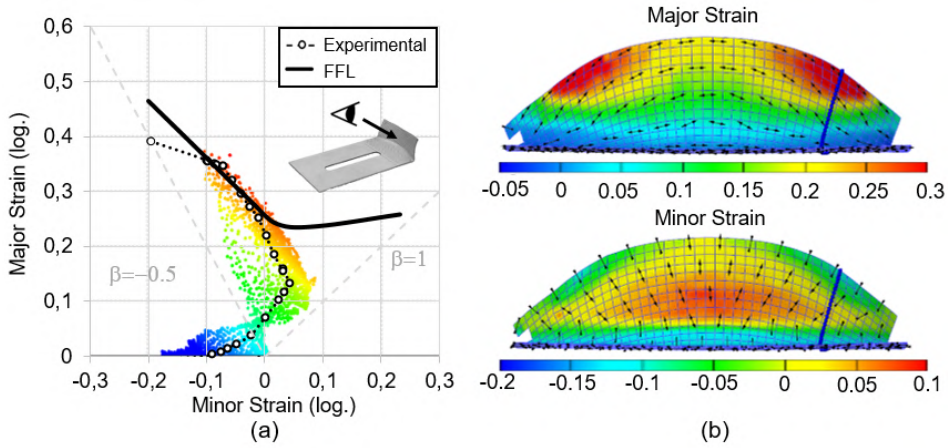

Figure 3.16. Strain analysis of a stretch flange produced by SPIF. (a) Strain points and section on the FLD. (b) Strain contours.

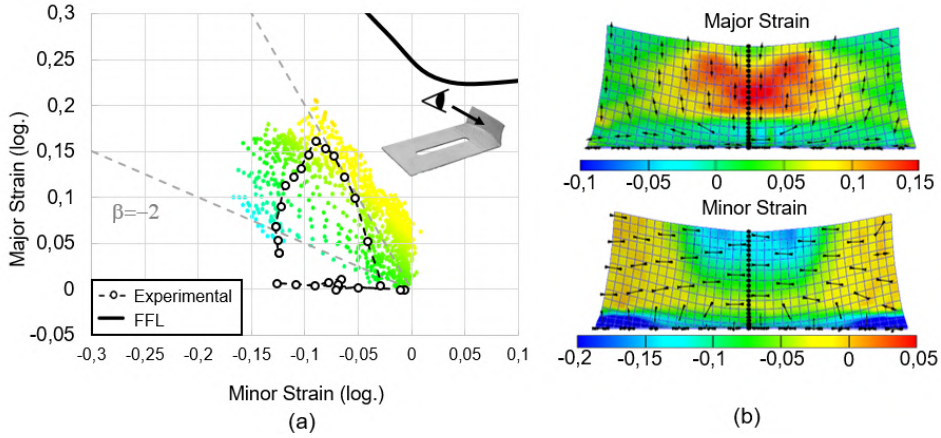

Figure 3.17. Strain analysis of a shrink flange produced by SPIF. (a) Strain points and section on the FLD. (b) Strain contours.

Because the strain data from the edge cannot be obtained using CGA, the following alternative method was used.

Under the assumption that the edge of the flange is under pure tension conditions, the strain points at the edge of the sheet should be on the $\beta = -0.5$ line for an isotropic material, which is the relation between ε_1 and ε_2 at the edge.

Furthermore, the through-thickness strain ϵ_3 was calculated by thickness measurement (equation 3.6), where ε_1 and ε_2 were obtained by applying volume constancy (equation 3.5). For the AA2024-T3 sheet analysed, the value of β corresponding to pure tension conditions obtained using Barlat's 89 anisotropy criterion was $\beta = -0.43$. Consequently, the values of ε_1 and ε_2 slightly differ from those in the anisotropic case.

3.3.2 Failure analysis

One of the main objectives of the experimental campaign is to determine whether the flanges are acceptable from a functional point of view. In this regard, two failure modes were observed in the stretch flanges, and two failure modes were observed in the shrink flanges. The flanges were classified as successful flanges or failed flanges according to their functionality.

On the one hand, the two different modes of failure observed for stretch flanging were (i) fracture at the edge and (ii) fracture at the corner. In flanges that failed by fracture at the edge, a crack was found near the edge, as depicted in figure 3.18a. This mode of failure is a consequence of the high tensile strains at the edge of the flange. As will be discussed in chapter 5, the fracture does not necessarily initiate at the very edge but may appear at a certain distance from it and then propagate toward the edge. In flanges that failed by fracture at the corner, the crack appears at the lateral edge in the region depicted in figure 3.18b. In this region, the material is stretched and experiences cyclical straining due to the multiple passes of the forming tool.

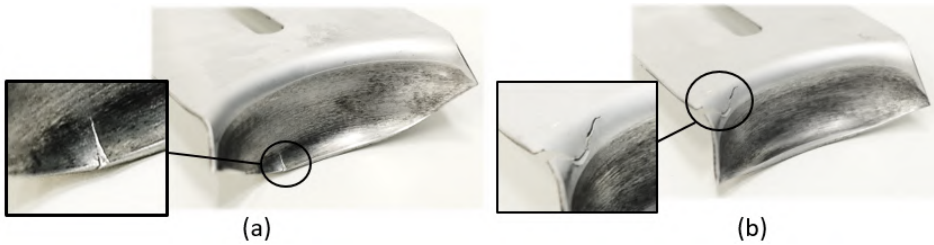

Figure 3.18. Modes of failure in stretch flanging by SPIF. (a) Fracture at the edge. (b) Major strain contour. (c) Fracture at the corner.

On the other hand, in shrink flanging, the two different modes of failure observed were (i) failure by wrinkling and (ii) failure by incipient wrinkling. For both

modes of failure, the flanges presented wrinkles, although with different intensities. In the flanges that failed by wrinkling, the wrinkles were larger and appeared at the centre of the flange. The tests corresponding to flanges that failed by wrinkling had to be stopped to avoid any damage to the forming tool. This is the case for the shrink flange shown in figure 3.19a. In contrast, in flanges that failed by incipient wrinkling, the wrinkles were smaller and usually located at some distance from the centre of the flange. These flanges had an edge with a polygonal shape instead of a circular shape, as depicted in figure 3.19b.

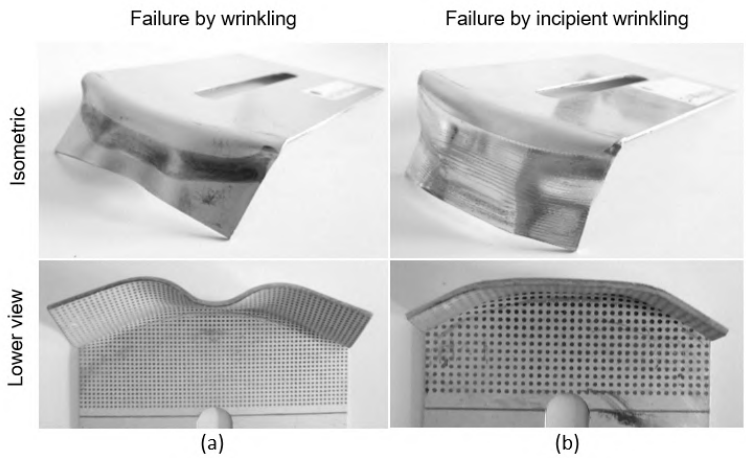

Figure 3.19. Modes of failure in shrink flanging by SPIF. (a) Failure by wrinkling. (b) Failure by incipient wrinkling.

Chapter 4

Numerical methods

This chapter describes the numerical models used to reproduce the flanging process by SPIF. First, section 4.1 describes the FE models corresponding to stretch and shrink flanging by SPIF. Second, section 4.2 presents the process to obtain the principal strain components in the plane of the sheet from the components of the strain tensor.

4.1 SPIF modelling

Numerical simulations of the flanging process by SPIF were carried out with the aim of (i) predicting the principal modes of failure attained in stretch and shrink flanging by SPIF and (ii) analysing the stress and strain conditions that produce these modes of failure. In this regard, the finite element (FE) models corresponding to stretch flanging by SPIF and shrink flanging by SPIF presented in figure 4.1 and figure 4.2 were developed. Both models were designed using the commercial software Ansys LS-Dyna® in the Ansys mechanical APDL® programming environment. The simulations were based on an explicit integration scheme.

Explicit methods are widely employed in incremental sheet forming simulations, as these approaches are more stable and faster than implicit formulations, especially in contact problems (Bambach *et al.*, 2003). A more exhaustive description of the differences between explicit and implicit methodologies can be found in (Belytschko and Moran, 2000).

The model was developed using the SHELL163 element type available in the Ansys LS-Dyna® element library, which is recommended for the simulation of

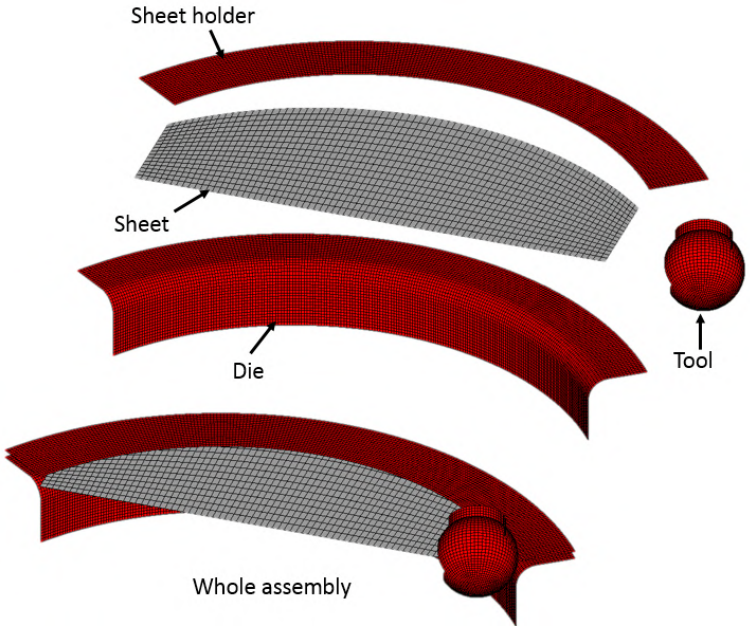

Figure 4.1. Finite element model for stretch flanging by SPIF.

forming processes. This element type has 12 degrees of freedom (DOFs) in each of its 4 nodes depicted in figure 4.3, allowing both in-plane and normal loads as well as bending. Furthermore, five integration points placed at the centre of the element were used to consider the through-thickness stress and strain gradients. A previous configuration with 3 integration points was also tested, obtaining faster simulations but less accuracy at the sheet surface. Regarding the element formulation, the different options available in the Ansys® library were analysed, with the Belytschko-Tsay element formulation providing better results. Additional information about the SHELL163 element type and its different options can be found in the Element Reference section of the Ansys® Help document (Ansys, 2018).

As seen in figure 4.1 and figure 4.2, each FE model has four components that represent the different parts involved in the flanging process. On the one hand, the forming die, sheet holder and forming tool were defined as rigid bodies with different displacement restrictions. In this regard, the forming die was fixed in 3D space, whereas the displacements of the forming tool and the sheet holder were defined by positioning vectors. On the other hand, the sheet metal was modelled using the yield criteria proposed by Barlat and Lian (1989) for anisotropic

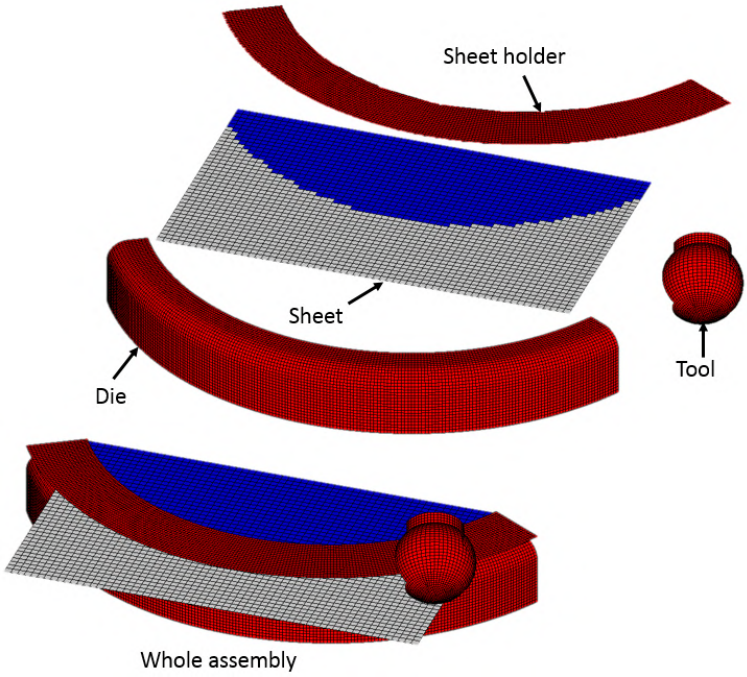

Figure 4.2. Finite element model for shrink flanging by SPIF.

materials in combination with the Swift power law and the material properties of the AA2024-T3 sheet described in chapter 3. Furthermore, as a consequence of the cyclical deformation attained in SPIF, the plasticity hardening rule was set to kinematic hardening. A more exhaustive analysis of Barlat's 89 yield criterion will be carried out in chapter 5.

The contact conditions were defined using the Ansys LS-Dyna® surface-to-surface contact model "FSTS", which is suggested for metal forming applications. This option is recommended by the Ansys LS-Dyna® manual (Ansys, 2018) for modelling bodies with large contact areas and large amounts of relative sliding. For both models, the sheet was modelled as the contact surface, whereas the forming die, forming tool and sheet holder were modelled as target surfaces. Additionally, a Coulomb friction model was assumed, setting the dynamic friction coefficient to 0.01 for the tool-sheet interface. This value was tuned by comparing numerical results with experimental results in terms of strain and force evolutions.

The different parts of the FE model were meshed using a regular mesh of quadrilateral elements with a characteristic length in the range of 0.5-1.5 mm.

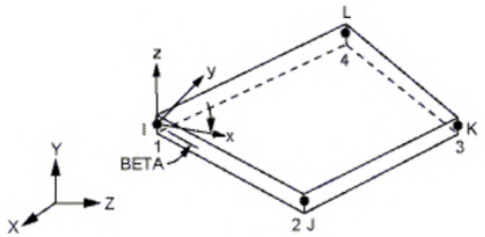

Figure 4.3. Element type Shell163 geometry. Note that X and Y are in the plane of the element.

However, the element size of the sheet was set to values below 0.5 mm to avoid the unstable results that arose depending on different factors, such as the mass scaling, hourglass control or time scaling.

It is worth mentioning that the SHELL163 element type, which is recommended in problems involving large deformations, is an element type with reduced integration. This type of element formulation produces zero-energy modes usually called hourglassing (HG), which have to be minimized, as they cause a lack of stiffness and zigzag distortions in the element mesh. These HG modes were controlled using local hourglassing controls.

The two HG controls available in Ansys LS-Dyna® consist of increasing the model stiffness locally using either viscous hourglassing control or stiffness hourglassing control. The former method, viscous hourglassing control, produces a damping effect on the velocity degrees of freedom in the direction of the hourglass modes. The damping effect is proportional to the velocities and is effective in the simulation of explosions and collisions but not in low velocity problems such as the simulation of the SPIF process. The latter method, stiffness hourglassing, increases the stiffness of the element to counteract the HG modes, whereas it allows rigid body motions and linear deformations. In this case, the stiffness of the element increases proportionally to the displacement of the nodes, which makes this HG control method suitable for low velocity problems. The intensity of the stiffness hourglassing control was specified using the hourglass coefficient, which is recommended to be 0.03 in the Ansys LS-Dyna® documentation. The ratio of the energy related to the HG effect to the total energy of the simulation was analysed to ensure a ratio below 10%, which is the maximum value recommended. This ratio was always in the range of 1%-5% in all the simulations carried out.

Another two factors considered in the design of the FE models were time scaling

and mass scaling. In the explicit method, the robustness of the simulation depends, among other factors, on the discretization of the problem in time steps smaller than a threshold value Δt. This value is defined by equation 4.1, where L_s is the characteristic length of the shell element and c is the speed of sound in the material, which is expressed in equation 4.2.

$$\Delta t = \frac{L_s}{c} \tag{4.1}$$

$$c = \sqrt{\frac{E}{\rho(1-\nu^2)}} \tag{4.2}$$

A smaller size of Δt increases the number of steps to be solved, increasing the simulation time. However, given a maximum value of Δt, it is possible to reduce the number of time steps using time scaling, which consists of artificially increasing the speed of the physical process and reducing the simulation time. In the case of the flanging FE models presented, the feed rate of the tool, which was set to 1000 mm/s in the experimental process, was multiplied by the factor MF. In this case, different values of MF ranging between x10 and x10000 led to different results. On the one hand, for MFs lower than x100, convergence problems and instabilities arose. On the other hand, for MF values higher than x2000, the problem became unstable as a consequence of the high feed rate, especially at the moment when the tool contacted the sheet.

Another method for reducing the simulation time is to increase the density of the material. Consequently, the constants c (see equation 4.2) and Δt (see equation 4.1) increase, reducing the number of time steps of the simulation. This method is known as mass scaling. In this study, the mass scaling factor was set to x10, although acceptable results were obtained in the range of x10-x100.

Time scaling and mass scaling methods should be applied under several conditions. In the case of time scaling, when the speed is increased, the dynamic effect becomes more important, and inertia forces may cause unwanted results. Special attention should be paid to the moment when two bodies make contact. Regarding mass scaling, the effect is similar, although in this case, it is the virtually increased density that causes the inertia forces to increase.

Using time scaling and mass scaling, the simulation time was reduced by one order of magnitude. For example, the simulation time for the FE model of a

concave flange with $w_0 = 63$ mm and $l_0 = 20$ mm, with approximately 5000 elements in the sheet, was reduced from 4 days to less than 10 hours.

4.2 In-plane principal strains

As presented in chapter 3, the flanges were analysed in terms of principal strains within the FLD, with the experimental principal strains obtained using the CGA system Argus®. In this regard, the strains ε_1^{arg}, ε_2^{arg} and ε_t^{arg}, which correspond to the major strain, minor strain and thickness reduction strain obtained using Argus®, are different from the global principal strains ε_1, ε_2 and ε_3 obtained from the FE software. Consequently, the principal strains obtained from the FE model were transformed to obtain the in-plane principal strains in the plane of the sheet. The process to perform this transformation will be detailed below for a single element.

First, the strain components ε_{ij} of the strain tensor $\bar{\varepsilon}$ presented in equation 4.3 were obtained from the FE software. Note that the strain tensor $\bar{\varepsilon}$ is symmetrical and can therefore be completely defined using 6 components. Figure 4.4a presents the different components of the strain tensor expressed in an orthogonal reference system that does not coincide with the reference system of the element. Then, using equation 4.4, the strain tensor is expressed in the new coordinate system $X'Y'Z'$, whose axis X' and Y' are contained in the plane of the sheet. In this equation $\bar{A}$ is the transformation matrix used to transform $\bar{\varepsilon}$ to $\bar{\varepsilon}'$, whose rows are the axes of the new coordinates system $X'Y'Z'$ expressed using the old coordinates system XYZ. The transformation matrix $\bar{A}$ can be expressed according to the Euler angles ϕ, ψ and θ as in equation 4.5, where C and S corresponds to cosine and sine respectively. The z axis of the new coordinate system $X'Y'Z'$ coincides with the direction normal to the shell element, and therefore, the axes X' and Y' are in the plane of the sheet element. As seen in figure 4.4b, the components ε'_{xx}, ε'_{yy}, ε'_{xy} and ε'_{yx} of the strain tensor $\bar{\varepsilon}'$ are also contained in the plane of the shell element.

At this point, the tensor $\bar{\varepsilon}'$ is rotated around the Z' axis (see figure 4.4c) to find a position at which its tangential strain components ε'_{xy} and ε'_{yx} are zero. After this rotation, the components ε''_{xx} and ε''_{yy} of the tensor $\bar{\varepsilon}''$ are the in-plane principal strains ε_1^{ip} and ε_2^{ip}, with $\varepsilon'_{zz} = \varepsilon_t$. In this regard, ε_1^{ip} and ε_2^{ip} are obtained from the eigenvalues of the 2x2 sub-matrix formed by ε''_{xx}, ε''_{xy}, ε''_{yx} and ε''_{yy}. The new expression of the strain tensor is given by equation 4.6.

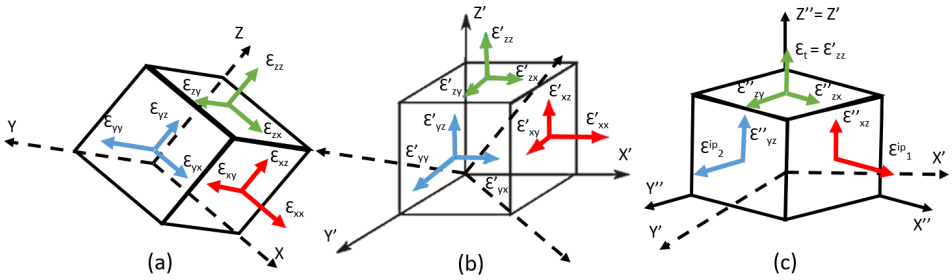

Figure 4.4. Graphical representation of the strain tensor: (a) initial arbitrary orientation, (b) z axis parallel to the element normal, and (c) orientation to obtain the in-plane principal strains.

$$\bar{\varepsilon} = \begin{bmatrix} \varepsilon_{xx} & \varepsilon_{xy} & \varepsilon_{xz} \\ \varepsilon_{xy} & \varepsilon_{yy} & \varepsilon_{yz} \\ \varepsilon_{xz} & \varepsilon_{yz} & \varepsilon_{zz} \end{bmatrix} \tag{4.3}$$

$$\bar{\varepsilon}' = \bar{A} \cdot \bar{\varepsilon} \bar{A}^T = \begin{bmatrix} \varepsilon'_{xx} & \varepsilon'_{xy} & \varepsilon'_{xz} \\ \varepsilon'_{xy} & \varepsilon'_{yy} & \varepsilon'_{yz} \\ \varepsilon'_{xz} & \varepsilon'_{yz} & \varepsilon'_{zz} \end{bmatrix} \tag{4.4}$$

$$\bar{A} = \begin{bmatrix} C(\psi)C(\phi) - S(\psi)C(\theta)S(\phi) & C(\psi)S(\phi) + S(\psi)C(\theta)C(\phi) & S(\psi)S(\theta) \\ -S(\psi)C(\phi) - C(\psi)C(\theta)S(\phi) & -S(\psi)S(\phi) + C(\psi)C(\theta)C(\phi) & C(\psi)S(\theta) \\ S(\theta)S(\phi) & S(\theta)C(\phi) & C(\theta) \end{bmatrix} \tag{4.5}$$

$$\bar{\varepsilon}'' = \begin{bmatrix} \varepsilon_1^{ip} & 0 & \varepsilon''_{xz} \\ 0 & \varepsilon_2^{ip} & \varepsilon''_{yz} \\ \varepsilon''_{xz} & \varepsilon''_{yz} & \varepsilon_t \end{bmatrix} \tag{4.6}$$

After the process described above, the components ε_1^{ip}, ε_2^{ip} and ε_t of the strain tensor are equivalent to the major strain, minor strain and negative thickness reduction strain obtained from the CGA software, i.e., ε_1^{arg}, ε_2^{arg} and $-\varepsilon_t^{arg}$. This transformation process described for a single element was applied to every element of the sheet, obtaining the set of strain data that were comparable to the experimental results.

Chapter 5

Analytical framework

This chapter presents the stress triaxiality theoretical framework used in the prediction of failure for the flanging process by SPIF. In section 5.1, three plasticity yield criteria widely used in finite element simulations are described. In section 5.2, the FFL for an AA2024-T3 sheet is obtained using these yield criteria, performing a numerical-experimental validation of the FFL corresponding to Barlat's 89 yield criterion.

5.1 Plasticity criteria: anisotropy

In a general plastic stress state, the material behaviour is defined using three elements: (i) a yield criterion that defines the value of the stress components in the transition from the elastic to plastic state, (ii) a flow rule associated with this criterion that relates the stress components to the strains and (iii) a description of the stress evolution at yielding, known as the hardening rule. In FE modelling, these elements are considered in the definition of the material behaviour and determine the response of the model.

As described in chapter 4, the material flow rule used in the FE models follows the Swift power law, with the coefficients adjusted with the stress-strain curve of the AA2024-T3 sheet. With respect to the hardening rule, two options available are kinematic and isotropic. The former, kinematic hardening, establishes that the yield curve is displaced in the stress space without changing its shape. The latter, isotropic hardening, leads to variation in the size of the yield curve without displacement. In this regard, both hardening rules were tested, obtaining

better results when using the selected option of kinematic hardening. Concerning the yield criterion, three were considered: the von Mises plasticity yield criterion for anisotropic materials, the Hill 48 anisotropic yield criterion and Barlat's 89 anisotropic yield criterion. In this regard, the formulations of the yield criteria were simplified assuming plane stress ($\sigma_3 = 0$). Furthermore, the anisotropy was specified using the Lankford coefficients, whose values can be found in chapter 3.

5.1.1 von Mises yield criterion

The plasticity criterion proposed by Mises (1913) is a yield criterion based on the distortion energy. In this regard, it establishes that yielding occurs when the elastic energy of distortion reaches a critical value. This assumption makes it possible to experimentally obtain a critical stress value σ_0 in uniaxial tension and use it as a reference for more complex stress states. Assuming plane strain, the equation of the von Mises anisotropy yield criterion can be expressed using equation 5.1. This equation represents an ellipse in the plane of principal stresses σ_1 and σ_2, as depicted in figure 5.1.

$$(\sigma_1 - \sigma_2)^2 + \sigma_1^2 + \sigma_2^2 = 2\sigma_0^2 \tag{5.1}$$

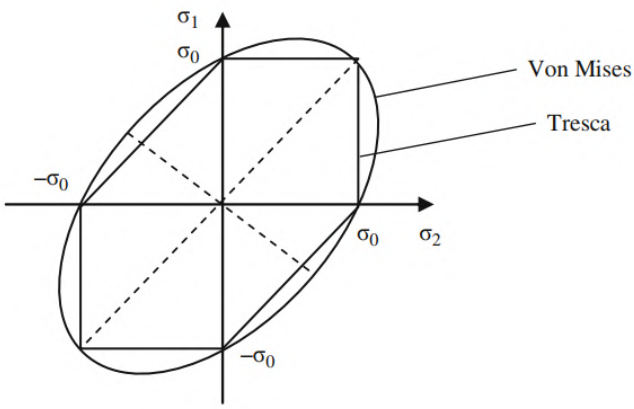

Figure 5.1. Graphical representation of the von Mises yield criterion in the plane of principal stresses.

Although von Mises is widely accepted as one of the classic plasticity criteria,

it is defined only for isotropic materials. Therefore, it cannot represent the anisotropic behaviour of sheet metals. As can be observed in figure 5.1, the yield surface in the stress plane is symmetric with respect to its axes. Consequently, σ_1 and σ_2 produce equal results. The von Mises criterion was included in this study as an example of an isotropic criterion and for comparison with anisotropic yield criteria.

5.1.2 Hill 1948 yield criterion

Hill 1948 (Hill, 1948) is one of the classical yield criteria. It was proposed as a generalization of the von Mises criterion for anisotropic materials (Mises, 1928) applied to orthotropic materials. As a von Mises anisotropic criterion, the Hill criterion is based on a quadratic function. However, the Hill criterion assumes orthotropy and includes only six coefficients. The general expression of the quadratic Hill criterion is presented in equation 5.2, where F, G, H, L and M are six constants, which depend on the anisotropy coefficients r_0, r_{90} and r_{45}.

$$\begin{aligned} 2f(\sigma) \equiv F(\sigma_{22}-\sigma_{33})^2 \ + \ G(\sigma_{33}-\sigma_{11})^2 \ + \ H(\sigma_{11}-\sigma_{22})^2 \\ + \ 2L\sigma_{23}^2 \ + \ 2M\sigma_{31}^2 \ + \ 2N\sigma_{12}^2 = 1 \end{aligned} \tag{5.2}$$

Particularizing for plane stress conditions ($\sigma_3 3 = \sigma_{31} = \sigma_{23} = 0$), using the Lankford anisotropy coefficients, this general expression can be written in terms of the uniaxial yield stress in the rolling direction σ_0, as expressed in equation 5.3, where σ_1 and σ_2 are the stress components along the principal axes oriented 0° and 90° with respect to the rolling direction. This equation was used in figure 5.2 to obtain a number of yield curves for different values of anisotropy. In these curves, the yield stress σ_0 was normalized to 1. Furthermore, the yield curve corresponding to the von Mises isotropic yield criterion was also included for comparison with the curves obtained with isotropic yield criteria. In this case, it must be mentioned that when the anisotropy coefficients r are set to 1, the Hill yield criterion becomes the von Mises isotropic yield criterion. Regarding the effect of anisotropy, the influence of the different Lankford coefficients is depicted in figure 5.2a-c. Additionally, figure 5.2d shows the yield curve obtained using the Lankford coefficients for the AA2024-T3 sheet.

$$\sigma_1^2 \; - \; \frac{2r_0}{1+r_0}\sigma_1\sigma_2 \; + \; \frac{r_0(1+r_90)}{r_90(1+r_0)}\sigma_2^2 \; = \; \sigma_0^2 \tag{5.3}$$

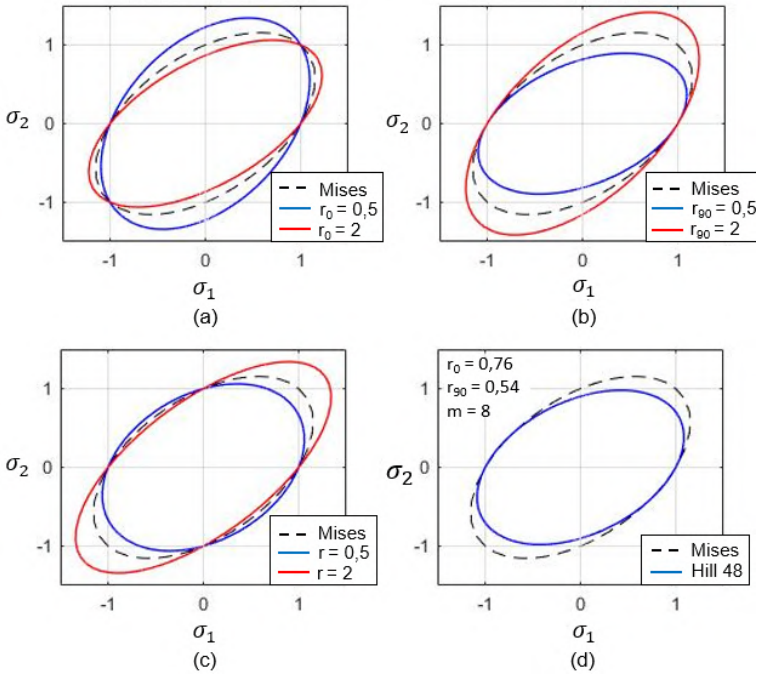

Figure 5.2. Yield curves for the Hill 1948 yield criterion: (a) influence of r_0, (b) influence of r_{90}, (c) influence of the normal anisotropy coefficient r and (d) yield curve for the AA2024-T3 sheet.

As shown in figure 5.2d, for $r < 1$, the yield curve corresponding to the Hill criterion is inside of the von Mises ellipse in the first quadrant (+,+), yielding lower stress levels than in the isotropic case. In contrast, for $r > 1$, the curve corresponding to the Hill criterion is outside the von Mises curve in the first quadrant. Considering that the Lankford coefficients for the AA2024-T3 sheet are less than 1, the predicted biaxial stress σ_b for this material is smaller than the uniaxial stress σ_0. In this regard, Woodthrope and Pearce (1970) and Pearce (1968) showed that some materials, especially aluminium alloys, present $\sigma_b > \sigma_0$

for $r < 1$. They showed that this anomalous behaviour cannot be predicted adequately using the Hill criterion. For this reason, the yield criterion proposed by Barlat in 1989 was used in the FE models.

5.1.3 Barlat 1989 yield criterion

The yield criterion proposed by Barlat and Lian (1989) was developed from a previous yield criterion of Barlat and Richmond (1987) formulated for isotropic materials with the purpose of describing the behaviour of sheet metals with planar anisotropy. As in the case of the Hill yield criterion mentioned above, its formulation is based on the microstructural plastic potential and has been shown to be useful in the prediction of the yield locus for aluminium alloys. This criterion assumes plane stress and is frequently used in numerical simulations of sheet metal forming processes, especially for those with planar anisotropy. One of its main advantages is the lower complexity compared with other criteria. In this regard, this criterion contains only four mechanical parameters (a, c, h and p) that can be easily obtained except for p, which has to be identified numerically.

Equation 5.4 presents a generalization of Barlat's 89 yield criterion in a general stress state for materials that present planar anisotropy. The exponent m is related to the crystallographic structure of the material, which, following the recommendations of Logan and Hosford (1980), has to be 6 for BCC and 8 for FCC materials. $k1$ and $k2$, which are invariants of the stress tensor, are obtained from the equations expressed in 5.5. The values of a, c and h can be obtained by introducing the anisotropy coefficients r_0 and r_{90} into equation 5.6. The parameter p is obtained numerically using the expressions that relate a, c, h and p with the yield stresses obtained in different shear and uniaxial tests. In this study, p was not obtained because the FE software does so internally. More information about how to obtain this value can be found in the publication of Banabic (2010).

$$f(\sigma) \equiv a|k_1 + k_2|^m + a|k_1 - k_2|^m + c|2k_2|^m = 2\bar{\sigma}^m \tag{5.4}$$

$$k_1 = \frac{\sigma_{11} + h\sigma_{22}}{2}; \qquad k_2 = \sqrt{\frac{\sigma_{11} - h\sigma_{22}}{2} + p^2\sigma_{12}^2} \tag{5.5}$$

$$a = 2 - 2\sqrt{\frac{r_0 r_{90}}{(1 + r_0)(1 + r_{90})}}; \qquad c = 2 - a; \qquad h = \sqrt{\frac{r_0(1 + r_{90})}{(1 + r_0)r_{90}}} \tag{5.6}$$

Figure 5.3 shows different yield curves obtained using the expression of Barlat's 89 yield criterion presented by equations 5.4, 5.5 and 5.6. The value of p was not considered in this analysis because the curves are presented for a principal stress state and, therefore, $\sigma_{12} = 0$. As depicted in figure 5.3b-d, the influence of the anisotropy coefficients on the yield curve is similar to the effect observed for the Hill 1948 yield criterion (figure 5.2). Regarding the effect of r_{med} in the first quadrant (figure 5.3d), values of r_{med} less than 1 displace Barlat's 89 yield curve to inside of the von Mises yield curve, and values of r_{med} higher than 1 displace the curve to outside the von Mises yield curve only in the biaxial region. With respect to the effect of m (5.3d), for high values of m, the yield curve acquires a polygonal shape that is reminiscent of the yield curve of the classical Tresca (1964) yield criterion shown in figure 5.1.

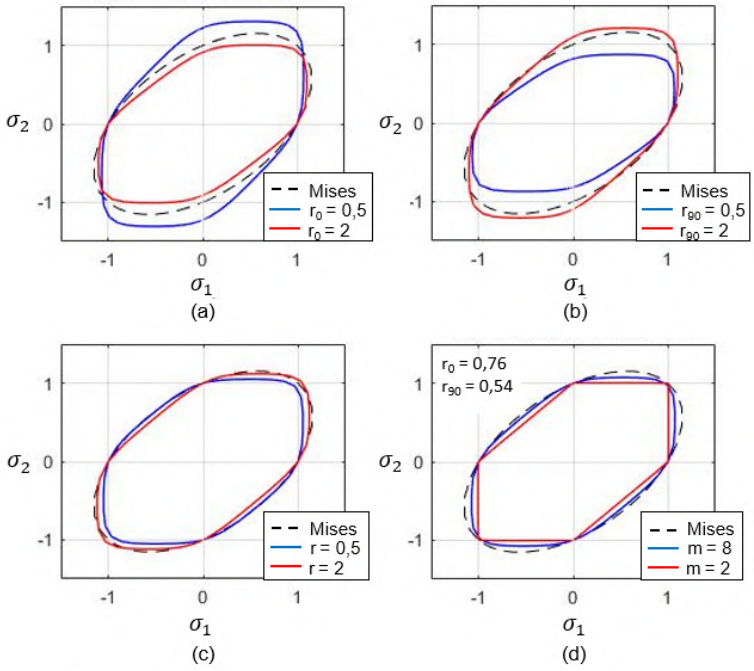

Figure 5.3. Yield curves obtained using Barlat's 1989 yield criterion: (a) influence of r_0, (b) influence of r_{90}, (c) influence of normal anisotropy coefficient r and (d) influence of Barlat exponent m

To determine the differences between the Barlat and Hill yield curves, both are presented in figure 5.4 together with the von Mises criterion yield curve. In this figure, the two anisotropic criteria predict yield curves inside the von Mises yield curve. As has been revealed, this is an effect caused by Lankford coefficients less than 1. However, Barlat's 89 prediction for the biaxial yield stress is closer to the von Mises yield curve than to the Hill 48 yield curve.

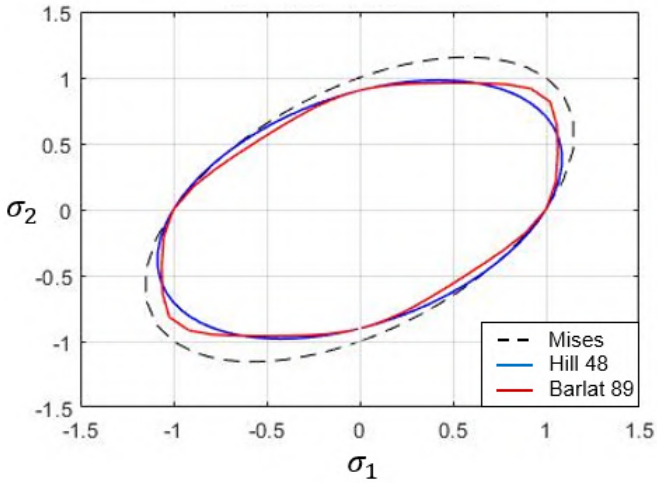

Figure 5.4. Superposition of yield curves obtained using the Barlat 1989, Hill 1948 and von Mises isotropic yield criteria.

In conclusion, this section has shown differences between the two anisotropic yield criteria analysed (Hill 1948 and Barlat 1989). According to the yield curves obtained for the AA2024-T3 sheet depicted in figure 5.4, the predictions of yield curves using the Barlat 89 and Hill 48 yield criteria are different, especially in the biaxial region. In this regard, many studies have shown higher accuracy of Barlat's 89 yield criterion for aluminium alloys. (Woodthrope and Pearce (1970) and Pearce (1968)) showed that the Barlat 1989 yield criterion is better than the Hill 1948 yield criterion in reproducing the behaviour of aluminium, specifically due to the anomalous behaviour of aluminium alloys (see section 5.1.2). Furthermore, Lege *et al.* (1964) showed the effectiveness of the Barlat 1989 yield criterion for FCC sheet metals. Based on these studies, the use of the Barlat 1989 yield criterion instead of the Hill 1948 yield criterion seems to be more accurate in FE modelling.

5.2 Stress triaxiality

This section presents a triaxiality approach to fracture prediction in SPIF based on the transformation of the formability limits from the principal strain space to the average stress triaxiality vs. equivalent strain space.

As suggested by Martins *et al.* (2014), fracture in SPIF usually occurs in mode I of fracture mechanics when a corresponding damage function D reaches a critical value D_{crit}. In this regard, Atkins (1996) proposed the damage function expressed in equation 5.7 based on the level of accumulated stress triaxiality, which was derived from the void-growth fracture criterion of McClintock (1968).

$$D = \int_0^{\bar{\varepsilon}} \frac{\sigma_m}{\bar{\sigma}} \, d\bar{\varepsilon} = \bar{\eta}\bar{\varepsilon} \tag{5.7}$$

In addition, Bao and Wierzbicki (2004) and later Wierzbicki *et al.* (2005) represented the different stress-strain states of a forming process in terms of the stress triaxiality ratio and the equivalent strain. Mirnia and Shamsari (2017) proposed a methodology for the prediction of failure using the average stress triaxiality, valid for both proportional and non-proportional loading paths, which is the case in SPIF. More recently, Martínez-Donaire *et al.* (2019) analysed the loading paths attained in hole flanging by SPIF, suggesting that the lower triaxiality levels attained in SPIF explained the high levels of principal strains at failure. In this regard, they obtained the expressions of the equivalent strain and the average stress triaxiality corresponding to the Hill 48 yield criterion and represented the FLD and the FFL of the material in the triaxiality space. Based on this work, Magrinho *et al.* (2019) proposed an analytical transformation from the stress space to the stress triaxiality space using the Hosford yield criterion for proportional loading.

Based on these previous studies, the expressions of the average stress triaxiality $\bar{\eta}$ and the equivalent strain $\bar{\varepsilon}$ are obtained in subsection 5.2.1 using the three yield criteria: the von Mises isotropic yield criterion, Hill 48 yield criterion and Barlat 89 yield criterion. Afterwards, in subsection 5.2.2, these expressions are used to assess, experimentally and using FE, the FFL of an AA2024-T3 sheet in the stress triaxiality space.

5.2.1 Triaxiality equations

The transformation of the experimental loading paths and the corresponding forming limits from the principal strain space to the triaxiality space requires evaluating the stress triaxiality ratio η and the effective strain $\bar{\varepsilon}$. The expressions of η and $\bar{\varepsilon}$ were obtained in terms of principal stresses σ_1 and σ_2, with the tangential component of the stress tensor $\tau_{12} = 0$ and assuming plane stress conditions ($\sigma_3 = 0$).

5.2.1.1 von Mises

The expression of the stress triaxiality ratio η and the equivalent strain $\bar{\varepsilon}$ corresponding to the von Mises criterion were obtained from the general expression of the von Mises isotropic yield criterion for plane stress, which is expressed as follows:

$$2f(\sigma_{ij}) \equiv (\sigma_1 - \sigma_2)^2 + \sigma_1^2 + \sigma_2^2 = 2\bar{\sigma}^2 \tag{5.8}$$

Considering the general expression of the flow rule expressed in equation 5.9,

$$d\bar{\varepsilon}_{ij} = d\lambda \frac{\partial f(\sigma_{ij})}{\partial \sigma_{ij}} \tag{5.9}$$

where $d\lambda > 0$ is the instantaneous hardening parameter related to the material strain-stress curve and σ_{ij} is taken as the von Mises isotropic plasticity criterion, the expressions of the strain increments $d\varepsilon_1$ and $d\varepsilon_2$ (equation 5.10) are obtained:

$$\begin{aligned} d\varepsilon_1 &= 4\sigma_1 - 2\sigma_2 \\ d\varepsilon_2 &= 4\sigma_2 - 2\sigma_1 \end{aligned} \tag{5.10}$$

Consequently, the expression of the strain ratio β can be written using equation 5.10 as follows:

$$\beta = \frac{d\varepsilon_2}{d\varepsilon_1} = \frac{4\sigma_2 - 2\sigma_1}{4\sigma_1 - 2\sigma_2} = \frac{2\alpha - 1}{2 - \alpha} \tag{5.11}$$

where α is the stress ratio (equation 5.12).

$$\alpha = \frac{\sigma_2}{\sigma_1} \tag{5.12}$$

Then, considering the incremental plastic work per unit of volume expressed in equation 5.13,

$$dw_p = (\sigma_1 d\varepsilon_1 + \sigma_2 d\varepsilon_2) = \bar{\sigma} d\bar{\varepsilon} \tag{5.13}$$

and the strain ratio expressed in equation 5.11 and assuming the equivalent stress obtained from equation 5.8, the effective strain increment $d\bar{\varepsilon}$ becomes

$$d\bar{\varepsilon} = \frac{(1 + \alpha\beta) d\varepsilon_1}{\sqrt{\alpha^2 - \alpha + 1}} \tag{5.14}$$

which is also valid in terms of absolute variables $d\bar{\varepsilon}_{eq} = f(\varepsilon_1)$ under the assumption of proportional loading.

Finally, expressing the mean stress σ_m under plane stress conditions ($\sigma_3 = 0$) as

$$\sigma_m = \frac{\sigma_1 + \sigma_2 + \sigma_3}{3} = \frac{\sigma_1 + \sigma_2}{3} = \frac{1 + \alpha}{3}\sigma_1 \tag{5.15}$$

it is possible to use equation 5.8 and equation 5.15 to define the stress triaxiality ratio η as follows:

$$\eta = \frac{\sigma_m}{\bar{\sigma}} = \frac{(1 + \alpha)}{3\sqrt{\alpha^2 - \alpha + 1}} \tag{5.16}$$

Equations 5.14 and 5.16 can be used to transform the proportional strain loading paths and the forming limits from the principal strain space to the triaxiality space using the von Mises isotropic yield criterion.

5.2.1.2 Hill 1948

The expressions of the stress triaxiality ratio η and the equivalent strain $\bar{\varepsilon}$ for the Hill 48 yield criterion were obtained following the same procedure as for the von Mises yield criterion (section 5.2.1.1). These expressions were obtained by Martínez-Donaire *et al.* (2019) under the assumption of normal anisotropy. However, the expressions presented in this section will be formulated assuming planar anisotropy, which considers the Lankford coefficients r_0 and r_{90} instead of the normal anisotropy coefficient r. In this regard, the general expression of the Hill 48 yield criterion for plane stress, expressed in terms of principal stress components σ_1 and σ_2, is

$$2f(\sigma_{ij}) \equiv (G+H)\sigma_1^2 - 2H\sigma_1\sigma_2 + (H+F)\sigma_2^2 = \bar{\sigma}^2 \tag{5.17}$$

where the coefficients F, G and H are functions of the Lankford coefficients r_0 and r_{90} through the relations

$$F = \frac{r_0}{(1+r_0)r_{90}}; \qquad G = \frac{1}{(1+r_0)}; \qquad H = 1 - \frac{1}{(1+r_0)} \tag{5.18}$$

The expressions of $d\varepsilon_1$ and $d\varepsilon_2$ are obtained by applying the general flow rule (equation 5.9),

$$\begin{aligned} d\varepsilon_1 &= (G+H)\sigma_1 - H\sigma_2 \\ d\varepsilon_2 &= -H\sigma_1 + (H+F)\sigma_2 \end{aligned} \tag{5.19}$$

Consequently, using equation 5.12, the strain ratio β can be expressed as a function of the stress ratio α as follows:

$$\beta = \frac{d\varepsilon_2}{d\varepsilon_1} = \frac{-H\sigma_1 + (H+F)\sigma_2}{(G+H)\sigma_1 - H\sigma_2} = \frac{(H+F)\alpha - H}{G + H - H\alpha} \tag{5.20}$$

Then, considering the expression of the incremental plastic work per unit of volume (equation 5.13) and the strain ratio expressed in equation 5.11 and assum-

ing the equivalent stress obtained for the Hill 48 yield criterion (equation 5.17), the effective strain increment $d\bar{\varepsilon}$ is expressed as follows:

$$d\bar{\varepsilon} = \frac{(1+\alpha\beta)d\varepsilon_1}{\sqrt{G+H-2H\alpha+(H+F)\alpha^2}} \tag{5.21}$$

Finally, from the expression of the mean stress under plane stress conditions (equation 5.15) and the general expression of the Hill 48 yield criterion for plane stress conditions (5.17), it is possible to define the stress triaxiality ratio η as follows:

$$\eta = \frac{\sigma_m}{\bar{\sigma}} = \frac{1+\alpha}{3\sqrt{G+H-2H\alpha+(H+F)\alpha^2}} \tag{5.22}$$

Equations 5.21 and 5.22 can be used to transform the proportional strain loading paths and the forming limits from the principal strain space to the triaxiality space using the Hill 48 yield criterion. Note that for $r_0 = 0$ and $r_{90} = 0$, i.e., assuming isotropy, equation 5.21 and equation 5.22 become the expressions of the strain increment (equation 5.14) and stress triaxiality ratio (equation 5.16), respectively, that correspond to the von Mises isotropic yield criterion.

5.2.1.3 Barlat 1989

The general expression of the Barlat 1989 yield function for planar anisotropy and plane stress conditions is presented in equation 5.23, where k_1 and k_2 (equation 5.24) can be written as functions of the principal stresses σ_1 and σ_2 or using the expression of the stress ratio presented in equation 5.12.

$$f(\sigma_{ij}) \equiv a|k_1+k_2|^m + a|k_1-k_2|^m + c|2k_2|^m = 2\bar{\sigma}^m \tag{5.23}$$

$$k_1 = \frac{\sigma_1+h\sigma_2}{2} = \frac{1+h\alpha}{2}\sigma_1; \qquad k_2 = \sqrt{\left(\frac{\sigma_1-h\sigma_2}{2}\right)^2} = \sqrt{\left(\frac{1-h\alpha}{2}\right)^2}\,\sigma_1 \tag{5.24}$$

The parameters a, c and h, given by equation 5.25, are functions of the aniso-

tropy coefficients r_0 and r_{90}, and the exponent m depends on the crystallographic structure. In this case, m was set to 8, corresponding to FCC structures.

$$a = 2 - 2\sqrt{\frac{r_0 r_{90}}{(1+r_0)(1+r_{90})}}; \qquad c = 2 - a; \qquad h = \sqrt{\frac{r_0(1+r_{90})}{(1+r_0)r_{90}}} \tag{5.25}$$

Considering the general flow rule expression (equation 5.9), the strain increments $d\varepsilon_1$ and $d\varepsilon_2$ can be defined as follows:

$$\begin{aligned} d\varepsilon_1 &= am|k_1+k_2|^{m-2}(k_1+k_2) + cm|2k_2|^{m-2}(2k_2) \\ d\varepsilon_2 &= amh|k_1-k_2|^{m-2}(k_1-k_2) - cmh|2k_2|^{m-2}(2k_2) \end{aligned} \tag{5.26}$$

Consequently, the stress ratio β can be written as a function of the stress ratio α (equation 5.12) as shown in equation 5.27.

$$\beta = \frac{d\varepsilon_2}{d\varepsilon_1} = \frac{a|k_1+k_2|^{m-2}(k_1+k_2) + c|2k_2|^{m-2}(2k_2)}{ah|k_1-k_2|^{m-2}(k_1-k_2) - ch|2k_2|^{m-2}(2k_2)} \tag{5.27}$$

Substituting into equation 5.27 the expressions of k_1 and k_2 presented in equation 5.24, σ_1 is cancelled and β is defined as a function of the stress ratio α:

$$\beta = \frac{ah\left|\frac{1+h\alpha}{2} - \sqrt{\left(\frac{1-h\alpha}{2}\right)^2}\right|^{m-2}\left(\frac{1+h\alpha}{2} - \sqrt{\left(\frac{1-h\alpha}{2}\right)^2}\right) - ch\left|2\sqrt{\left(\frac{1-h\alpha}{2}\right)^2}\right|^{m-2}\left(2\sqrt{\left(\frac{1-h\alpha}{2}\right)^2}\right)}{a\left|\frac{1+h\alpha}{2} + \sqrt{\left(\frac{1-h\alpha}{2}\right)^2}\right|^{m-2}\left(\frac{1+h\alpha}{2} + \sqrt{\left(\frac{1-h\alpha}{2}\right)^2}\right) + c\left|2\sqrt{\left(\frac{1-h\alpha}{2}\right)^2}\right|^{m-2}\left(2\sqrt{\left(\frac{1-h\alpha}{2}\right)^2}\right)} \tag{5.28}$$

Then, considering the expression of the incremental plastic work per unit of volume (equation 5.13) and the strain ratio β (equation 5.11) and assuming the equivalent stress obtained for the Barlat 89 yield criterion (equation 5.23), the effective strain increment $d\bar{\varepsilon}$ is expressed as follows:

$$d\bar{\varepsilon} = \frac{(\sigma_1 d\varepsilon_1 + \sigma_2 d\varepsilon_2)}{\bar{\sigma}} = \frac{(1+\alpha\beta)\sigma_1 d\varepsilon_1}{\bar{\sigma}} \tag{5.29}$$

Using the expression of equivalent stress $\bar{\sigma}$ for the Barlat 89 yield function obtained from equation 5.23 and substituting k_1 and k_2 from equation 5.24 into equation 5.29, σ_1 can be cancelled, obtaining the effective strain increment as a function of α, β and the strain increment $d\varepsilon_1$ as follows:

$$d\bar{\varepsilon} = \frac{(1+\alpha\beta)d\varepsilon_1}{\left(\frac{a}{2}\left|\frac{1+h\alpha}{2}+\sqrt{\left(\frac{1-h\alpha}{2}\right)^2}\right|^m + \frac{a}{2}\left|\frac{1+h\alpha}{2}-\sqrt{\left(\frac{1-h\alpha}{2}\right)^2}\right|^m + \frac{c}{2}\left|\sqrt{(1-h\alpha)^2}\right|^m\right)^{\frac{1}{m}}} \tag{5.30}$$

Equation 5.30 is also valid in terms of absolute variables $\bar{\varepsilon}_{eq} = f(\varepsilon_1)$ under the assumption of proportional loading.

Finally, from the mean stress σ_m (equation 5.15) and the equivalent stress $\bar{\sigma}$ for Barlat 89 (equation 5.23), the stress triaxiality ratio η is defined as follows:

$$\eta = \frac{\sigma_m}{\bar{\sigma}} = \frac{\frac{(1+\alpha)}{3}}{\left(\frac{a}{2}\left|\frac{1+h\alpha}{2}+\sqrt{\left(\frac{1-h\alpha}{2}\right)^2}\right|^m + \frac{a}{2}\left|\frac{1+h\alpha}{2}-\sqrt{\left(\frac{1-h\alpha}{2}\right)^2}\right|^m + \frac{c}{2}\left|\sqrt{(1-h\alpha)^2}\right|^m\right)^{\frac{1}{m}}} \tag{5.31}$$

Using the expression of the stress triaxiality ratio expressed in equation 5.31, the expression of the average stress triaxiality defined in equation 5.32 is obtained. However, obtaining the analytical expression of equation 5.32) has not been necessary. On the one hand, the strain evolutions of the Nakazima tests used to obtain the FFL are proportional, with the stress triaxiality ratio defined by a constant. On the other hand, the average stress triaxiality corresponding to the flanging simulations, which have non-proportional strain evolutions, is obtained numerically.

$$\bar{\eta} = \frac{1}{\varepsilon_{eq}} \int_0^{\bar{\varepsilon}} \frac{\sigma_m}{\sigma_{eq}}\, d\varepsilon_{eq} \tag{5.32}$$

5.2.2 Forming limit within the triaxiality space

Assessment of the FFL curves presented in the stress triaxiality vs. equivalent strain space was carried out for the three yield criteria presented in section 5.2.1. Additionally, the FFL corresponding to the Barlat 89 criterion, which is the yield criterion used in the FE models, was obtained using FE simulations and the experimental fracture strains of the Nakazima test presented in section 3.1.3.

5.2.2.1 Obtaining the FFL curves

Assessment of the FFL curves in the triaxiality space was performed through the transformation of the fracture points from the principal strain space to the average stress triaxiality vs. equivalent strain ($\bar{\eta}$-$\bar{\varepsilon}$) space. To perform the transformation, the expressions of $\bar{\eta}$ and $\bar{\varepsilon}$ for the three yield criteria presented in section 5.2.1 were evaluated using different fracture strains. For the two anisotropic criteria, Hill 48 and Barlat 89, the Lankford coefficients corresponded to the AA2024-T3 sheet ($r_0 = 0.76$ and $r_{90} = 0.54$). The procedure to obtain the FFL curves is homologous for the three yield criteria and will therefore be described exhaustively for the Barlat 89 yield criterion and extrapolated for the other two criteria.

Table 5.1 contains the principal strains $\bar{\varepsilon}_1$ and $\bar{\varepsilon}_2$, the strain ratio β and the stress ratio α of the points selected to represent the FFL in the triaxiality space. These points were classified as either experimental (E) or theoretical (T). On the one hand, the experimental points represent the fracture strains achieved in the experimental Nakazima tests described in section 3.1.3. These points were obtained by averaging the fracture strains obtained for each strain path presented in figure 5.5a. In addition, the experimental points were used to obtain the FFL in the principal strain space. On the other hand, the theoretical points were obtained from the intersection between the FFL and the theoretical strain paths corresponding to uniaxial tension ($\alpha = 0$), plane strain ($\beta = 0$) and equi-biaxial strain ($\beta = 1$). These points are represented in figure 5.5a by white squares. It should be mentioned that $\beta = -0.432$ is the strain ratio for pure tension ($\alpha = 0$) of AA2024-T3 obtained using the Barlat 89 yield criterion from equation 5.27. In the case of the FFL curves for the Hill 48 yield criterion and von Mises isotropic yield criterion, equations 5.20 and 5.11 were used, respectively.

Description	β	α	ε_1	ε_2
Uniaxial (T)	-0.432	0	0.468	-0.202
Uniaxial (E)	-0.314	0.062	0.383	-0.120
Plane-strain (E)	-0.089	0.232	0.284	-0.025
Plane-strain (T)	0	0.448	0.260	0
Biaxial 1 (E)	0.092	0.641	0.241	0.022
Biaxial 2 (E)	0.383	0.780	0.237	0.091
Equi-biaxial (E)	0.900	0.876	0.258	0.232
Equi-biaxial (T)	1	0.889	0.260	0.260

Table 5.1. Values of α, β and major strain ε_1 for the points selected to represent the FFL curve in the $\bar{\eta}$-$\bar{\varepsilon}$ diagram. (T) theoretical, (E) experimental.

Using the values of β and ε_1 presented in table 5.1, the expressions of $\bar{\eta}$ (equation 5.31) and $\bar{\varepsilon}$ (equation 5.30) for the Barlat 89 yield criterion were evaluated, obtaining the corresponding FFL in the stress triaxiality space depicted in figure 5.5b. In this figure, the blue line corresponds to the FFL for the Barlat yield criterion, and the theoretical and experimental points are represented using blue filled squares and filled circles, respectively, according to the criteria adopted in figure 5.5a. As mentioned, the strain paths were considered proportional, and consequently, (i) the major strain increment $d\varepsilon_1$ and the major strain ε_1 coincide in equation 5.31), and (ii) the expressions for the average stress triaxiality 5.32 and the triaxiality ratio 5.31 are equivalent. In the second case, this causes the evolution of the average stress triaxiality to be represented by a straight vertical line in the diagram depicted in figure 5.5b.

In addition, the FFL curves for the von Mises anisotropy yield criterion and the Hill 48 yield criterion are presented in figure 5.5b. The FFL curves obtained using the different yield criteria are sensibly different. In this regard, the FFL of the von Mises yield criterion is similar to the FFL for Barlat's 89 yield criterion in the biaxial region ($\bar{\eta} \approx 0.65$) and different from the FFL for the Hill 48 yield criterion. In contrast, the FFL curves corresponding to the Barlat 89 and Hill 48 yield criteria are similar for $\bar{\eta} \leq 0.55$ but different from the FFL obtained for the von Mises criterion in the same range of $\bar{\eta}$. Consequently, the predictions of fractures in the triaxiality space using different yield criteria are very different.

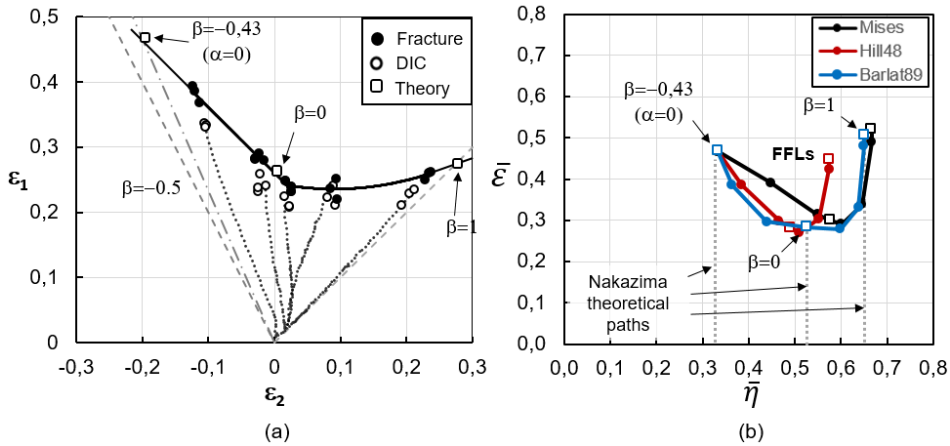

Figure 5.5. (a) FFL obtained by Nakazima tests and (b) FFL in the stress triaxiality space using different yield criteria.

Regarding anisotropy, the effect of the Lankford coefficients on the FFL curves was analysed. In this regard, figures 5.6 and 5.7 present the FFL curves for the Barlat 89 yield criterion for different values of r_0 and r_{90}, respectively. In general, a variation in the Lankford coefficients displaces the FFL curves in the triaxiality space. Concretely, changes in r_0 produce a displacement of the left part of the curves (see figure 5.6), and variations in r_{90} displace the right part of the FFL curves (see figure 5.7).

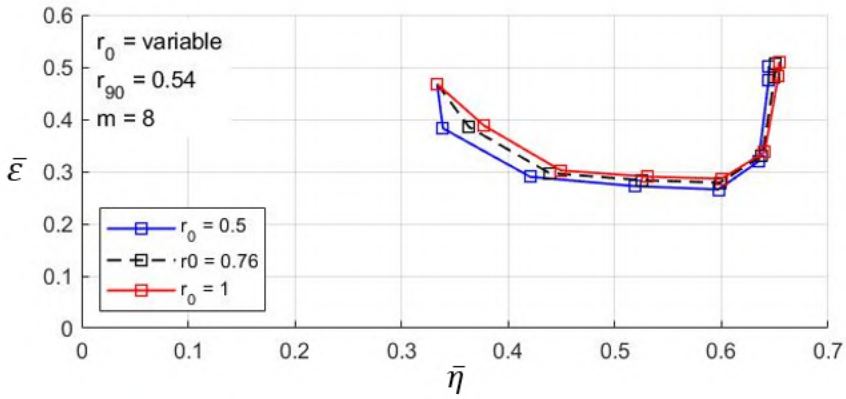

Figure 5.6. Effect of Lankford coefficient r_0 on the FFL curves in the triaxiality space obtained using Barlat's 89 yield criterion.

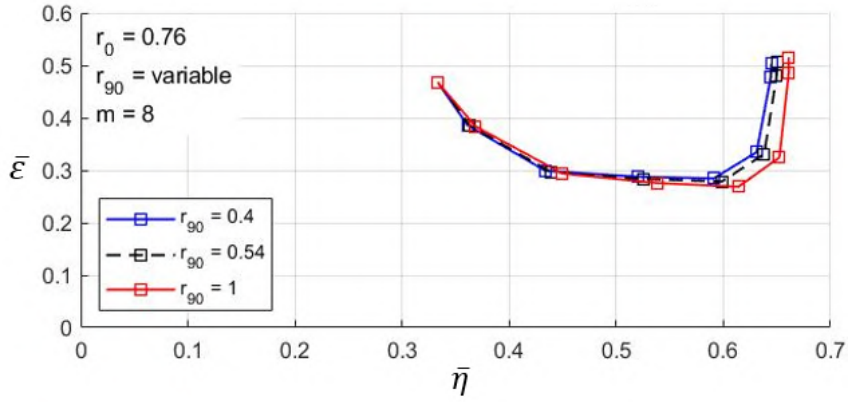

Figure 5.7. Effect of Lankford coefficient r_{90} on the FFL curves in the triaxiality space obtained using Barlat's 89 yield criterion.

Finally, the effect of different values of the Barlat exponent m was analysed. The blue line in figure 5.8 corresponds to $m = 2$, which coincides with the Hill criterion. The FFL presented in red is a hypothetical case corresponding to $m = 20$, which shows the effect of increasing m well above 8. In this regard, it can be seen that the FFL curves are sensitive to the value of the Barlat exponent m, obtaining different values of triaxiality ratio η and equivalent strain $\bar{\varepsilon}$ for the same fracture points.

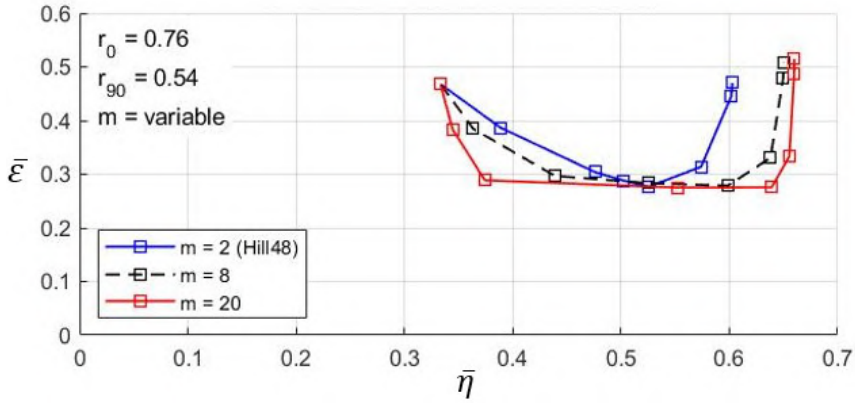

Figure 5.8. Effect of Barlat exponent m on the FFL curves in the triaxiality space obtained using Barlat's 89 yield criterion.

5.2.2.2 Numerical assessment of the Barlat FFL

This section analyses the evolutions of numerical Nakazima tests in the stress triaxiality space using the Barlat 89 yield criterion. These evolutions are then compared to the FFL obtained analytically in section 5.2.2.1 to assess the accuracy of the triaxiality results obtained in section 6.1.4 for the simulations of flanging by SPIF.

For the FE model of the Nakazima tests, the same parameters considered for the simulations of flanging forming by SPIF were used. Specifically, the material properties, meshing parameters and hourglass control are presented in section 4. The use of these parameters ensures consistency with the triaxiality results obtained in section 6.1.4. Furthermore, to obtain different paths in the triaxiality space, three different specimen geometries for the Nakazima tests were considered: uniaxial tension, plane strain and equi-biaxial strain.

Figure 5.9 depicts the evolutions of the numerical Nakazima tests in the stress triaxiality space. On the one hand, the grey curves represent the evolution of the triaxiality ratio η during the tests. Under proportional loading, η is a constant, and therefore, its evolution is a vertical line, as depicted for the equi-biaxial test ($\eta \approx 0.65$). However, the evolutions of η for uniaxial tension ($\eta \approx 0.36$) and plane strain ($\eta \approx 0.43$) present oscillations in the initial stages of the test. This occurs due to the adjustment between the specimen and the Nakazima spherical punch. On the other hand, the dotted black curves represent the evolution of the average stress triaxiality $\bar{\eta}$. The evolution of $\bar{\eta}$ is obtained from equation 5.32 and coincides with η for proportional loading ($\eta = constant$). However, as has been mentioned, η is not constant for plane-strain and uniaxial tension, and therefore, η and $\bar{\eta}$ do not coincide.

Concerning the assessment of the fracture points, the Nakazima FE models did not reproduce the fracture itself. Consequently, the fracture points within the triaxiality space were determined using the experimental fracture strains presented in table 5.1 for uniaxial (E), plane-strain (E) and equi-biaxial (E) fractures. In this regard, it was assumed that fracture is attained when the numerical major strain reaches the corresponding experimental major strain at fracture (table 5.1). As depicted in figure 5.9, the three fracture points predicted in the numerical simulations coincide with the points obtained analytically.

Considering the results presented in this section, the numerical model reproduces the behaviour of the performed Nakazima tests in terms of stress triaxiality. In this regard, the fracture points predicted analytically and using FE coincide for

the same experimental fracture strains.

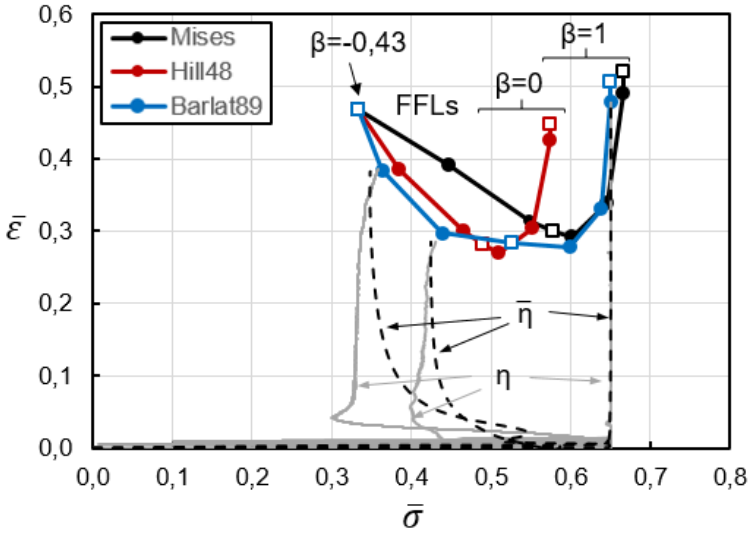

Figure 5.9. FFL and numerical evolution of Nakazima tests in the $\bar{\eta}$-$\bar{\varepsilon}$ space.

Chapter 6

Results

This chapter aims to present the results obtained in this research work, discussing the main contributions. Stretch and shrink flanging experiments are independently analysed in sections 6.1 and 6.2, respectively, using the experimental and numerical resources described in previous chapters.

6.1 Stretch flanging

This section contains the results corresponding to stretch flanging by SPIF. First, section 6.1.1 presents the stretch flanges obtained experimentally, describing and classifying the failure modes observed. Second, in section 6.1.2, the most representative flanges in terms of principal strains and formability are analysed. Third, in section 6.1.3, a validation of the numerical model for stretch flanging by SPIF is performed. Finally, in section 6.1.4, the numerical model is used to perform a formability analysis in terms of stress triaxiality.

It must be noted that the most relevant results concerning stretch flanging by SPIF presented in this section have been successfully published in a keynote international journal publication (López-Fernández *et al.*, 2021).

6.1.1 Experimental tests

The experimental campaign consisted of a series of stretch flanging experiments carried out following the stretch flanging process described in section 3.2. The aim of this series of tests is to obtain the process windows for different process parameters and discuss the characteristics of the principal modes of failure. For this purpose, the experimental tests presented in table 6.1 and table 6.2 were performed based on the different parameters presented in table 3.3. The set of parameters includes two different die radii (R_{die} = 45 mm and R_{die} = 20 mm), two tool diameters (ϕ_{tool} = 12 mm and ϕ_{tool} = 20 mm), two spindle speeds (S = 20 rpm and S = 1000 rpm) and different initial widths (w_0) and initial lengths (l_0). Note that at least two replicates were performed for every experiment to provide statistical meaning, resulting in more than 200 tests.

According to their mode of failure, the experiments were classified using the following nomenclature: S (safe) for the flanges produced successfully, F(E) for the cases that presented fracture at the edge, and F(C) for the flanges with fracture at the corner.

Flange radius (R_{die}) of 45 mm

	l_o (mm)	w_0 (mm)				
		36	**45**	**54**	**63**	**72**
(a) Φ_{tool} = 20 (mm) S = 20 (rpm)	15				S	
	20			S	F(E)	S
	25	S	S	F(C)		F(E)
	30	S	S			
	l_o (mm)	w_0 (mm)				
		36	**45**	**54**	**63**	**72**
(b) Φ_{tool} = 20 (mm) S = 1000 (rpm)	15				S	
	20			S	F(E)	S
	25	S	S	F(C)		F(C)
	30	S	S			
	l_o (mm)	w_0 (mm)				
		36	**45**	**54**	**63**	**72**
(c) Φ_{tool} = 12 (mm) S = 20 (rpm)	15					
	20	S		S	S	**S**
	25	S	S	F(C)	F(C)	**F(E)**
	30	S	S			
	l_o (mm)	w_0 (mm)				
		36	**45**	**54**	**63**	**72**
(d) Φ_{tool} = 12 (mm) S = 1000 (rpm)	15					
	20	S	S	S	S	S
	25	S	S	F(C)	F(C)	S
	30	S	S			F(C)

S (Safe), F (failure) either at (C) corner or at the (E) edge.

Table 6.1. Stretch flanging experiments corresponding to R_{die} = 45 mm. Tests in bold are analysed in section 6.1.2.

Furthermore, a colour-based code is used in table 6.1 and table 6.2 to easily identify the different regions, representing in green the safe zone, yellow the zone corresponding to failure at the corner and red the experiments with fracture at the edge. A more detailed description of the different modes of failure is presented in section 3.3.2.

In general terms, short and narrow flanges (low values of l_0 and w_0) for both die radii are within the safe zone, whereas large and wide flanges (high values of w_0 and l_0) fail either by fracture at the corner or by fracture at the edge. Regarding the tool diameter ϕ_{tool}, it did not exhibit a clear effect with respect to the mode of failure attained, with larger values increasing the safe zone for flanges corresponding to the largest die radius (R_{die} = 45 mm) but having the opposite effect for the flanges corresponding to the smallest die radius (R_{die} = 20 mm). With respect to the spindle speed S, the highest value (S = 1000 rpm) increased the safe zone independent of the die radius, as depicted in table 6.1 for R_{die} = 45 mm and in table 6.2 for R_{die} = 20 mm, which is in line with a previous trend observed by Borrego *et al.* (2016) in hole flanging experiments.

Flange radius (R_{die}) of 20 mm

(a)	l_o (mm)	w_0 (mm)				
		20	**24**	**28**	**32**	**36**
Φ_{tool} = 20 (mm)	15				S	S
S = 20 (rpm)	20	S	S	S	F(C)	F(C)
	25	S	S	S		
(b)	l_o (mm)	w_0 (mm)				
		20	**24**	**28**	**32**	**36**
Φ_{tool} = 20 (mm)	15				S	S
S = 1000 (rpm)	20	S	S	S	F(C)	F(C)
	25	S	S	S		
(c)	l_o (mm)	w_0 (mm)				
		20	**24**	**28**	**32**	**36**
Φ_{tool} = 12 (mm)	15		S	S	**S**	**F(E)**
S = 20 (rpm)	20	S	S	S	S	F(C)
	25	S	S	F(C)	F(C)	
(d)	l_o (mm)	w_0 (mm)				
		20	**24**	**28**	**32**	**36**
Φ_{tool} = 12 (mm)	15					S
S = 1000 (rpm)	20	S	S	S	S	F(E)
	25	S	S	S	F(C)	

S (Safe), F (failure) either at (C) corner or at the (E) edge.

Table 6.2. Stretch flanging experiments corresponding to R_{die} = 20 mm. Tests in bold are analysed in section 6.1.2.

To perform a deeper analysis of the relation between the flange geometry and the failure mode attained, the experiments presented in table 6.1c and table 6.2c will be analysed independently.

First, the analysis is focused on the experiments corresponding to $R_{die} = 45$ mm presented in table 6.1c. In this table, flanges with initial widths w_0 less than 54 mm were in the safe zone, and for these narrow flanges, the process was similar to a conventional sheet bending process. Two examples of narrow flanges are depicted in figure 6.1. Although they are in the safe zone, narrow flanges with high l_0 sometimes do not have the desired geometry due to the springback effect. With respect to the initial length l_0, flanges with values of l_0 less than 25 mm are always within the safe zone, as these flanges are too short to be stretched by the forming tool. Figure 6.2a and figure 6.2b contain two examples of short flanges, corresponding to equal initial length l_0 of 20 mm and initial widths w_0 of 54 mm and 72 mm, respectively. However, it must be mentioned that for initial lengths of less than 15 mm, the resulting flanges have a very small flange height that hardly adapts to the bending radius of the die. Concerning the experiments in the unsafe zone, which corresponds to flanges of high initial length and high initial width, the predominant failure is fracture at the corner. For this geometry, the flanges are narrow enough to twist alternatively due to tool-sheet friction, causing cyclic plastic straining at the corner of the flange and, consequently, fracture at the corner, as shown in figure 6.3b.

Nevertheless, for some flanges, the failure mode attained is fracture at the edge (see figure 6.3a). In these cases, fracture occurs due to the tensile strains at the edge of the flange before cyclic straining produces fracture at the corner. As will be discussed in section 6.1.2, the fracture does not necessarily initiate at the very edge but may appear at a certain distance from it and then propagate toward the edge. Additionally, it is worth noting that many tests were performed at step down $\Delta z = 0.2$ mm, leading to the conclusion that this value causes more cyclical straining than the current value of $\Delta z = 0.4$ mm. In this regard, for $\Delta z = 0.4$ mm, the number of tool passes for equal initial length is lower, avoiding some fractures at corners. This analysis result was why the final experiments were performed at $\Delta z = 0.4$ mm.

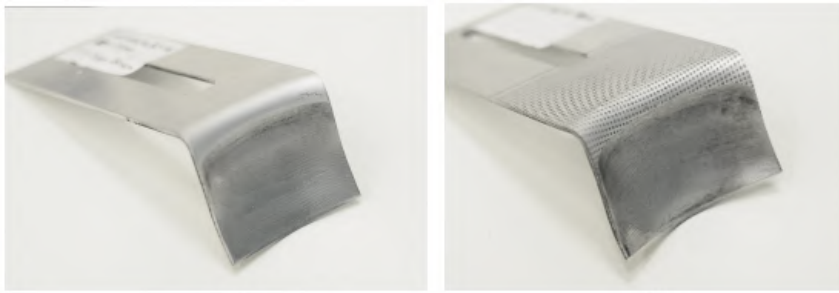

Figure 6.1. Narrow stretch flanges included in table 6.1c corresponding to (a) an initial width of $w_0 = 36$ mm and an initial length of $l_0 = 30$ mm and (b) an initial width of $w_0 = 45$ mm and an initial length of $l_0 = 30$ mm.

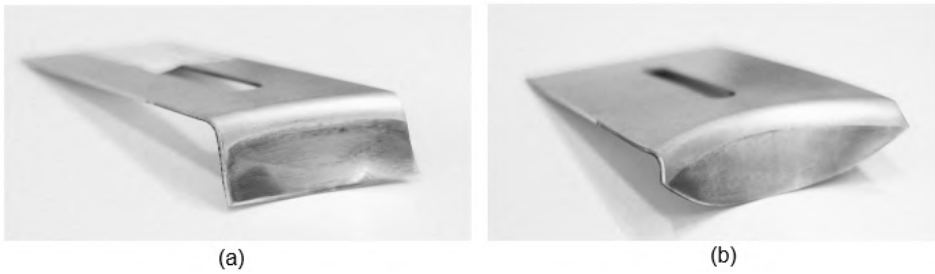

Figure 6.2. Stretch flanges included in table 6.1c corresponding to (a) an initial width of $w_0 = 54$ mm and an initial length of $l_0 = 20$ mm and (b) an initial width of $w_0 = 72$ mm and an initial length of $l_0 = 20$ mm.

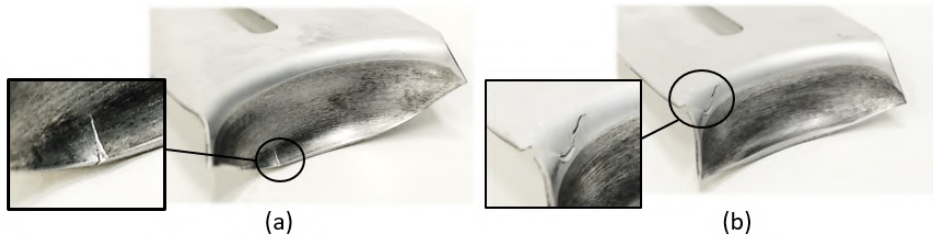

Figure 6.3. Stretch flanges included in table 6.1c failed by (a) fracture at the corner ($w_0 = 63$ mm and $l_0 = 25$ mm) and (b) fracture at the edge ($w_0 = 72$ mm and $l_0 = 25$ mm).

Regarding the experiments for $R_{die} = 20$, the flanges contained in table 6.2c were analysed. For this die radius, flanges with initial widths w_0 less than 32 mm were successfully processed. As depicted in figure 6.4, the principal concave radius of the flanges corresponding to $w_0 = 20$ mm and $w_0 = 24$ mm is very mild, and their final shape is obtained in a sheet-bending operation. Additionally, although the flanges with low w_0 did not present fractures, they showed more springback than flanges with larger w_0. In this regard, the successful flanges in the centre of table 6.2c, e.g., the flanges depicted in figure 6.5, present less springback and have a principal concave radius that is more pronounced than that of flanges with lower w_0. With respect to the failure zone, both failure at the corner and failure at the edge were obtained. Concretely, the flanges with larger l_0 presented fracture at the corner (figure 6.6a), as they were subjected to more cyclical straining compared to flanges with lower l_0. In contrast, the flange of $w_0 = 36$ mm and $l_0 = 15$ mm depicted in figure 6.6b failed by fracture at the edge.

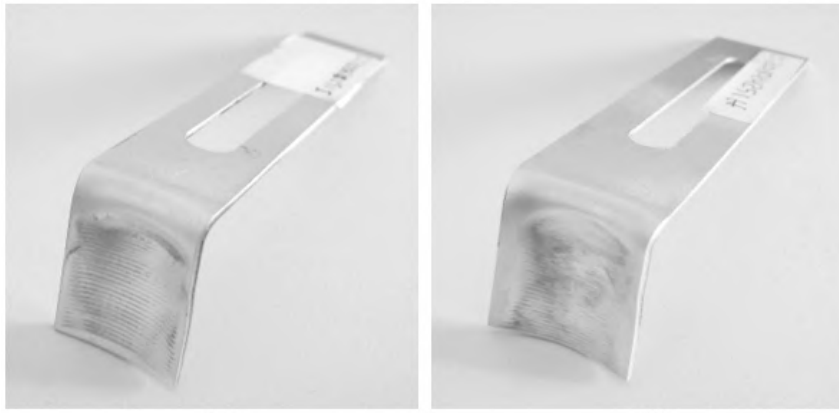

Figure 6.4. Narrow stretch flanges included in table 6.2c corresponding to (a) an initial width of $w_0 = 20$ mm and an initial length of $l_0 = 25$ mm and (b) an initial width of $w_0 = 24$ mm and an initial length of $l_0 = 25$ mm.

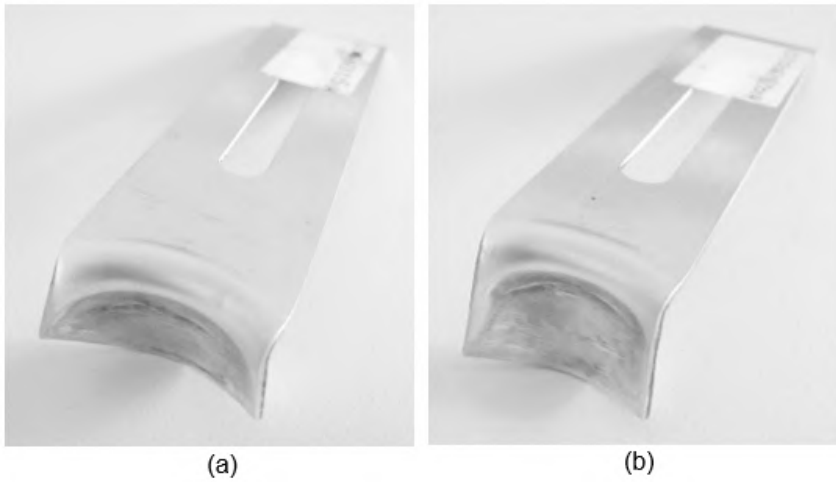

Figure 6.5. Stretch flanges included in table 6.2c corresponding to (a) $w_0 = 32$ mm and $l_0 = 15$ mm and (b) $w_0 = 28$ mm and $l_0 = 20$ mm.

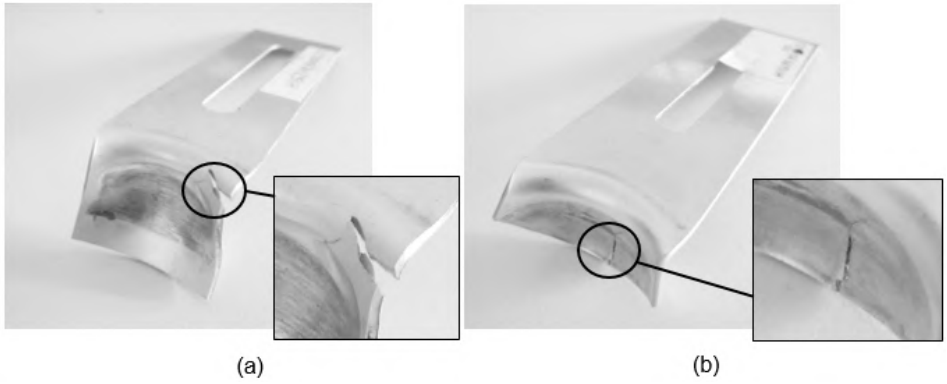

Figure 6.6. Failed stretch flanges included in table 6.2c corresponding to (a) fracture at the corner ($w_0 = 32$ mm and $l_0 = 25$ mm) and (b) fracture at the edge ($w_0 = 36$ mm and $l_0 = 15$ mm).

6.1.2 Strain analysis

The analysis within the principal strain space focuses on four flanges selected from the tests presented in section 6.1.1, corresponding to the cases highlighted in bold in table 6.1c and table 6.2c. These flanges are the most representative for studying the transition from the successful manufacturing of a flange to failure by fracture at the edge. The aim of this analysis is twofold: (i) understanding the strain conditions that lead to fracture in stretch flanging by SPIF and (ii) evaluating the formability attained in stretch flanging compared to the conventional FFL obtained from Nakazima tests. For this purpose, following the methodology detailed in section 3.3.1, two tests for each die radius (R_{die} = 45 mm and R_{die} = 20 mm) with fixed tool diameter ϕ_{tool} = 12 mm and spindle speed S = 20 rpm were analysed. In the case of the larger die radius R_{die} = 45 mm, the transition from the safe zone to fracture in table 6.1 was analysed at constant initial width w_0 = 72 mm, whereas for the smaller die radius R_{die} = 20 mm, this transition was attained at constant initial length l_0 = 15 mm.

Concerning the larger die radius R_{die} = 45 mm, the two experiments analysed are of fixed initial width w_0 = 72 mm and initial lengths l_0 = 20 mm and l_0 = 25 mm, corresponding to the successful flange and the flange that failed by fracture at the edge F(E) presented in table 6.1c.

In this regard, the contour of thickness reduction obtained using Argus® for the successful flange is depicted in figure 6.7a. For the same flange, figure 6.7c shows the principal strain distribution within the FLD, with the points coloured based on the thickness reduction and including the FFL obtained for the AA2024-T3 sheet. Additionally, the section depicted in blue in figure 6.7a is represented in the principal strain diagram (figure 6.7c) by a white-circle dotted line. This section is located in the flange longitudinally and coincides with the point where fracture occurred in the flanges that failed by fracture at the edge F(E). The last point of the section was obtained by thickness measurement using the methodology detailed in section 3.3.1. As this point is at the edge of the flange and, therefore, subjected to pure tension conditions, it was forced to be on the $\beta = -0.43$ line for this material according to the Barlat 89 yield criterion.

Likewise, for the flange that failed by fracture at the edge for R_{die} = 45 mm, figure 6.7b and figure 6.7d present the thickness strain contour and the principal strain distribution within the FLD, respectively. In this case, the section is located along the flange and coincides with the actual fracture attained for this test.

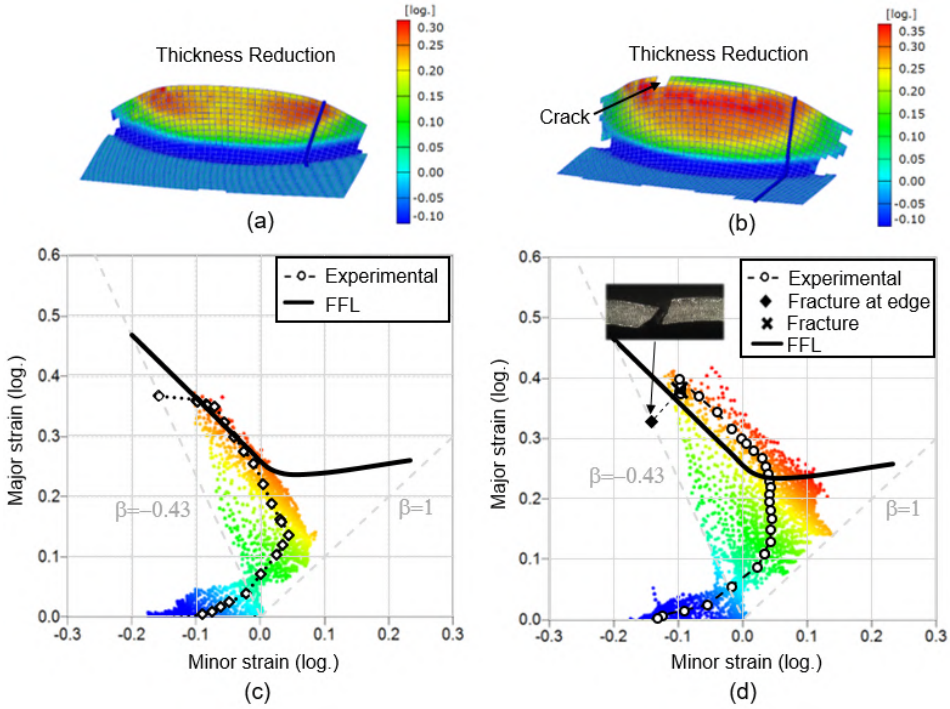

Figure 6.7. Formability analysis within the principal strain space of stretch flanges corresponding to $\phi_{tool} = 12$ mm, $S = 20$ rpm, $R_{die} = 45$ mm and $w_0 = 72$ mm: contour of thickness reduction for (a) $l_0 = 20$ mm and (b) $l_0 = 25$ mm with the corresponding FLD in (c) and (d), respectively.

The location of the fracture in the principal strain diagram is represented in figure 6.7d by a black diamond, along with a picture of the crack.

If both flanges are compared, it can be seen that the maximum levels of thickness reduction are higher in the failed flange than in the successful flange. Indeed, in the flange that failed by fracture at the edge, fracture occurs at the location of the edge with the highest thickness reduction. According to the principal strain diagram, the maximum levels of principal strains are above the FFL for both the successful flange and the failed flange. However, the flange that failed by fracture at the edge presented a larger number of points with higher strain levels compared to the successful specimen. In addition, in the case of the successful flange and in the absence of fracture, there were a number of points slightly above the FFL. These results demonstrate the increase in formability of flanging by SPIF

with respect to the conventional limits represented by the FFL obtained by means of Nakazima tests. These results agree with the increase in formability observed for hole flanging by SPIF of aluminium sheets by Martínez-Donaire *et al.* (2019) and stainless steel sheets by Centeno *et al.* (2014). Furthermore, focusing on the principal strain diagram of the failed flange depicted in figure 6.7d, the strains at the points labelled as "fracture at edge" are lower than the strain levels for points inside from the edge. Based on this observation, it can be suggested that fracture did not occur at the very edge but slightly inside from the edge.

Analogously, the previous study was performed for the experiments with $R_{die} = 20$ mm. In this case, the transition from the successful zone to fracture was analysed at constant initial length $l_0 = 15$ mm and for two different initial widths $w_0 = 32$ mm and $w_0 = 36$ mm. These experiments correspond to the successful flange and the flange that failed by fracture at the edge highlighted in bold in table 6.2c.

Consequently, for the successful case of $w_0 = 32$ mm, figure 6.8a and figure 6.8c depict the thickness reduction contour and the strain distribution within the FLD obtained from the software Argus®. In this case, the most representative section was located in the centre of the flange, coinciding with the location where the fracture occurred for failed flanges corresponding to $R_{die} = 20$ mm. For the flange that failed by fracture at the edge F(E), figure 6.8b and figure 6.8d present the thickness reduction contour and the diagram of principal strains, respectively. As for the case of $R_{die} = 45$ mm, the section is represented in the principal strain diagram (6.8d) using a white-dotted line. Furthermore, the strains at fracture were obtained by thickness measurement and represented using a black diamond along with the fractography of the crack for this flange.

According to the strain contours for both the successful and failed flanges, the highest levels of thickness reduction are located at the centre of the flange near the edge. Then, focusing on the principal strain diagrams, the highest strain levels are below the FFL for the successful flange (figure 6.8c), whereas for the failed flange (figure 6.8d), they are above the FFL. In this regard, although the number of points above the FFL is not as high as in the case of $R_{die} = 45$ mm, the number of points above this limit also demonstrates an increase in formability for this die radius.

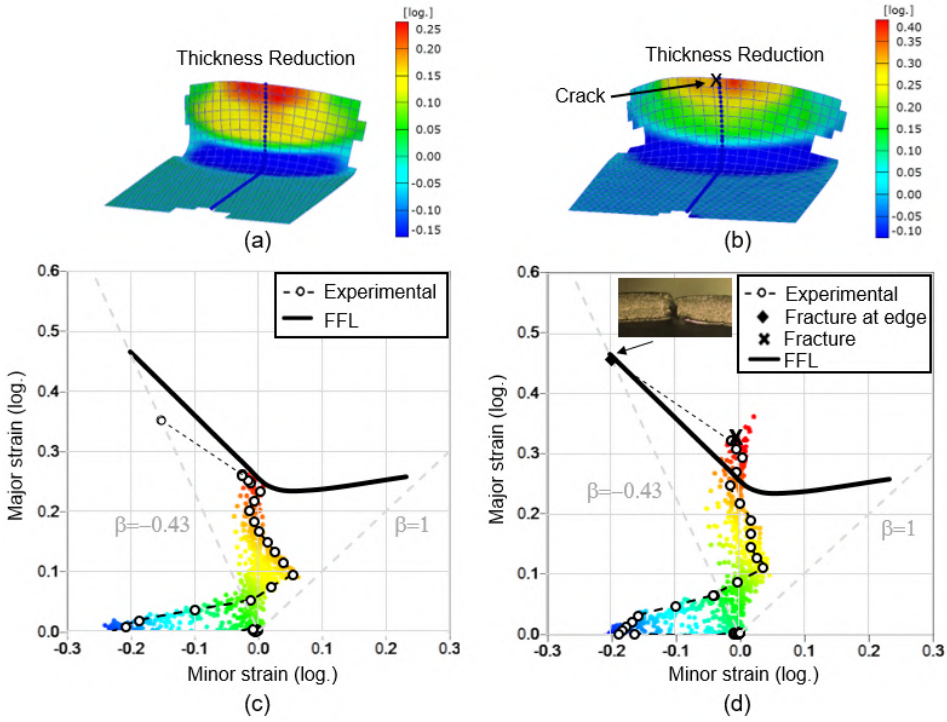

Figure 6.8. Formability analysis within the principal strain space of stretch flanges corresponding to $\phi_{tool} = 12$ mm, $S = 20$ rpm, $R_{die} = 20$ mm and $l_0 = 15$ mm: contour of thickness reduction for (a) $w_0 = 32$ mm and (b) $w_0 = 36$ mm with the corresponding FLD in (c) and (d), respectively.

6.1.3 Validation of the numerical model

In this section, the FE model corresponding to stretch flanging by SPIF is validated in terms of principal strains. With this aim, the four experiments analysed in section 6.1.2 were reproduced numerically and critically compared with the corresponding experimental strains. Concretely, strain validation was performed using the experimental and numerical results obtained from both the major strain contours and the strain distribution of the most representative section of each flange. A similar validation in terms of principal strains was used for stainless steel by Centeno *et al.* (2017).

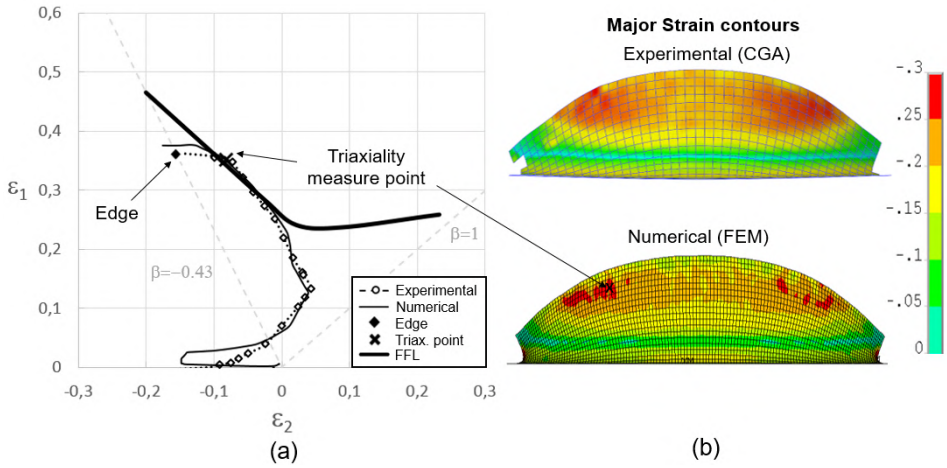

Figure 6.9. Validation of numerical modelling: (a) comparison of numerical vs. experimental principal strains and (b) experimental and numerical major strain contours (the figures correspond to the successful case $\phi_{tool} = 12$ mm, $S = 20$ rpm, $R_{die} = 45$ mm, $l_0 = 20$ mm and $w_0 = 72$ mm).

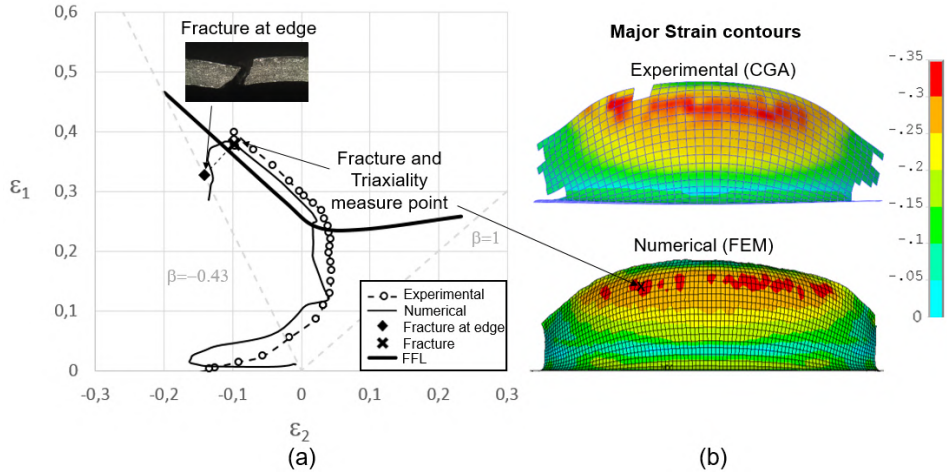

Figure 6.10. Validation of numerical modelling: (a) comparison of numerical vs. experimental principal strains and (b) experimental and numerical major strain contours (the figures correspond to the failed case $\phi_{tool} = 12$ mm, $S = 20$ rpm, $R_{die} = 45$ mm, $l_0 = 25$ mm and $w_0 = 72$ mm).

First, focusing on $R_{die} = 45$ mm, figure 6.9 and figure 6.10 show the numerical

and experimental results obtained for the successful flange S and the flange that failed by fracture at the edge F(E), respectively. On the one hand, the strain distributions within the FLD of the selected sections are depicted in figure 6.9 and figure 6.10 for both flanges, showing good agreement between the numerical and experimental results. On the other hand, the numerical and experimental major strain contours of the flanges are shown in figure 6.9b and figure 6.10b.

The numerical model generally reproduces the major strains of the experimental flanges in terms of the strain distribution and level of maximum strain. In this regard, it should be noted that the experimental measurements obtained using CGA do not allow evaluation of the strains at the very edge of the sheet; therefore, the numerical contours provide additional information from the flange edge.

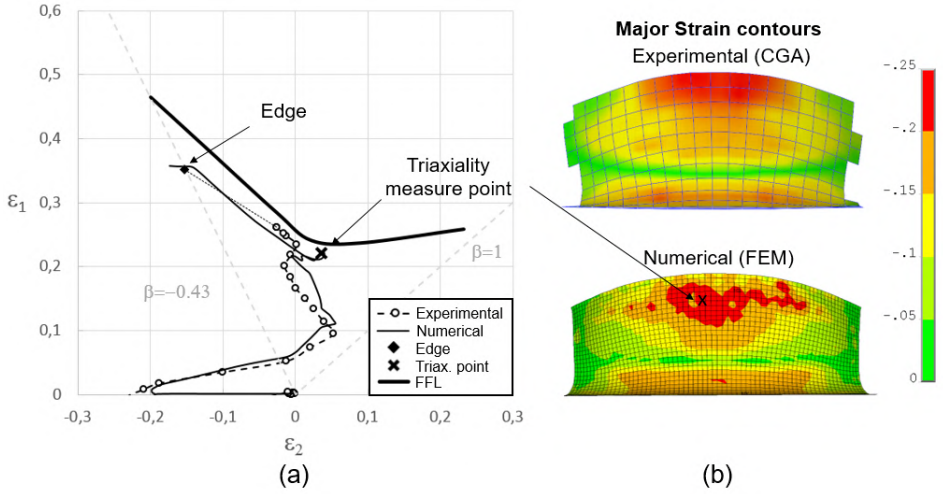

Figure 6.11. Validation of numerical modelling: (a) comparison of numerical vs. experimental principal strains and (b) experimental and numerical major strain contours (the figures correspond to the successful case $\phi_{tool} = 12$ mm, $S = 20$ rpm, $R_{die} = 20$ mm, $l_0 = 15$ mm and $w_0 = 32$ mm).

Analogously, the previous analysis was performed for a successful flange and a failed flange corresponding to $R_{die} = 20$ mm. In this regard, figure 6.11 and figure 6.12 show the major strain contours and the strain distribution of the most representative section (located in the centre of the flange) for both flanges. As depicted in figure 6.11a and figure 6.12a, the numerical and experimental strain

results from these sections are in good agreement for both flanges. Indeed, at the last point of the section, the numerical prediction also agrees with the strains obtained by thickness measurement. Regarding the strain contours, the FE model reproduces the distribution of major strains, which are maximal at the centre of the flange and near the edge for $R_{die} = 20$ mm. The edge of the flange is not represented in the experimental contour, with the strains at the edge of the flange depicted only in the numerical major strain contours.

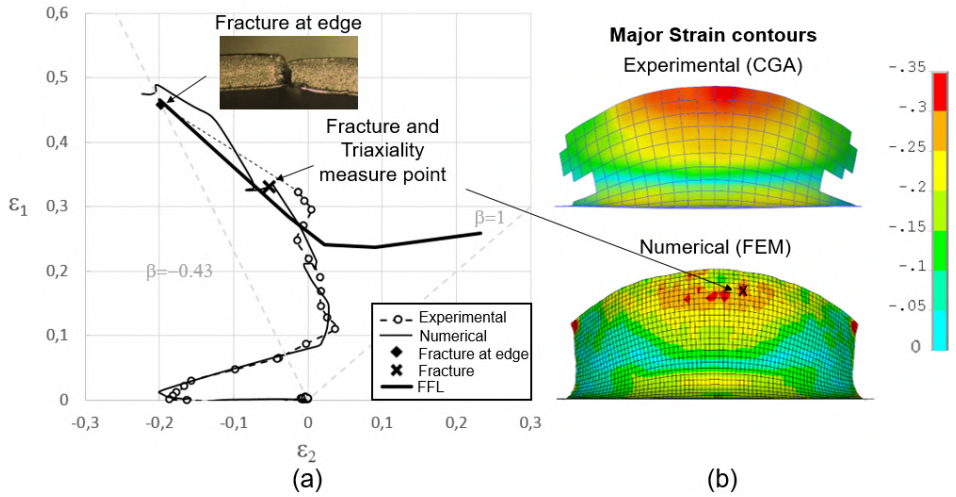

Figure 6.12. Validation of numerical modelling: (a) comparison of numerical vs. experimental principal strains and (b) experimental and numerical major strain contours (the figures correspond to the failed case $\phi_{tool} = 12$ mm, $S = 20$ rpm, $R_{die} = 20$ mm, $l_0 = 15$ mm and $w_0 = 36$ mm).

Based on the good agreement of the experimental and numerical results, it can be concluded that the numerical model successfully reproduces the behaviour of the stretch flanging process by SPIF and can therefore be used to provide accurate predictions in terms of principal strains and modes of failure. In this regard, the numerical model will be used in section 6.1.4 to perform a formability analysis in terms of stress triaxiality.

6.1.4 Stress triaxiality analysis

The results presented in section 6.1.2 showed that the strain levels attained in stretch flanging by SPIF exceed the conventional formability limit, which is represented by the FFL for materials without necking. As a consequence, in this process, the onset of fracture cannot be adequately predicted based only on the material FLD. In this regard, previous studies suggested the use of average stress triaxiality vs. equivalent strain ($\bar{\eta}$ vs. $\bar{\varepsilon}$) diagrams to make failure predictions in SPIF (Mirnia and Shamsari (2017), Magrinho *et al.* (2019), Martínez-Donaire *et al.* (2019)). In this section, the triaxiality approach to the prediction of failure presented by Martínez-Donaire *et al.* (2019) will be reproduced using the Barlat 89 yield criterion for stretch flanging by SPIF. With this aim, the FFL of the material for proportional loading obtained in section 5.2.2, along with the corresponding results obtained for stretch flanging by SPIF, will be analysed in the $\bar{\eta}$-$\bar{\varepsilon}$ space.

First, the FFL curves of the material in the triaxiality space are presented in figure 6.13 and figure 6.14 for the different yield criteria presented in section 5.2.2. The black curve corresponds to the FFL for the Barlat yield criterion, whereas the grey curve is the FFL obtained using the von Mises isotropic yield criterion. As depicted, the average stress triaxiality values evaluated at fracture, which in the case of proportional loading coincide with the stress triaxiality ratio, obtained for the two curves are different. In the isotropic case, the triaxiality ratio corresponds to $\eta = 0.33$, $\eta = 0.58$ and $\eta = 0.67$ for the pure tension, plane strain and equi-biaxial Nakazima tests, respectively. In contrast, for the same tests, the predictions of the Barlat 89 yield criterion correspond to $\eta = 0.33$, $\eta = 0.53$ and $\eta = 0.65$, respectively. Consequently, it can be affirmed that the FFLs predicted using both yield criteria are different in the stress triaxiality space.

Additionally, the flanges studied in section 6.1.3 were analysed within the triaxiality space along with the two FFL curves presented above. In this regard, figure 6.13 and figure 6.14 present the evolution in the $\bar{\eta}$-$\bar{\varepsilon}$ space of the flanges corresponding to $R_{die} = 45$ mm and $R_{die} = 20$ mm, respectively, using blue colour for the successful cases and red colour for the evolution of the failed flanges. Furthermore, for the fractured specimens, the fracture point is marked with "x" in the diagrams. The points at which $\bar{\eta}$ and $\bar{\varepsilon}$ were evaluated are presented in figures 6.9-6.12 under the label "triaxiality measure point". In the failed flanges, these critical points are located at the fracture locus, whereas in the successful flanges, they are the points with the highest equivalent strain $\bar{\varepsilon}$.

As seen in figure 6.13 and figure 6.14, for the four flanges analysed, the aver-

age stress triaxiality levels are lower than the values attained in the FFL curves, whereas the equivalent strains are much higher than the FFL curves. In this regard, it can be affirmed that the evolution of the critical points in the $\bar{\eta}$-$\bar{\varepsilon}$ diagram occurs in a different region than the one where the Nakazima tests evolve. Consequently, the FFL curves expressed in the $\bar{\eta}$-$\bar{\varepsilon}$ diagram do not allow the fracture in stretch flanging by SPIF to be successfully predicted.

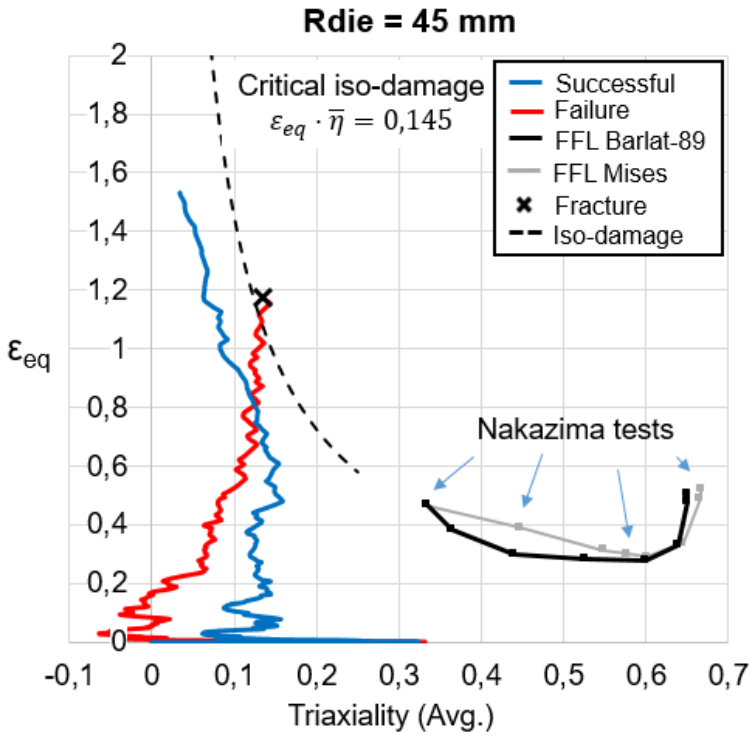

Figure 6.13. Analysis within the stress triaxiality space corresponding to a successful flange and a flange that failed by fracture at the edge for $R_{die} = 45$ mm.

To assess the onset of fracture in the $\bar{\eta}$-$\bar{\varepsilon}$ diagram, a different approach is proposed. It consists of using the Atkins equation (Atkins, 1996), which is based on the damage criteria proposed by McClintock (McClintock, 1968), to illustrate a possible limit in the triaxiality space. This limit is expressed using an iso-damage curve that follows the expression $\bar{\eta} \cdot \bar{\varepsilon} = k$ and is represented using a dotted line in figure 6.13 and figure 6.14. For these flanges, the critical value "k", which represents the value at which fracture occurs, is a material constant estimated

from the average value of the different flanges analysed. Based on this approach, the flanges that failed by fracture at the edge presented in figure 6.13 and figure 6.14 (red lines) present a higher level of accumulated damage than the successful flanges (blue lines). Furthermore, the equivalent strains are higher in successful flanges than in failed flanges, evidencing that the equivalent strain is not suitable by itself for making fracture predictions.

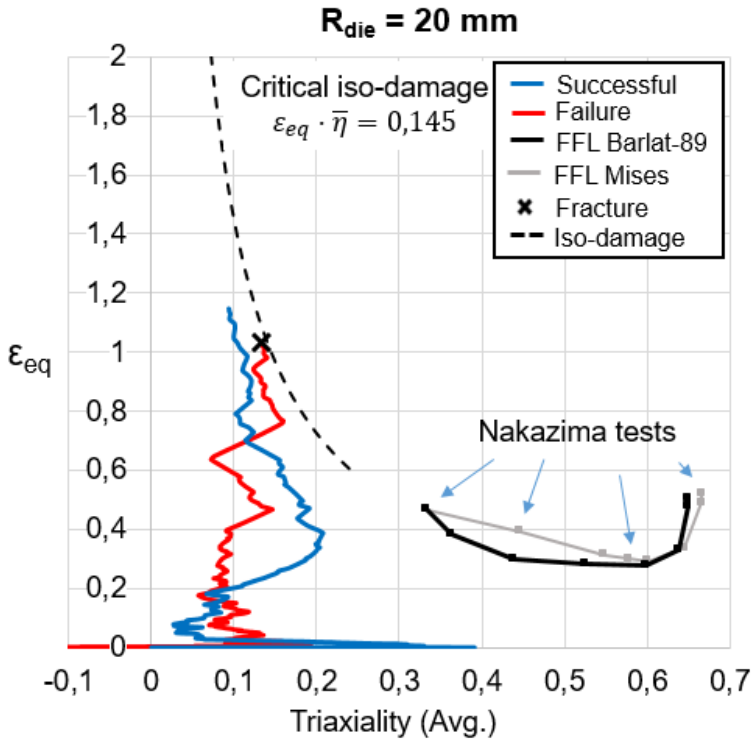

Figure 6.14. Analysis within the stress triaxiality space corresponding to a successful flange and a flange that failed by fracture at the edge for $R_{die} = 20$ mm.

6.2 Shrink flanging

This section contains the results corresponding to shrink flanging by SPIF. Section 6.2.1 presents the experimental tests carried out, classifying and describing the principal modes of failure attained. In section 6.2.2, the most representative shrink flanges in the principal strain space are analysed, discussing their prin-

cipal characteristics in terms of formability. In section 6.2.3, the numerical model is validated in terms of principal strains using the experimental results obtained in section 6.2.2. In section 6.2.4, the final geometry of the flanges are analysed, and the experimental results are compared with FE predictions. Finally, section 6.2.5 presents a new approach to failure prediction in shrink flanging based on the analysis of compression stresses.

6.2.1 Experimental tests

This section presents the results of the experimental campaign performed for shrink flanging by SPIF. A set of tests were carried out to analyse the principal modes of failure and the influence of different process parameters on the material formability. The parameters analysed include two principal die radii ($R_{die} = 45$ mm and $R_{die} = 20$ mm), two different tool diameters ($\phi_{tool} = 12$ mm and $\phi_{tool} = 20$ mm), two spindle speeds ($S = 20$ rpm and $S = 1000$ rpm) and different values of initial width (w_0) and initial length (l_0). The flanges resulting from the combination of these parameters are summarized in table 6.3 and table 6.4, which represent the process windows for $R_{die} = 45$ mm and $R_{die} = 20$ mm, respectively. Similar to the process window obtained for stretch flanging, at least two replicates were performed for every experiment to provide statistical meaning.

The experiments were classified using the following nomenclature: S (safe) for flanges processed successfully, F(W) for flanges that failed by wrinkling and F(IW) for failed flanges that presented a polygonal profile as a consequence of incipient but stable wrinkling, named incipient wrinkling hereafter. Additionally, in table 6.3 and table 6.4, the experiments corresponding to successful flanges are coloured in green, whereas red and yellow colours correspond to flanges that failed by wrinkling and flanges that failed by incipient wrinkling, respectively. More details about the characteristics of the different modes of failure in shrink flanging by SPIF can be found in section 3.3.2.

According to the process windows presented in table 6.3 and table 6.4, the results obtained when processing a flange by SPIF are very different depending on the die radius (R_{die}). In this regard, flanges formed using $R_{die} = 45$ mm were susceptible to failing either by wrinkling F(W) or by incipient wrinkling F(IW), whereas for flanges corresponding to $R_{die} = 20$ mm, only failure by incipient wrinkling was attained. Furthermore, the process parameters also had different effects depending on R_{die}. On the one hand, for the largest die radius ($R_{die} = 45$ mm), reducing the tool diameter from $\phi_{tool} = 20$ mm to $\phi_{tool} = 12$ mm slightly

Flange radius (R_{die}) of 45 mm

(a) Φ_{tool} = 20 (mm), S = 20 (rpm)

l_o (mm)	w_0 (mm)				
	36	45	54	63	72
10			S	F(W)	F(W)
15		S	F(W)	F(W)	F(W)
20	S	F(IW)			
25	F(IW)	F(IW)			

(b) Φ_{tool} = 20 (mm), S = 1000 (rpm)

l_o (mm)	w_0 (mm)				
	36	45	54	63	72
10			S	F(W)	F(W)
15		S	F(W)	F(W)	F(W)
20	S	F(IW)			
25	F(IW)	F(IW)			

(c) Φ_{tool} = 12 (mm), S = 20 (rpm)

l_o (mm)	w_0 (mm)				
	36	45	54	63	72
10				**S**	S
15		S	S	**F(W)**	F(W)
20	S	F(IW)	**F(IW)**		
25	F(IW)	F(IW)			

(d) Φ_{tool} = 12 (mm), S = 1000 (rpm)

l_o (mm)	w_0 (mm)				
	36	45	54	63	72
10				S	S
15	S	S	S	F(W)	F(W)
20	S	F(IW)	F(IW)		
25	F(IW)	F(IW)			

S (Safe), F (failure) either by wrinkling (W) or by incipient wrinkling (IW).

Table 6.3. Shrink flanging experiments corresponding to R_{die} = 45 mm. Tests in bold are analysed in section 6.2.2.

increased the formability and produced more successful flanges, as depicted in table 6.3. The spindle speed in turn had no effect in these tests in terms of formability, obtaining the same results for flanges processed either at $S = 20$ rpm or at $S = 1000$ rpm. On the other hand, as depicted in table 6.4 for $R_{die} = 20$ mm, the process windows resulting from combining the different values of S and ϕ_{tool} were identical.

To perform a more exhaustive analysis of the influence of the initial width w_0 and initial length l_0 on the flanges and the modes of failure, some results provided in table 6.3 and table 6.4 will be discussed separately. Focusing on the flanges for $R_{die} = 45$ mm presented in table 6.3c, it can be seen that increasing the initial length l_0 and the initial width w_0 reduced the formability, in some cases producing failed flanges. As a result, the transition from the successful zone to the failed zone

Flange radius (R_{die}) of 20 mm

(a)	l_o (mm)	w_0 (mm)				
		20	**24**	**28**	**32**	**36**
Φ_{tool} = **20 (mm)**	15	S	S	S	F(IW)	F(IW)
S = 20 (rpm)	20	S	S	F(IW)	F(IW)	F(IW)
	25					F(IW)

(b)	l_o (mm)	w_0 (mm)				
		20	**24**	**28**	**32**	**36**
Φ_{tool} = **20 (mm)**	15	S	S	S	F(IW)	F(IW)
S = 1000 (rpm)	20	S	S	F(IW)	F(IW)	F(IW)
	25					F(IW)

(c)	l_o (mm)	w_0 (mm)				
		20	**24**	**28**	**32**	**36**
Φ_{tool} = **12 (mm)**	15	S	S	**S**	**F(IW)**	F(IW)
S = 20 (rpm)	20	S	S	F(IW)	F(IW)	F(IW)
	25					F(IW)

(d)	l_o (mm)	w_0 (mm)				
		20	**24**	**28**	**32**	**36**
Φ_{tool} = **12 (mm)**	15	S	S	S	F(IW)	F(IW)
S = 1000 (rpm)	20	S	S	F(IW)	F(IW)	F(IW)
	25					F(IW)

S (Safe), F (failure) either by wrinkling (W) or by incipient wrinkling (IW).

Table 6.4. Shrink flanging experiments corresponding to $R_{die} = 20$ mm. Tests in bold are analysed in section 6.2.2.

is almost aligned with the diagonal. In this regard, flanges with small initial length l_0, e.g., the flanges depicted in figure 6.15, were successfully processed independent of their initial width w_0. The reason is that these flanges are not large enough to experience a level of compression that produces wrinkling. The flanges with medium initial length, e.g., the flange shown in figure 6.16a, were also successful if the initial width was 54 mm or less. These flanges are so narrow that there is not enough shrinking to produce wrinkles, and the flanging process is similar to a conventional bending operation.

Regarding the failed flanges, the factor that determined the mode of failure was the initial width w_0. In this case, failure by incipient wrinkling F(IW) was attained for narrow flanges from medium to large values of l_0. Figure 6.16b and figure 6.17b show two flanges that failed by incipient wrinkling corresponding to initial widths of $w_0 = 45$ mm and $w_0 = 54$ mm, respectively. As expected, the larger the initial width w_0 is, the higher the circumferential deformation. However, for w_0 larger than 54 mm, the flanges fail by wrinkling F(W), showing a number

of well-established wrinkles, as in the case of the flange depicted in figure 6.17a.

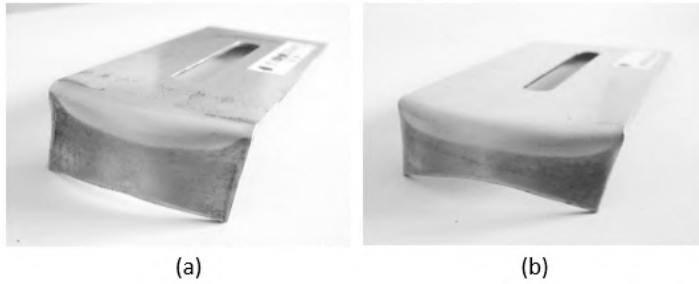

Figure 6.15. Successful shrink flanges included in table 6.3 corresponding to (a) $w_0 = 54$ mm and $l_0 = 15$ mm and (b) $w_0 = 63$ mm and $l_0 = 10$ mm.

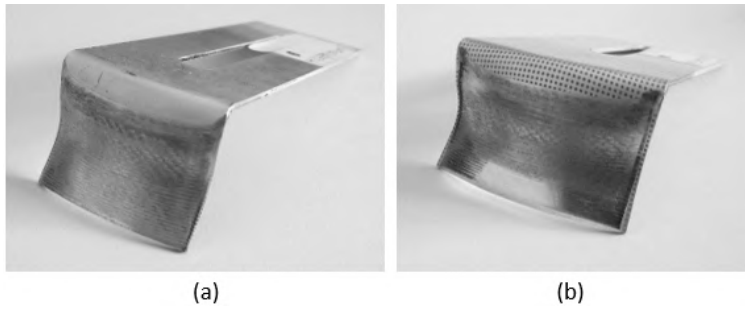

Figure 6.16. Narrow shrink flanges included in table 6.3 corresponding to (a) $w_0 = 36$ mm and $l_0 = 25$ mm and (b) $w_0 = 45$ mm and $l_0 = 25$ mm.

Figure 6.17. Failed shrink flanges included in table 6.3: (a) flange with wrinkles ($w_0 = 63$ mm and $l_0 = 15$ mm) and (b) flange with incipient wrinkles ($w_0 = 54$ mm and $l_0 = 20$ mm).

Regarding the flanges corresponding to $R_{die} = 20$ mm, the flanges analysed correspond to tests in table 6.4c. In contrast to the process window with $R_{die} = 45$ mm, these flanges fail only by incipient wrinkling F(IW). In general, the following rule applies for this die radius: short and narrow flanges (small w_0 and l_0) were successfully processed, whereas large and wide flanges (large w_0 and l_0) failed, in this case by incipient wrinkling. On the one hand, flanges of w_0 less than 28 mm, as presented in figure 6.18 and figure 6.19a, were successful for all the values of l_0 tested. However, as mentioned for $R_{die} = 45$ mm, the flanges with the smallest w_0 and the largest l_0 presented similar characteristics to straight flanges, with the effect of the die curvature almost negligible. On the other hand, flanges of w_0 larger than 28 mm presented failure by incipient wrinkling F(IW), even for small values of l_0, showing the polygonal shape depicted in figure 6.20b, which is characteristic of this mode of failure. Furthermore, the flanges that failed by incipient wrinkling F(IW) presented different degrees of shape deviation depending on the initial width w_0, with the wider flanges being more affected by this mode of failure. This effect becomes patent in the failed flanges depicted in figure 6.20. The flange of $w_0 = 36$ mm is clearly more deformed than the flange of $w_0 = 28$ mm.

Note that the highest value of initial width ($w_0 = 36$ mm) analysed for $R_{die} = 20$ mm coincides with the lowest value of w_0 tested for $R_{die} = 45$ mm. In this case, flanges of $w_0 = 36$ mm were successfully processed for the largest die radius ($R_{die} = 45$ mm), whereas for $R_{die} = 20$ mm, the flanges failed by incipient wrinkling F(IW). In this regard, it can be established that the die radius is determinant in the onset of failure by wrinkling, allowing more successful flanges to be processed as R_{die} increases.

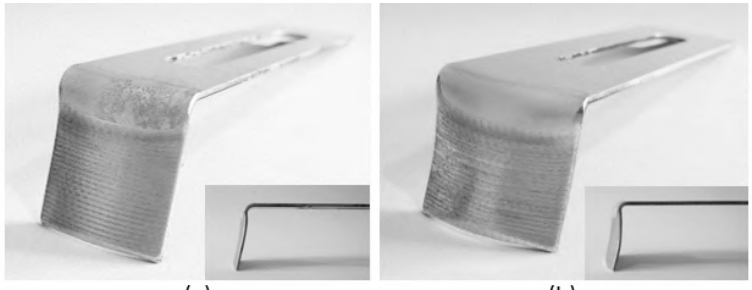

Figure 6.18. Narrow shrink flanges included in table 6.4 corresponding to (a) $w_0 = 20$ mm and $l_0 = 20$ mm and (b) $w_0 = 24$ mm and $l_0 = 20$ mm.

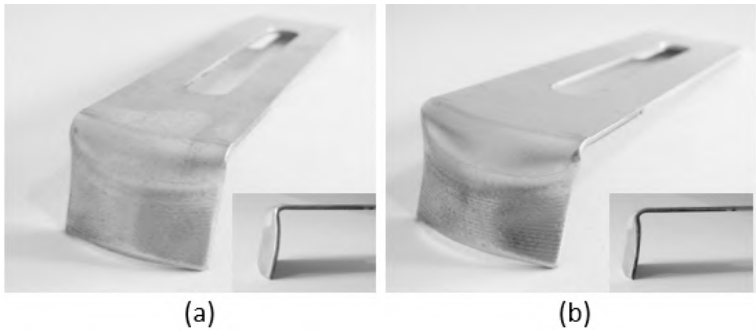

Figure 6.19. Successful shrink flanges included in table 6.4 corresponding to (a) $w_0 = 28$ mm and $l_0 = 15$ mm and (b) $w_0 = 24$ mm and $l_0 = 15$ mm.

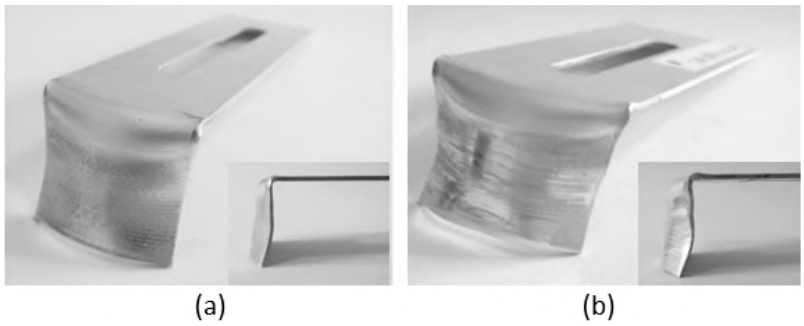

Figure 6.20. Failed shrink flanges included in table 6.4: (a) flange with incipient wrinkles corresponding to $w_0 = 28$ mm and $l_0 = 20$ mm and (b) flange with incipient wrinkles corresponding to $w_0 = 36$ mm and $l_0 = 20$ mm.

6.2.2 Strain analysis

This section presents the analysis within the principal strain space carried out on the shrink flanges processed by SPIF presented in section 6.2.1. In this regard, the most representative tests were selected to analyse the conditions leading to the different modes of failure. The strain distributions of these flanges were evaluated experimentally using CGA, following the methodology detailed in section 3.3.1. The results obtained were analysed within the FLD. The pure compression state was represented by $\beta = -2.33$ for AA2024-T3 assuming the Barlat 89 yield criterion.

With this aim, the five experiments highlighted in bold in table 6.3c ($R_{die} = 20$

mm) and table 6.4c (R_{die} = 45 mm) were analysed, all of which were performed at fixed values of spindle speed (S = 20 rpm) and tool diameter (ϕ_{tool} = 12 mm). Concretely, the flanges selected represent the transition from a successfully processed shrink flange to a failed flange, either by wrinkling or incipient wrinkling, allowing us to analyse the onset of the two failure modes attained in shrink flanging.

For R_{die} = 45 mm, the following flanges presented in table 6.3 were analysed: (i) a successful flange S of initial width w_0 = 63 mm and initial length l_0 = 10 mm, (ii) a flange that failed by wrinkling of w_0 = 63 mm and l_0 = 15 mm and (iii) a flange that failed by incipient wrinkling of w_0 = 54 mm and l_0 = 20 mm.

For the successful flange, the analysis of principal strains obtained using Argus® is depicted in figure 6.21. In this regard, figure 6.21a shows a picture of the inner side of the flange, i.e., the flange surface that was not in contact with the forming tool. This is the surface where the strains were evaluated using the CGA system. Figure 6.21c depicts the principal strain contours of the major strain, minor strain and thickness reduction.

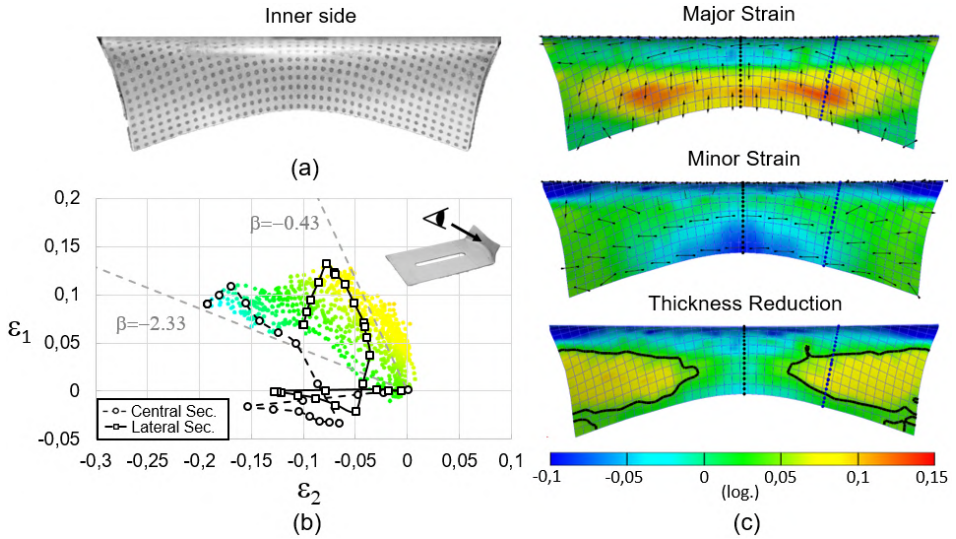

Figure 6.21. Formability analysis within the principal strain space corresponding to a successful shrink flange for R_{die} = 45 mm, ϕ_{tool} = 12 mm, S = 20 rpm, w_0 = 63 mm and l_0 = 10 mm: (a) flange surface, (b) strain distribution within the FLD and (c) strain contours. (Open dot ≡ centre section; square dots ≡ lateral section.)

The major and minor strains are presented within the FLD in figure 6.21b. The strain points are coloured as a function of the thickness reduction contour, as depicted in figure 6.21b. In this FLD, two sections were represented to analyse the strain distribution in the most representative regions of the flange. On the one hand, the central section longitudinally crossed the most compressed region, which is the location where wrinkle onset occurs in failed flanges. This section is represented in blue in figure 6.21c. On the other hand, is located a few millimetres from the central section at the location of the highest major strain. In addition, the pure tension and pure compression lines $\beta = -0.43$ and $\beta = -2.33$, respectively, are presented in the FLD for the AA2024-T3 sheet and according to the Barlat 89 plasticity criterion.

Similarly, the previous analysis was also carried out for the flanges that failed by wrinkling F(W) and by incipient wrinkling F(IW). In this regard, figure 6.22 and figure 6.23 present the strain contours and strain distribution within the FLD for these two flanges.

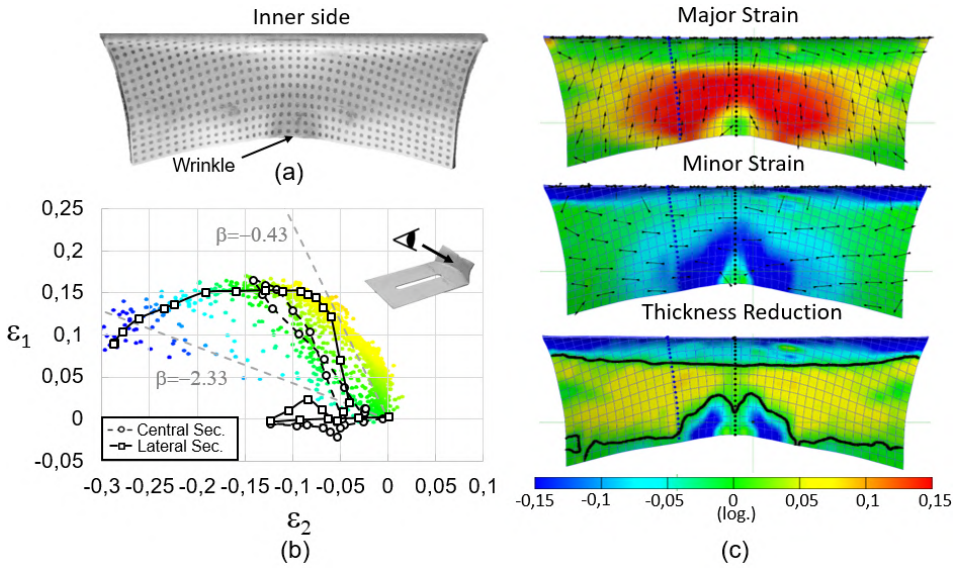

Figure 6.22. Formability analysis within the principal strain space corresponding to a flange that failed by wrinkling for $R_{die} = 45$ mm, $\phi_{tool} = 12$ mm, $S = 20$ rpm, $w_0 = 63$ mm and $l_0 = 15$ mm: (a) flange surface, (b) strain distribution within the FLD and (c) strain contours. (Open dot ≡ centre section; square dots ≡ lateral section.)

In general terms, the highest compression strains are located at the centre of

the flange for the three tests analysed, which is where wrinkles occur, whereas the sides of the flanges are undeformed. However, in the minor strain contours corresponding to the failed flanges (see figure 6.22c and figure 6.23)c, the centre of the flange edge presents lower strains than the adjacent regions. It is worth mentioning that when using the Argus system®, only the strains on the surface of the sheet can be evaluated. Consequently, if the sheet is bent, e.g., in the case of wrinkling, the strain values obtained depend on the face where the strains are evaluated, with the concave side of the wrinkle under compression and the convex side under tension. This effect can also be seen in the FLD for both flanges that failed by wrinkling and by incipient wrinkling, as depicted in figures 6.22b and 6.23b, respectively. In these cases, the last point of the lateral section (measured from the concave surface) presented lower values of minor strains than its homologous point in the central section (measured from the convex surface). Likewise, the major strains and thickness reduction strains are also influenced by this phenomenon, as seen in figure 6.22c.

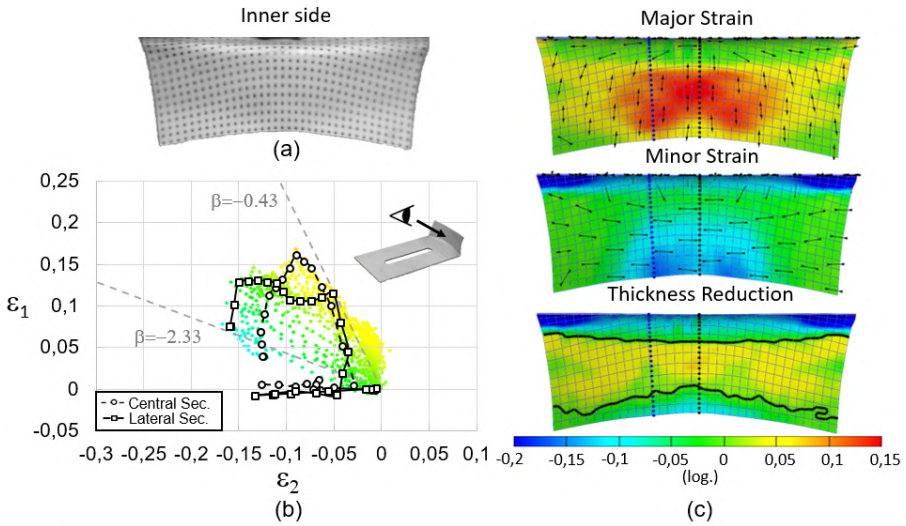

Figure 6.23. Formability analysis within the principal strain space corresponding to a flange that failed by incipient wrinkling for $R_{die} = 45$ mm, $\phi_{tool} = 12$ mm, $S = 20$ rpm, $w_0 = 54$ mm and $l_0 = 20$ mm: (a) flange surface, (b) strain distribution within the FLD and (c) strain contours. (Open dot ≡ centre section; square dots ≡ lateral section.)

According to the principal strain diagrams, the points corresponding to the successful flange are above the pure compression line, whereas in the FLDs cor-

responding to the failed flanges, there are points below this limit. Concretely, the points below the pure compression line correspond to the last points of the lateral sections for both failed flanges, which in both cases coincide with the compressed side of a wrinkle. Furthermore, in the successful flange, the levels of minor strain are higher than those in the wrinkled flange but lower than those in the flange exhibiting only incipient wrinkling. These results suggest that for their given width and length, the successful flange was closer to failure by wrinkling than it was to failure by incipient wrinkling.

Regarding the flanges corresponding to $R_{die} = 20$ mm, a similar strain analysis was carried out for the tests highlighted in bold in table 6.4. In this case, the tests correspond to a successful flange of $w_0 = 28$ mm and $l_0 = 15$ mm (figure 6.24) and a flange that failed by incipient wrinkling of $w_0 = 32$ mm and $l_0 = 15$ mm (figure 6.25). As seen in figure 6.24c and figure 6.25c, the strain distributions along the flange are similar to the strains obtained for $R_{die} = 45$ mm. In this regard, the highest levels of major strains are located at the centre of the flange, being higher in the failed flange than in the successful flange. The lowest levels of minor strains are located at the centre of the flange edge for both flanges. As expected, higher levels are observed in the failed flange.

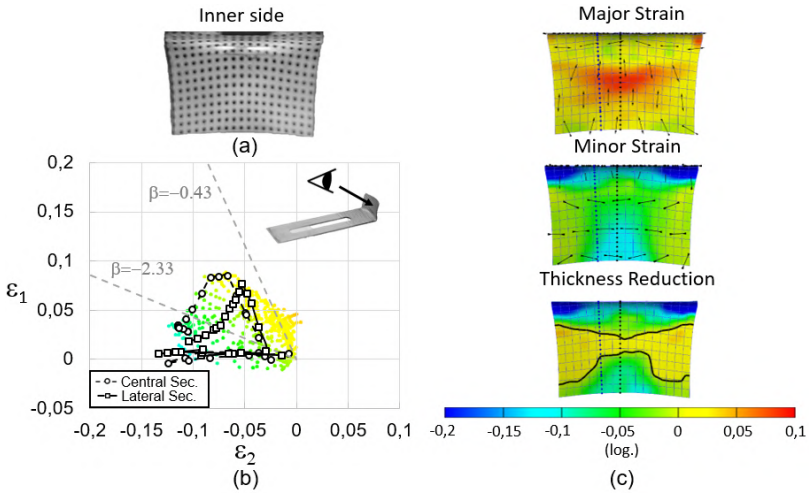

Figure 6.24. Formability analysis within the principal strain space corresponding to a successful shrink flange for $R_{die} = 20$ mm, $phi_{tool} = 12$ mm, $S = 20$ rpm, $w_0 = 28$ mm and $l_0 = 15$ mm: (a) flange wall, (b) FLD and (c) strain contours. (Open dot ≡ centre section; square dots ≡ lateral section.)

Additionally, incipient wrinkles can be seen in the thickness contour depicted in figure 6.25c, which presents two regions of thickness increase at the edge of the flange.

Focusing on the principal strain diagram, both flanges present lower levels of major strains than the flanges corresponding to $R_{die} = 45$ mm, whereas the minor strains are of a similar level. However, according to figure 6.24b and figure 6.25b, the flanges for $R_{die} = 20$ mm present strain points below the pure compression line ($\beta = -2.33$). In the case of the flange with incipient wrinkles, these points could be the result of measuring the strains on the surface of the wrinkles, as occurred for the failed flanges analysed previously. Nevertheless, in the successful flange, these levels of strains cannot be explained as a measurement effect, as this flange did not present wrinkles.

For these two flanges, the points below the pure compression line correspond to the edge of the flange; therefore, they can be analysed according to the last points of the two sections presented in the diagrams. In this regard, in the successful flange, the edge in the central section is more compressed (lower ε_2) than that in the lateral section. The reverse occurs in the failed flange as a consequence of the wrinkle appearance.

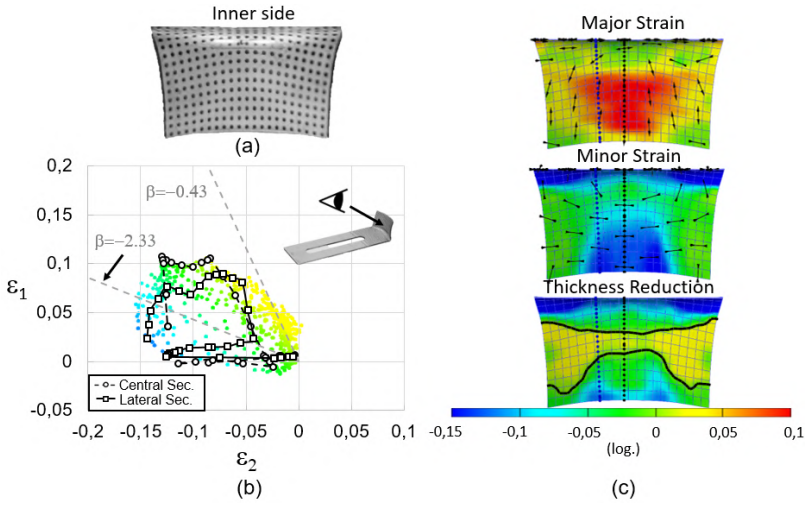

Figure 6.25. Formability analysis within the principal strain space corresponding to a shrink flange that failed by incipient wrinkling for $R_{die} = 20$ mm, $\phi_{tool} = 12$ mm, $S = 20$ rpm, $w_0 = 32$ mm and $l_0 = 15$ mm: (a) flange wall, (b) strain contours and (c) FLD. (Open dot ≡ centre section; square dots ≡ lateral section.)

In summary, it can be concluded that the strain levels and strain distributions for both flange radii analysed were similar. Furthermore, the analysis performed for $R_{die} = 20$ mm presented strain levels below the pure compression line of the material. This suggests that assuming the pure compression line as a wrinkling limit is not completely effective in the prediction of wrinkling for incremental forming, at least for flanges formed using small die radii.

Finally, due to the limitations of the CGA technique in measuring the strains in the presence of bending, it can be concluded that the study of wrinkling cannot be based only on the experimental analysis of principal strains using this method. In this regard, the next sections propose complementary analyses based on FE simulations and geometry analyses, providing a better understanding of the wrinkling phenomenon in shrink flanging by SPIF.

6.2.3 Validation of the numerical model

This section details the validation of the FE model used in the simulations of the shrink flanging process by SPIF. For this purpose, four shrink flanging tests were reproduced numerically, and their results were compared with the experimental results presented in section 6.2.2. For $R_{die} = 45$ mm, the flanges analysed were the successful flange ($w_0 = 63$ mm and $l_0 = 10$ mm) and the flange that failed by wrinkling ($w_0 = 63$ mm and $l_0 = 15$ mm) highlighted in bold in table 6.3c. For $R_{die} = 20$ mm, the analysis was carried out on the successful flange ($w_0 = 28$ mm and $l_0 = 15$ mm) and the flange that failed by incipient wrinkling ($w_0 = 32$ mm and $l_0 = 15$ mm) shown in table 6.4c.

Figure 6.26a and figure 6.27a show the strain distribution of the numerical and experimental central sections corresponding to flanges for $R_{die} = 45$ mm. In this regard, the evolution of the experimental and numerical principal strains for the successful flange are in good agreement. Although there are differences at the end of the sections, (i) these differences only involve less than 0.5 mm distance from the edge, and (ii) the experimental point right at the edge is not included in the experimental section, as it cannot be measured by CGA.

Regarding the numerical strain contours (see figure 6.26b), they reproduce the results included in the experimental analysis presented in figure 6.21b in that the highest values of major and minor strains are in the centre of the flange. In the analysis of the flange that failed by wrinkling, the FE model reproduced the three wrinkles depicted in figure 6.17a, although they were in the opposite direction with respect to the wrinkles obtained in the experimental flange. Note that wrinkling

is an unstable phenomenon; therefore, the direction of the wrinkles is aleatory.

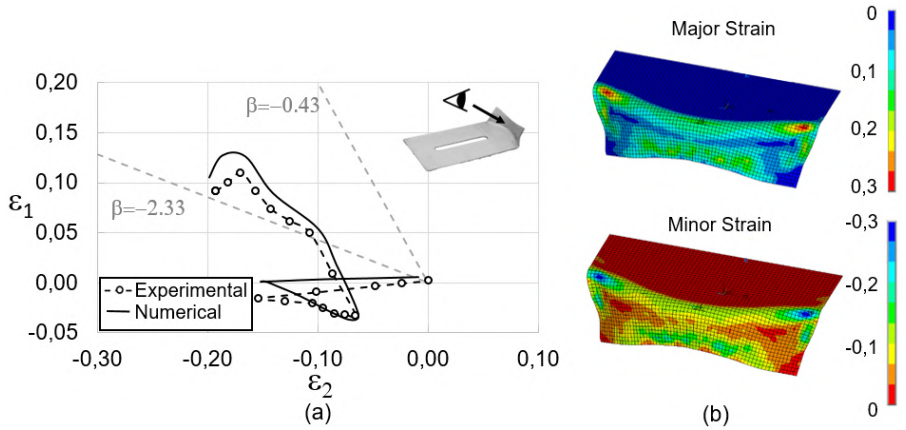

Figure 6.26. Validation of numerical modelling: (a) comparison of numerical vs. experimental principal strains in the central section of the flange and (b) numerical strain contours (the figures correspond to the successful case $\phi_{tool} = 12$ mm, $S = 20$ rpm, $R_{die} = 45$ mm, $l_0 = 10$ mm and $w_0 = 63$ mm).

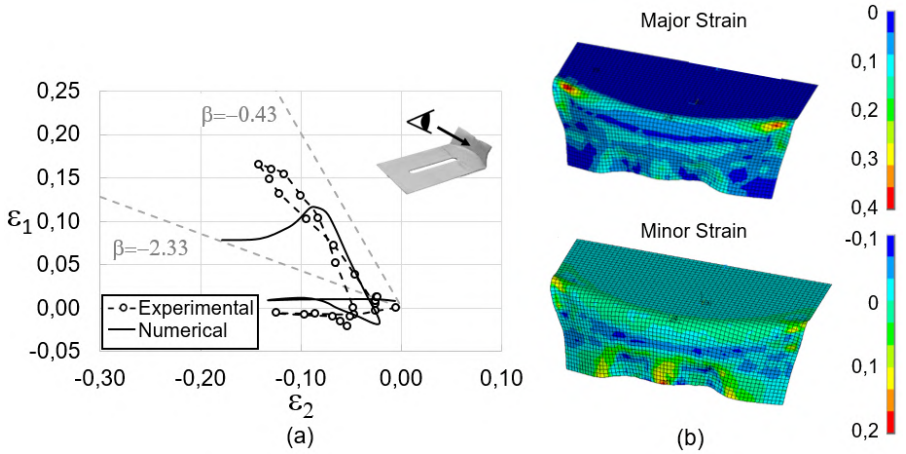

Figure 6.27. Validation of numerical modelling: (a) comparison of numerical vs. experimental principal strains in the central section of the flange and (b) numerical strain contours (the figures correspond to the failed case $\phi_{tool} = 12$ mm, $S = 20$ rpm, $R_{die} = 45$ mm, $l_0 = 15$ mm and $w_0 = 63$ mm).

Consequently, the experimental and numerical sections represented in the FLD only coincided in the region that was not affected by the wrinkles, as one wrinkle was measured from its concave surface and the other from its convex surface. However, although the strain distribution of the central sections did not agree completely, the number of wrinkles and their amplitude were reproduced successfully by the numerical model.

A similar validation was performed for the shrink flanging tests with $R_{die} = 20$ mm. In this regard, figure 6.28 and figure 6.29 present the numerical validations performed for the successful flange and the flange that failed by incipient wrinkling, respectively, consisting of the strain distribution within the FLD and the numerical major and minor strain contours. The numerical and experimental central sections are in good agreement in both tests with the exception of the end of the numerical section corresponding to the failed flange. As explained previously, this issue only affects the last 0.5 mm of the section. Regarding the strain distributions depicted in the principal strain contours, they are also in good agreement, showing the highest levels of major strain and the lower levels of minor strains in the centre and at the edge, respectively.

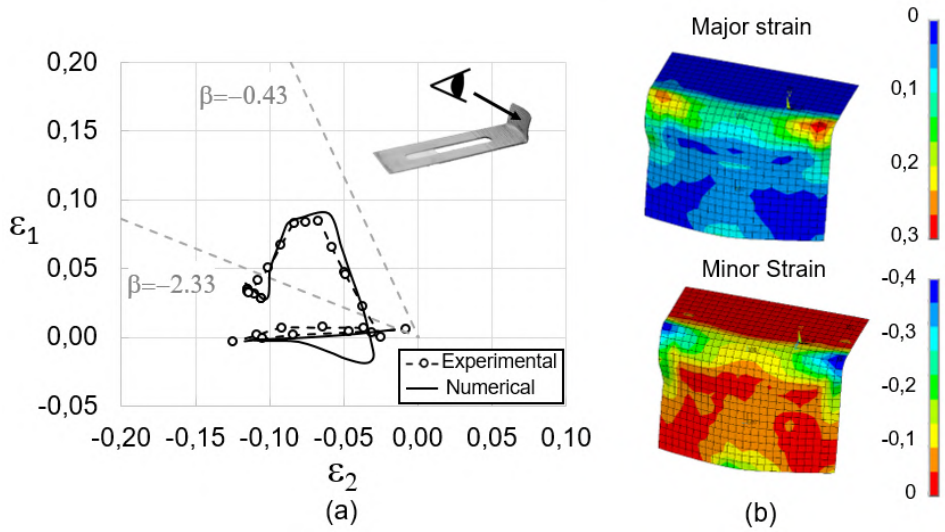

Figure 6.28. Validation of numerical modelling: (a) comparison of numerical vs. experimental principal strains in the central section of the flange and (b) numerical strain contours (the figures correspond to the successful case $\phi_{tool} = 12$ mm, $S = 20$ rpm, $R_{die} = 20$ mm, $l_0 = 15$ mm and $w_0 = 28$ mm).

In general, the numerical validation performed demonstrates that the FE model is able to reproduce the different modes of failure and the strain levels attained in shrink flanging by SPIF. In the case of flanges that failed by wrinkling, although the FE model did not reproduce the final shape of the wrinkles, it was able to predict the onset of the instability, the number of wrinkles and the order of magnitude of the principal strains.

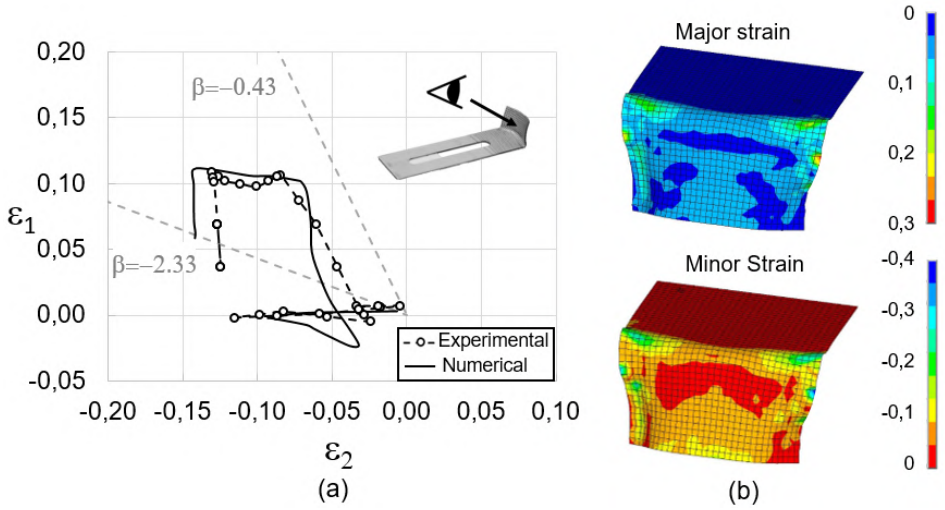

Figure 6.29. Validation of numerical modelling: (a) comparison of numerical vs. experimental principal strains in the central section of the flange and (b) numerical strain contours (the figures correspond to the failed case $\phi_{tool} = 12$ mm, $S = 20$ rpm, $R_{die} = 20$ mm, $l_0 = 15$ mm and $w_0 = 32$ mm).

6.2.4 Geometry analysis

This section analyses the flanges presented in section 6.2.3 to evaluate the springback in shrink flanging by SPIF. For each flange, two representative profiles will be analysed, comparing experimental and numerical results to assess the capability of the FE model to predict the shape of the flanges. These profiles are depicted in figure 6.30. The blue line and the red line correspond to the central section and the edge section of the flange, respectively.

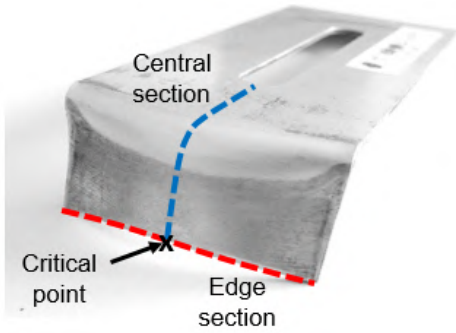

Figure 6.30. Central, lateral and edge sections on a $R_{die} = 45$ mm flange.

Focusing on the larger die radius, figure 6.31 and figure 6.32 present the central section and edge section for the successful flange S and the flange that failed by wrinkling F(W) corresponding to $R_{die} = 45$ mm. The profiles of the numerical and experimental sections represent the medium plane of the sheet, whereas the die profile represents the surface of the die.

As shown in figure 6.31, there is good agreement between the numerical and experimental results for both the central section and the edge section of the successful flange. In this flange, as a consequence of the springback, the wall is not completely parallel to the die profile, as seen in the central section presented in figure 6.31a. The effect of the elastic recovery can also be seen in the profile of the edge section (see figure 6.31b), where the final radius of the flange edge is slightly higher than 45 mm. As a consequence of the increased radius, the sides of the edge section are 5 mm from the die profile.

In the case of the flange that failed by wrinkling, three wrinkles can be observed in both the experimental and numerical edge sections presented in figure 6.32b. In this regard, although the FE model did not reproduce the final shape of the flange, the number of wrinkles and their amplitude were successfully predicted, as described in section 6.2.3.

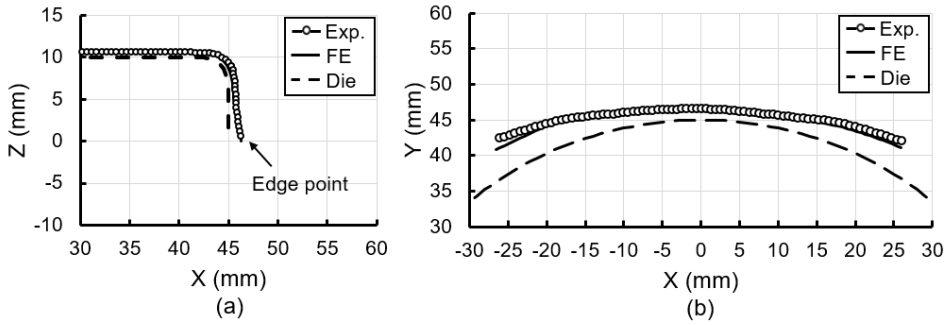

Figure 6.31. Profile analysis of a successful flange of $w_0 = 63$ mm and $l_0 = 10$ mm. a) Picture of the formed flange. b) Numerical and experimental edge profile.

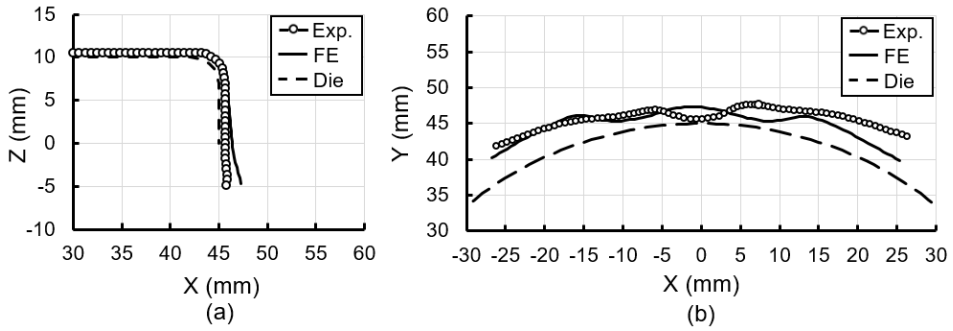

Figure 6.32. Profile analysis of a flange of $w_0 = 63$ mm and $l_0 = 10$ mm with wrinkles. a) Picture of the formed flange. b) Numerical and experimental edge profile.

Similarly, figures 6.33 and 6.34 depict the geometry analyses carried out for the successful flange and the flange that failed by incipient wrinkling for $R_{die} = 20$ mm. The FE model successfully reproduced the shape of both flanges. Indeed, it also predicted the shape of the flange that failed by incipient wrinkling, reproducing the springback and the polygonal shape that is characteristic of this mode of failure.

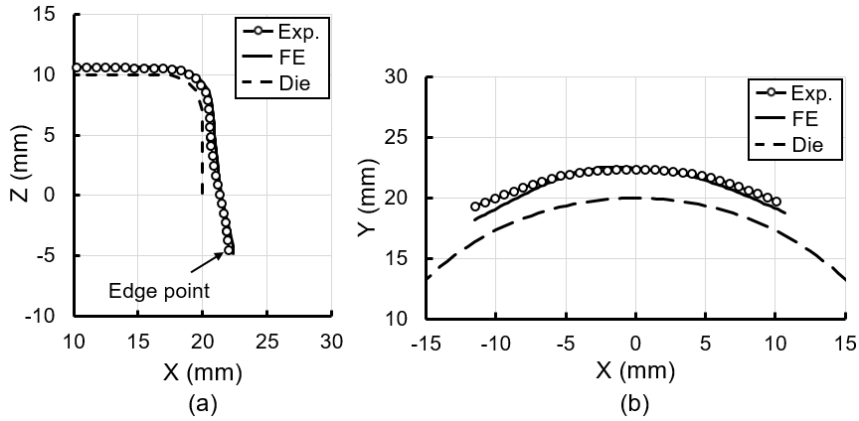

Figure 6.33. Central, lateral and edge sections on a $R_{die} = 45$ mm flange.

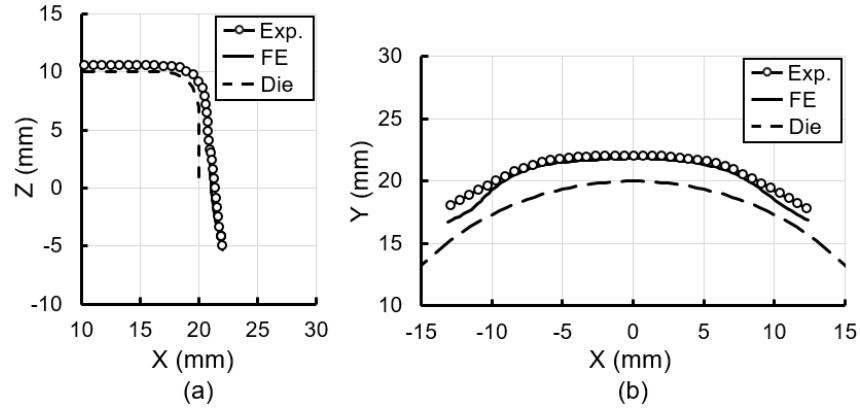

Figure 6.34. Central, lateral and edge sections on a $R_{die} = 45$ mm flange.

Based on these results, it can be affirmed that the influence of the springback effect should be considered in shrink flanging by SPIF. In this regard, the FE model has been shown to be effective in reproducing the final shape of successful flanges and the flanges that failed by incipient wrinkling, allowing estimation of the springback effect. Furthermore, although the model did not predict the shape of the wrinkles, it was demonstrated to be useful in predicting the onset of wrinkling.

6.2.5 Wrinkling prediction by stress analysis

According to the results presented in section 6.2.1, it is clear that wrinkling is the principal cause of failure in shrink flanging by SPIF. With the objective of predicting both the failure by wrinkling and that by incipient wrinkling, different approaches based on principal strains and FE analysis were proposed. In this regard, in section 6.2.2, it was demonstrated that the predictions based on the pure compression line are not entirely effective, as some successful flanges showed strain points beyond this line. Additionally, in section 6.2.4, the geometry analyses performed using FE modelling were shown to be effective in predicting the different modes of failure and the final geometry of the flanges. However, this method only addresses the final geometry of the simulations, not providing a deeper analysis of the conditions that lead to failure by wrinkling in shrink flanging by SPIF. In this context, a more physical approach based on evaluation of the compression and stress in the sheet is proposed in this section. This methodology focuses on analysis of the principal in-plane compression stress σ_2^{ip}, considering that wrinkling occurs when a critical stress level is reached.

To perform the stress analysis, the principal in-plane stresses σ_1^{ip} and σ_2^{ip} were evaluated at the critical point previously depicted in figure 6.30. As previously explained, this critical point is the most compressed point in successful and failed flanges, being the location where wrinkle onset is more likely to occur. The stress data were obtained using the FE model for shrink flanging validated in section 6.2.3.

Figure 6.35 depicts the evolution of the minor and major principal in-plane stresses σ_1^{ip} and σ_2^{ip} along the simulation corresponding to the FE model of the successful flange for $R_{die} = 45$ mm, highlighted in bold in table 6.3c. Note that the horizontal axis is the vertical displacement of the forming tool z_{tool}. The evolution of the compression stress σ_2^{ip} during the flanging process is cyclical, coinciding with each cycle with a different tool pass. In this regard, the compression stress σ_2^{ip} reaches a local minimum when the tool approaches the critical point, whereas it reaches a maximum when the tool is at the furthest point with respect to the critical point. The grey curve, which corresponds to σ_1^{ip}, also follows this cyclical pattern, reaching maxima and minima with every tool cycle. In addition, an envelope curve is presented, connecting the local minima in the compression stress σ_2^{ip}. The analysis carried out for the successful flange was also applied to the flange that failed by wrinkling F(W) highlighted in table 6.3c, as presented in figure 6.36. The instant corresponding to the numerical onset of wrinkling is represented with

the label z^{crit}.

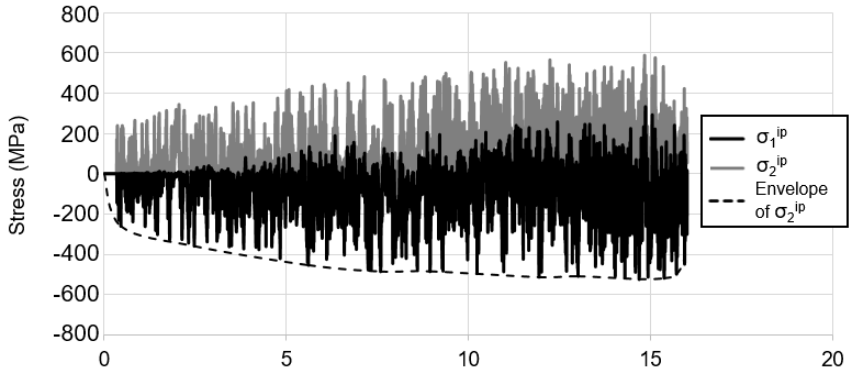

Figure 6.35. Evolution of principal in-plane stresses corresponding to the successful flange for $R_{die} = 45$ mm.

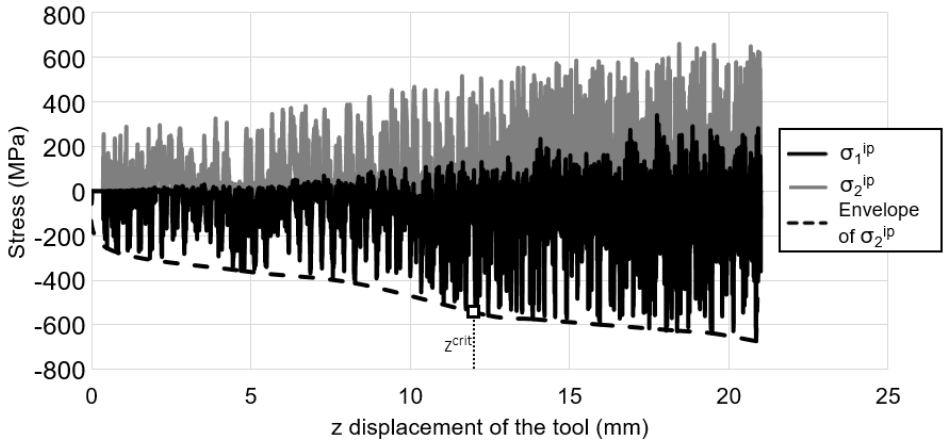

Figure 6.36. Evolution of principal in-plane stresses corresponding to the flange that failed by wrinkling for $R_{die} = 45$ mm.

The methodology followed to predict the onset of wrinkling is based on the analysis of the local minima in the compression strain σ_2^{ip}. In this regard, the evolutions of σ_2^{ip} for successful and failed flanges presented in figure 6.35 and figure 6.36 show different behaviours. For the failed flange, the local minima of σ_2^{ip} always decrease at a constant rate as the forming process proceeds. For this flange, the minimum value of σ_2^{ip} (-700 MPa) is attained at the end of the process.

In contrast, for the successful flange, the minimum value envelope of σ_2^{ip} decreases in the first half of the forming process but is almost constant in the second half of the simulation. For this flange, the lowest value of compression strain is reached at $z_{tool} = 15$ mm ($\sigma_2^{ip} = -525$ MPa). Comparing the stress results of both flanges, the minimum σ_2^{ip} obtained for the successful flange ($\sigma_2^{ip} \approx -525$ MPa) is higher than the minimum σ_2^{ip} for the failed flange ($\sigma_2^{ip} \approx -700$ MPa), with the critical point of the failed flange being more compressed than that of the successful flange. Furthermore, it can be seen that the value of the σ_2^{ip} envelope at $z_{tool} = z^{crit}$ ($\sigma_2^{ip} \approx -530$ MPa) is similar to the minimum σ_2^{ip} obtained in the analysis of the successful flange.

In this regard, it must be noted that these flanges represent the transition from a successful flange to a flange that failed by wrinkling, and therefore, the successful flange must be close to failure by wrinkling. The existence of a wrinkling limit at levels of σ_2^{ip} slightly near -530 MPa will be analysed in the following.

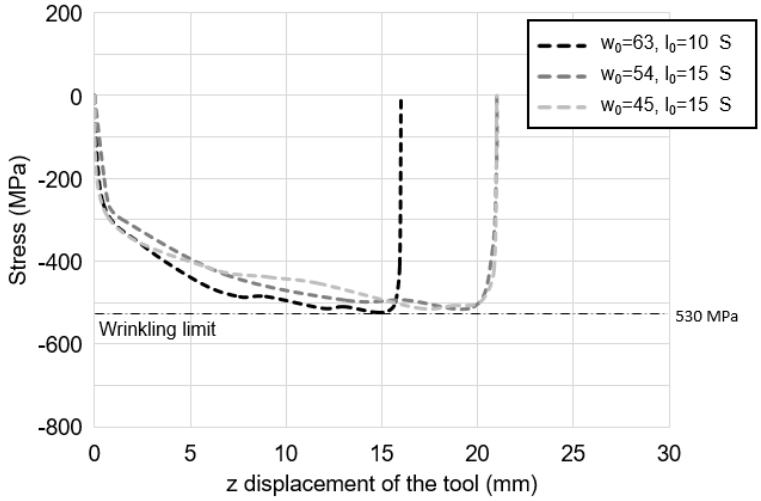

Figure 6.37. Evolution of the σ_2^{ip} envelope for three successful flanges corresponding to $R_{die} = 45$ mm.

With the aim of determining the wrinkling limit in terms of compression stress for the flanges corresponding to $R_{die} = 45$ mm, the evolutions of σ_2^{ip} of six flanges were analysed. In this case, to simplify the comparison of the different flanges, only the σ_2^{ip} envelopes of each test are included. Figures 6.37 and 6.38 show the σ_2^{ip} envelopes corresponding to three successful flanges and three failed flanges,

respectively. These flanges were selected from the set of flanges included in table 6.3c, which were processed using identical process parameters (tool diameter ϕ_{tool} and spindle speed S). The initial width and initial lengths corresponding to these flanges are shown in the figure legends.

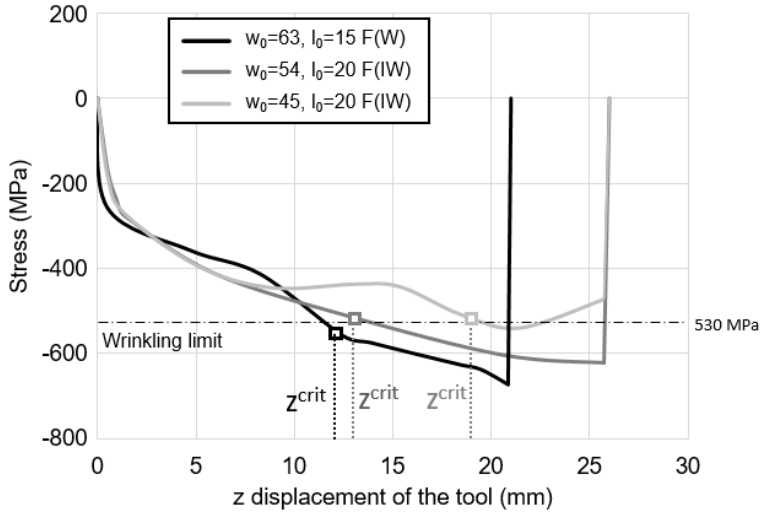

Figure 6.38. Evolution of the σ_2^{ip} envelope for three failed flanges corresponding to $R_{die} = 45$ mm.

As seen in figure 6.37, the evolution of σ_2^{ip} in the successful flanges presents a characteristic pattern with three stages consisting of (i) a first stage with decreasing σ_2^{ip}, (ii) a stabilization of the curve at constant σ_2^{ip} and (iii) an increase in σ_2^{ip} at the end of the test. In all cases, the minimum value of in-plane compression strain (having a value of $\sigma_2^{ip} \approx -525$ MPa) was reached in the second stage. Note that this value is very similar to those for the successful flanges analysed previously.

Figure 6.38 presents the σ_2^{ip} envelopes of the failed flanges. According to the trend of these curves, the σ_2^{ip} evolution of the flange that failed by wrinkling F(W) is always decreasing, and therefore, the minimum value of σ_2^{ip} is reached at the end of the tests. Two behaviours were observed for the flanges that failed by incipient wrinkling. On the one hand, the σ_2^{ip} evolution of the flange that failed by incipient wrinkling F(IW) with $w_0 = 54$ mm and the flange that failed by wrinkling F(W) with $w_0 = 63$ mm is always decreasing. Note that these flanges are close to each other in the process window (see table 6.3c). On the other hand, the σ_2^{ip} evolution of the failed flange with $w_0 = 45$ mm is similar to that of the successful flanges

presented in figure 6.37.

The onset of wrinkling obtained from the FE simulation is presented in the curves corresponding to the failed flanges. According to the levels of σ_2^{ip} at wrinkling, it can be seen that for both modes of failure, the values are very similar. In this regard, the average level of σ_2^{ip} at wrinkling is represented using a horizontal line at $\sigma_2^{ip} = -530$ MPa with the label "Wrinkling limit". This wrinkling limit, which is also presented in figure 6.37, is slightly below the minimum levels of σ_2^{ip} obtained for the successful shrink flanges, showing the relation between the minimum compression strains attained in shrink flanging by SPIF and the onset of wrinkling.

The results presented above show that for the die radius analysed and the process parameters selected, wrinkling occurs at similar values of compression strains σ_2^{ip} in shrink flanging by SPIF. This allows a quantitative wrinkling limit to be defined based on the maximum compression stress in the flange during the forming process.

Chapter 7

Conclusions

This chapter covers the main conclusions of the thesis and proposes possible further works that may result from this investigation.

7.1 General conclusions

This thesis presents a systematic study with the aim of increasing the knowledge of stretch and shrink flanging by single point incremental forming (SPIF) of AA2024-T3 sheets. With this aim, an experimental campaign was performed considering large (R_{die} = 45 mm) and small (R_{die} = 20 mm) principal flange radii, assessing the formability limits within a wide range of process parameters. In addition, FE modelling was used to study the principal modes of failure, performing formability predictions regarding the two flange geometries analysed, i.e., stretch and shrink.

The 2024-T3 sheet material was characterized by means of tensile tests, determining the tensile properties in different directions and the corresponding Lankford anisotropy coefficients r_0, r_{90} and r_{45}. Additionally, the conventional formability limits within the FLD were obtained, which were, for this sheet material in particular, uniquely expressed by the FFL, as the material did not present necking.

The experimental campaign was performed considering a wide range of process parameters, thus allowing the process windows for stretch and shrink flanging by SPIF to be obtained. The parameters analysed include the flange length (l_0), flange width (w_0), flange principal radius (R_{die}), tool diameter (ϕ_{tool}) and spindle speed (S). In this regard, the principal modes of failure were determined for both flange geometries, consisting of (i) either fracture at the corner F(C) or fracture

at the edge F(E) in the case of stretch flanges and (ii) failure by wrinkling F(W) or failure by incipient wrinkling F(IW) in the case of shrink flanges.

An explicit FE model based on the Barlat 89 yield criterion was used to reproduce a number of flanging tests for fixed values of ϕ_{tool} and S. The obtained results allow an understanding of the process conditions involved in the transition from a successful flange to a failed flange for different failure modes. Additionally, two novel approaches were proposed to assess the formability in flanging by SPIF, consisting of (i) analysis of the stress triaxiality in stretch flanging and (ii) assessment of the level of compression stresses in shrink flanging.

Presenting the general conclusions of this study, the particular conclusions for each flange geometry will be summarized individually.

Stretch flanges

From the stretch flanging analysis, the following particular conclusions are drawn:

As a result of the experimental campaign performed for stretch flanging by SPIF, two different modes of failure were observed. On the one hand, failure by fracture at the corner F(C) was attained in flanges of high initial length l_0 and medium to moderate initial width w_0. On the other hand, failure by fracture at the edge F(E) was observed in wide flanges with low to moderate initial lengths. It was also found that narrow flanges produced successful flanges independent of their initial length.

Regarding the effects of the process parameters analysed, a lower tool diameter increased the formability of flanges for $R_{die} = 45$ mm, whereas it had the opposite effect on flanges for $R_{die} = 20$ mm, not providing a clear effect on the material formability. In addition, increasing the spindle speed from $S = 20$ rpm to $S = 1000$ rpm increased the formability only in the tests performed using the lower tool diameter $\phi_{tool} = 12$ mm, and it did not have any effect on the flanges processed using the larger tool diameter $\phi_{tool} = 20$ mm.

A set of flanges corresponding to $\phi_{tool} = 20$ mm and $S = 20$ rpm were selected to analyse the strain levels attained in the transition from a successful flange to a flange that failed by fracture at the edge. For both die radii, the strain levels of the failed flanges were higher than the strain levels observed in the successful flanges. In these analyses, the successful flanges corresponding to $R_{die} = 45$ mm and the failed flanges for both die radii presented strains above the FFL of the material

at points outside of the fracture region. According to these results, it can be concluded that the stretch flanging process by SPIF may produce an enhancement of formability beyond the conventional limit represented by the FFL in materials without necking.

A numerical and analytical framework was established to assess the formability in the stress triaxiality space based on the Barlat 89 anisotropy yield criterion for the first time. In this regard, the material FFL was transformed from the principal strain space to the average stress triaxiality $\bar{\eta}$ versus equivalent strain $\bar{\varepsilon}$ space using the corresponding expressions obtained from the Barlat 89 yield criterion. Additionally, the FFL curves in the $\bar{\eta}$-$\bar{\varepsilon}$ space corresponding to the von Mises isotropic yield criterion and Hill 48 yield criterion were compared with the Barlat FFL, showing the importance of selecting an appropriate yield criterion.

The evolutions of the critical points corresponding to successful and failed flanges for both die radii were analysed in the $\bar{\eta}$-$\bar{\varepsilon}$ space. The results demonstrated that these evolutions occur in a region of the $\bar{\eta}$-$\bar{\varepsilon}$ space that is different from the location of the FFL obtained for proportional loading. These results suggest that a failure criterion based only on the FFL obtained using Nakazima tests is not suitable for assessing the onset of failure in stretch forming by SPIF. Consequently, a new approach based on iso-damage curves derived from the Atkins interpretation of the McClintock damage model was proposed to assess the formability in stretch flanging by SPIF.

Shrink flanges

As a result of the shrink flanging campaign, the following particular conclusions are drawn:

In the experimental campaign performed for shrink flanging by SPIF, two modes of failure were obtained: (i) failure by wrinkling F(W) and (ii) failure by incipient wrinkling. On the one hand, failure by wrinkling is attained when the flanges present well-established wrinkles. This mode of failure was observed only in flanges of large initial width for $R_{die} = 45$ mm. On the other hand, failure by incipient wrinkling was considered when the flanges presented shape deviations but not larger wrinkles. This mode of failure was found in flanges for $R_{die} = 45$ mm and in flanges for $R_{die} = 20$ mm.

The influence of the different process parameters on the formability was analysed. In this regard, reducing the tool diameter from 20 mm to 12 mm increased

the formability for $R_{die} = 45$ mm flanges, whereas it did not present any effect on the process windows corresponding to $R_{die} = 20$ mm. With respect to the spindle speed S, the variation from S=20 rpm to S=1000 rpm produced no effects in terms of formability for any of the die radii analysed.

To study the conditions in the transition from a successful flange to a failed flange in the process windows, a set of flanges were analysed in terms of principal strains for both die radii and constant process parameters $\phi_{tool} = 12$ mm and $S = 20$ rpm. From these analyses, it was concluded that, in general, failed flanges present principal strains below the pure compression line of the material, assuming that the Barlat 89 yield criterion corresponds to $\beta = -2.33$. Furthermore, in the analyses of the successful $R_{die} = 20$ mm flanges, there were a number of strain points below this limit, showing an increase in formability with respect to this line. These results suggest that assuming the pure compression line as a wrinkling limit is not completely effective in the prediction of wrinkling in shrink flanging by SPIF.

Furthermore, a geometry analysis of the flanges in the transition zone from the successful to failure zone was carried out. The experimental results confirmed that the springback effect is present in flanges for both die radii and should therefore be considered in the manufacturing of flanges using SPIF. Additionally, the shape of the flanges was compared to the results obtained using FE modelling, showing good agreement in the geometry predictions and demonstrating the capacity of the FE model to predict the different modes of failure. In the case of the flange that failed by wrinkling, the FE model predicted the onset of the wrinkles, whereas in the case of the flange that failed by incipient wrinkling, the characteristic polygonal shape of this mode of failure was successfully reproduced.

Finally, an engineering approach to the prediction of wrinkling in shrink flanging by SPIF based on evaluation of the compression stress was proposed. This method focuses on the level of the in-plane minor stress σ_2^{ip}, suggesting that wrinkling occurs when the compression stress reaches a critical value of σ_2^{ip}. This critical value was determined for the flanges corresponding to $R_{die} = 45$ mm.

7.2 Future works

This section presents possible future investigations that could be performed to continue this research, with some of them currently being carried out already:

In this study, the flanges were obtained from rectangular specimens. Further

works will focus on optimizing the pre-cut shape to obtain flanges with straight edges using the experimental results and the numerical tools developed in this thesis.

The analyses performed on stretch and shrink flanges focused on flanges of small and medium principal radii. In this regard, future work could be performed on a different range of large die radii (e.g., R_{die} larger than 100 mm) used for large structures and other industrial applications.

The AA2024-T3 sheet is a low ductility material that fails directly by fracture, with the formability limited by the FFL in the principal strain diagram. In this regard, similar studies could be performed for a more ductile aluminium sheet that fractures by necking and for polymeric sheets.

The analyses of principal strains within the FLD showed strains beyond the conventional forming limits represented by the FFL in stretch flanging as well as strains below the pure compression line in shrink flanging. To assess the increase in formability obtained in SPIF versus the formability in a single-stage flanging process, conventional flanging experiments using a punch and a die need to be carried out. This approach would allow us to compare the conventional and incremental flanging processes.

Bibliography

AISI (1988) Automotive Steel Design Manual

Allwood J, King G, Duflou J (2005) A structured search for applications of the incremental sheet-forming process by product segmentation. Proceedings of the Institution of Mechanical Engineers Part B: Journal of Engineering Manufacture 219(2):239–244

Allwood J, Braun D, Music O (2010) The effect of partially cut-out blanks on geometric accuracy in incremental sheet forming. Journal of Materials Processing Technology 210(11):1501–1510

Allwood JM, Shouler DR (2007) Paddle forming: a novel class of sheet metal forming processes. Annals of the CIRP 56/1/2007:257–260

Altan T, Tekkaya AE (2012) Sheet metal forming. ASM International

Ambrogio G, Costantino I, De Napoli L, Filice L, Frantini L, Muzzupappa M (2004) Influence of some relevant process parameters on the dimensional accuracy in incremental forming: a numerical and experimental investigation. Journal of Materials Processing Technology 153-154:501–507

Ambrogio G, Cozza V, Filice L, Micari F (2007) An analytical model for improving precision in single point incremental forming. Journal of Materials Processing Technology 191(1-3):92–95

Ambrogio G, Gagliardi F, Filice L (2013) Robust design of incremental sheet forming by taguchi's method. Procedia CIRP 12:270–275

Ansys (2018) ANSYS/LS-DYNA V19.1 User's Guide and Documentation. Ansys

Asnafi N (1999) On stretch and shrink flanging of sheet aluminium by fluid forming. Journal of Materials Processing Technology 96:198–214

ASTM (2000) Standard E 517 – 00. Standard method for plastic strain ratio r for sheet metal

ASTM (2009) Standard E8/E8M – 09. Standard tests methods for tension testing of metallic materials

Atkins A (1996) Fracture in forming. Journal of Materials Processing Technology 56:609–618

Attanasio, Ceretti E, Giardini C (2006) Optimization of tool path in two points incremental forming. Journal of Materials Processing Technology 177:409–412

Attanasio, Ceretti E, Giardini C, Mazzoni L (2008) Asymmetric two points incremental forming: Improving surface quality and geometric accuracy by tool path optimization. Journal of Materials Processing Technology 197:59–67

Ayada M, Higashino T, Mori K (1987) Central bursting in extrusion of inhomogeneous materials. ICTP 1987 – Proceedings of the 2nd International Conference on Technology of Plasticity 1:553–558

Bambach M, Hirt G, Junk S (2003) Modeling and experimental evaluation of the incremental cnc sheet metal forming process. VII Int Conf on Computational Plasticity pp 1–15

Bambach M, Taleb AB, Hirt G (2009) Strategies to improve the geometric accuracy in asymmetric single point incremental forming. Production Engineering 3:145–156

Bambach M, Voswinckel H, Hirt G (2014) A new process design for performing hole-flanging operations by incremental sheet forming. Procedia Engineering 81(C):2305–2310

Banabic D (2010) Sheet metal forming processes. Constitutive modelling and numerical simulation. Springer

Bao Y, Wierzbicki T (2004) On fracture locus in the equivalent strain and stress triaxiality space. International Journal of Mechanical Sciences 46:81–98

Barlat F, Lian J (1989) Plastic behaviour and stretchability of sheet metals. part i: A yield function for orthotropic sheets under plane stress conditions. Int Journal of Plasticity 5:51–66

Barlat F, Richmond O (1987) Prediction of tricomponent plane stress yield surfaces and associated flow and failure behaviour of strongly textured fcc polycrystalline sheets. Materials Science and Engineering 91:15–29

Belytschko L, Moran (2000) Nonlinear finite elements for continua and structures. Wiley

Borrego M, Morales-Palma D, Martínez-Donaire A, Centeno G, Vallellano C (2016) Experimental study of hole-flanging by single-stage incremental sheet forming. Journal of Material Processing Technology 237:320–330

Brosius A, Yin Q, Güner A, Tekkaya A (2011) A new shear test for sheet metal characterization. Steel research int 82:4:323–328

Callegari M, Amodio D, Ceretti E, Giardini C (2006) Sheet incremental forming: Advantages of robotised cells vs. cnc machines. Simulation

Cao T, Lu B, Ou H, Long H, Chen J (2016) Investigation on a new hole-flanging approach by incremental sheet forming through a featured tool. International Journal of Machine Tools and Manufacture 110:1–17

Centeno G, Doblas F, Martínez-Palmeth L, Martínez-Donaire A, Vallellano C (2012a) Fea of the bending effect in the formability of metal sheets via incremental forming. Steel Research International Spl. Issue Metal Forming:447–450

Centeno G, Silva M, Cristino V, Vallellano C, Martins P (2012b) Hole-flanging by incremental sheet forming. International Journal of Machine Tools and Manufacture 59:46–54

Centeno G, Bagudanch I, Martínez-Donaire A, Garcia-Romeu M, Vallellano C (2014) Critical analysis of necking and fracture limit strains and forming forces in single point incremental forming. International Journal of Mechanical Sciences 63:20–29

Centeno G, Martínez-Donaire Andrés J, Bagudanch I, Morales-Palma D, Garcia-Romeu ML, Vallellano C (2017) Revisiting formability and failure of aisi304 sheets in spif: Experimental approach and numerical validation. Metals 7:531

Chen L (2011) Numerical simulation and die compensation on springback of shrink flanging in rubber forming. Third International Conference on Measuring Technology and Mechatronics Automation 2:705–708

Chen L, Yingwei L, Shanliang L (2010) Finite element simulation and control method on springback of stretch flanging in rubber forming. International Conference on Digital Manufacturing and Automation 2010

Chen L, Chen H, Wang Q, Li Z (2015a) Studies on wrinkling and control method in rubber forming using aluminium sheet shrink flanging process. Materials and Design 65:505–510

Chen L, Chen H, Wang Q, Li Z (2015b) Studies on wrinkling and control method in rubber forming using aluminium sheet shrink flanging process. Materials and Design 65:505–510

Cristino V, Montanari L, Silva M, Atkins A, Martins P (2014) Fracture in hole-flanging produced by single point incremental forming. Int Journal of Mechanical Sciences 83:146–154

Cui Z, Gao L (2010) Studies on hole-flanging process using multistage incremental forming. CIRP Journal of Manufacturing Science and Technology 2:124–128

Dewang Y, Hora MS, Panthi SK (2014a) Analysis of stretch flanging process using fem to study deformation behavior of flange. ICEMP 2014:247–252

Dewang Y, Hora MS, Panthi SK (2014b) Finite element analysis of non-axisymmetric stretch flanging process for prediction of location of failure. Procedia materials science International conference on advances in manufacturing and materials engineering 5:2054–2062

Dewang Y, Hora MS, Panthi SK (2014c) Review on finite element analysis of sheet metal stretch flanging process. ARPN Journal of Engineering and Applied Sciences 9(9):1565–1579

Dewang Y, Hora MS, Panthi SK (2017) Effect of process parameters on deformation behavior of aa 5052 sheets in stretch flanging process. Materials Today: Proceedings 4:9316–9326

Dudra S, Shan S (1988) Stretch flanges: Formability and trimline development. J Mater Shamping Technol 6:91–101

Duflou J, Lauwers B, Verbert J (2007a) Study on the achievable accuracy in single point incremental forming. Advanced Methods in Material Forming p 251–262

Duflou J, Tunckol Y, Szekeres A, Vanherck P (2007b) Experimental study on force measurements for single point incremental forming. Journal of Materials Processing Technology 189:65–72

Durante M, Formisano A, Langella A (2011) Observations on the influence of tool-sheet contact conditions on an incremental forming process. Journal of Materials Engineering and Performance 20/6:941–946

Embury J, Duncan J (1981) Formability maps. Annual Review of Materials Science 11:505–521

Emmens W, Van den Boogaard A (2008) Tensile tests with bending: a mechanism for incremental forming. Int J Mater Form Suppl 1:1155–1158

Emmens W, Van den Boogaard A (2009) An overview of stabilizing deformation mechanisms in incremental sheet forming. Journal of material processing technology 209:3688–3695

Emmens WC (2011) Formability. A review of parameters and processes that control, limit or enhance the formability of sheet metal. Springer

Fan G, Sun F, Meng X, Gao L, Tong G (2009) Electric hot incremental forming of ti-6al-4v titanium sheet. The International Journal of Advanced Manufacturing Technology 49:941–947

Fang Y, Lu B, Chen J, Xu D, Ou H (2014) Analytical and experimental investigations on deformation mechanism and fracture behavior in single point incremental forming. Journal of Materials Processing Technology 214:1503–1515

Filice L, Fantini L, Micari F (2002) Analysis of material formability in incremental forming. Annals of the CIRP 51/1/2002:199–202

Fiorentino A, Ceretti E, Attanasio A, Mazzoni L, Giardini C (2009) Analysis of forces, accuracy and formability in positive die sheet incremental forming. International Journal of Material Forming 2:805–808

Franzen V, Kwiatkowski L, Martins P, Tekkaya (2009) Single point incremental forming of pvc. Journal of Materials Processing Technology 209:462–469

Goodwin G (1968) Application of strain analysis to sheet metal forming problems in the press shop. SAE paper 680093

Guzmán C, Gu J, Duflou J, Vanhove H, Flores P, Habraken A (2012) Study of the geometrical inaccuracy on a spif two-slope pyramid by finite element simulations. International Journal of Solids and Structures 49:3594–3604

Hagan E, Jeswiet J (2003) A review of conventional and modern single-point sheet metal forming methods. Proceedings of the Institution of Mechanical Engineers, Part B: Journal of Engineering Manufacture 217(2):213–225

Ham M, Jeswiet J (2008) Dimensional accuracy of single point incremental forming. Journal of Material Forming pp 1171–1174

Han F, Mo J, Qi H, Long R, Cui X, Li Z (2013) Springback prediction for incremental sheet forming based on fem-psonn technology. Transactions of Nonferrous Metals Society of China 23:1061–1071

Hill R (1948) A theory of the yielding and plastic flow of anisotropic metals. Proceedings of the Royal Society London 193:281–297

Hirt G, Ames J, Bambach M, Kopp R (2004) Forming strategies and process modelling for cnc incremental sheet forming. Annals of CIRP 53/1/2004:203

Husmann T, Magnus C (2016) Thermography in incremental forming processes at elevated temperatures. Measurement 77:16–28

Iseki H, Kato K, Sakamoto S (1993) Forming limit of flexible and incremental sheet metal bulging with a spherical roller. Proceedings 4th ICTP, Beijing, China, September 5–9 pp 1635–1640

Isik K, Silva M, Tekkaya A, Martins P (2014) Formability limits by fracture in sheet metal forming. Journal of Materials Processing Technology 214:1557–1565

ISO IS (2008) ISO 12004-2:2008 Metallic materials-sheet and strip determination of forming limit curves, Part 2: Determination of forming limit curves in the laboratory

Jackson K, Allwood J (2009) The mechanics of incremental sheet forming. Journal of Materials Processing Technology 209:1158–1174

Jackson K, Allwood J, Landert M (2008) Incremental forming of sandwich panels. Journal of Materials Processing Technology 204/1–3:290–303

Jeswiet J (2004) Recent results for spif. Seminar on Incremental Forming

Jeswiet J, Hagan E (2002) Rapid proto-typing of a headlight with sheet metal. Transactions of North American Manufacturing Research Institute 30:33–38

Jeswiet J, Micari F, Hirt G, Bramley A, Duflou J, Allwood J (2005) Asymmetric single point incremental forming of sheet metal. CIRP Annals - Manufacturing Technology 54(2):88–114

Jong-Jin P, Yung-Ho K (2003) Fundamental studies on the incremental sheet metal forming technique. Journal of Materials Processing Technology 140:447–453

Kalpakjian S, Schmid SR (2009) Manufacturing engineering and technology. Pearson

Keeler S, Backofen W (1963) Plastic instability and fracture in sheets stretched over rigid punches. Trans ASM 56:25–48

Kitazawa K (1997) Limit strains for cnc incremental stretch-expanding of aluminum sheets. J of Japan Institute of Light Metals 47:445–450

Kitazawa K, Nakane M (1997) Hemi-ellipsoidal stretch expanding of aluminum sheet by cnc incremental forming process with two path method. J of Japan Institute of Light Metals 47:440–445

Kitazawa K, Wakabayashi A, Murata K, Yaejima K (1996) Metal flow phenomena in computerized numerically controlled incremental stretch-expanding of aluminum sheets. J of Japan Institute of Light Metals 46:65–70

Kopac J, Kampus Z (2005) Incremental sheet metal forming on cnc milling machinetool. Journal of Materials Processing Technology 162-163:622–628

Le V, Ghiotti A, Lucchetta G (2008) Preliminary studies on single point incremental forming for thermoplastic materials. International Journal of Material Forming 1/1:1179–1182

Lege D, Barlat F, Brem J (1964) Characterization and modeling of the mechanical behavior and formability of a 2008-t4 sheet sample. International Journal of Mechanical Sciences 31:549

Leszak E (1967) Apparatus and process for incremental dieless forming

Li Y, Lu H, Daniel W, Meehan P (2015) Investigation and optimization of deformation energy and geometric accuracy in the incremental sheet forming process using response surface methodology. International Journal of Advanced Manufacturing Technology 79:2041–2055

Logan R, Hosford W (1980) Upper-bound anisotropic yield locus calculations assuming (111) – pencil glide. International Journal of Mechanical Sciences 22:419–430

López-Fernández J, Centeno G, Martínez-Donaire Andrés J, Morales-Palma D, Vallellano C (2019) Critical evaluation of the formability of aa2024-t3 sheet deformed by single-point incremental forming. DYNA - Ingeniería e Industria 94(5):523–529

López-Fernández J, Centeno G, Martínez-Donaire A, Morales-Palma D, Vallellano C (2021) Stretch-flanging of aa2024-t3 sheet by single-stage spif. Thin-Walled Structures 160:107,338

Lu B, Fang Y, Xu D, Chen J, Ou H, Moser N, Cao J (2014) Mechanism investigation of friction-related effects in single point incremental forming using a developed oblique roller-ball tool. International Journal of Machine Tools & Manufacture 85:14–29

Lu B, Ou H, Shi S, Long H, Chen J (2016) Titanium based cranial reconstruction using incremental sheet forming. International Journal of Material Forming 9:361–370

Madeira T, Silva C, Silva M, Martins P (2015) Failure in single point incremental forming. International Journal of Advanced Manufacturing Technology 80:1471–1479

Magrinho M, Silva G, Centeno G, Moedas F, Vallellano C, MArtins P (2019) On the determination of forming limits in thin-walled tubes. International Journas of Mechanical Sciences 155:381–391

Maki T (2006) Dieless forming. Intern seminar on novel sheet metal forming technologies Feb. 15-16

Malhotra R, Reddy N, Cao J (2010) Automatic 3d spiral toolpath generation for single point incremental forming. Journal of Manufacturing Science and Engineering 132(6):06100,301–06100,310

Malhotra R, Xue L, Belytschko T, Cao J (2012) Mechanics of fracture in single point incremental forming. Journal of Materials Processing Technology 212:1573–1590

Marques Ta, Silva M, Martins PaF (2012) On the potential of single point incremental forming of sheet polymer parts. The International Journal of Advanced Manufacturing Technology 60:75–86

Martins P, Bay N, Skjoedt M, Silva M (2008) Theory of single point incremental forming. CIRP Annals - Manufacturing Technology 57:247–252

Martins P, Kwiatkowski L, Franzen V, Tekkaya A, Kleiner M (2009) Single point incremental forming of polymers. CIRP Annals – Manufacturing Technology 58/1::229–232

Martins P, Bay N, Tekkaya A, Atkins A (2014) Characterization of fracture loci in metal forming. International Journal of Mechanical Sciences 83:112–123

Martínez-Donaire A, García-Lomas F, Vallellano C (2014) New approaches to detect the onset of localised necking in sheets under through-thickness strain gradients. Materials and Design 57:135–145

Martínez-Donaire A, Borrego M, Centeno G, Vallellano C (2019) Analysis of the influence of stress triaxiality on formability of hole-flanging by single-stage spif. International Journal of Mechanical Sciences 151:76–84

Matsubara (1994) Incremental Backward Bulge Forming of a Sheet Metal with a Hemispherical Tool. J of the JSTP 35(1):1311–1316

McAnulty T, Jeswiet K, Doolan M (2016) Formability in single point incremental forming: A comparative analysis of the state of the art. CIRP Journal of Manufacturing Science and Technology pp 43–54

McClintock FA (1968) A criterion for ductile fracture by the growth of holes. Journal of Applied Mechanics 35:363–371

Micari F, Ambrogio G, Filice L (2007) Shape and dimensional accuracy in single point incremental forming: State of the art and future trends. Journal of Materials Processing Technology 191(1-3):390–395

Mirnia M, Shamsari M (2017) Numerical prediction of failure in single point incremental forming using a phenomenological ductile fracture criterion. Journal of Materials Processing Technology 244 (8):17–43

Mises R (1913) Mechanics of solids in plastic state. Göttinger Nachrichten Mathematical Physics 4:582–592

Mises R (1928) Mechanics of plastic deformation of crystals. Zeitschrift für Angewandte Mathematik und Mechanik 8:161–185

Montanari L, Cristino V, Silva M, Martins P (2013) A new approach for deformation history of material elements in hole-flanging produced by single point incremental forming. International Journal of Advanced Manufacturing Technology 69(5-8):1175–1183

Morales D, Martínez A, Vallellano C, Garcia-Lomas F (2009) Bending effect in the failure of stretch-bend metal sheets. International Journal of Material Forming 2:813–816

Morales-Palma D, Vallellano C, Garcia-Lomas FJ (2013) Assessment of the effect of the through-thickness strain/stress gradient on the formability of stretch-bend metal sheets. Materials and design 50:798–809

Morales-Palma D, Borrego M, Martínez-Donaire AJ, Centeno G, Vallellano C (2018) Optimization of hole-flanging by single point incremental forming in two stages. Materials 11,2029:1–15

Obikawa T, Satou S, Hakutani T (2009) Dieless incremental micro-forming of miniature shell objects of aluminum foils. International Journal of Machine Tools and Manufacture 49/12–13:906–915

Park J, Kim Y (2003) Fundamental studies on the incremental sheet metal forming technique. Journal of Materials Processing Technology 140:447–453

Pearce R (1968) Some aspects of anisotropic plasticity in sheet metals. International Journal of Mechanical Sciences 10:995–1001

Pereira Bastos RN, Alves de Sousa RJ, Fernandes Ferreira JA (2016) Enhancing time efficiency on single point incremental forming processes. International Journal of Material Forming 9:653–662

Pohland K, Raghupathi RS, Saniter JD, Schey JA, Weinmann KJ, Widera G (1985) Hanbook of metal forming. SME Dearborn Michigan USA

Powel NN (1990) Incremental sheet metal forming: flanged components. Proceedings of 28th MATADOR Conference, UMIST pp 359–366

Powell N, Andrew C (1992) Incremental Forming of Flanged Sheet Metal Components Without Dedicated Dies. Proceedings of the Institution of Mechanical Engineers, Part B: Journal of Engineering Manufacture 206(1):41–47

Rice J, Tracey D (1969) On the ductile enlargement of voids in triaxial stress fields. Journal of the Mechanics and Physics of Solids 17:201–217

Sawada T (1999) Deformation analysis for stretch forming of sheet metal with cnc machine tools. Proceedings of the 6th ICTP, Advanced Technology of Plasticity

Shankar R, Jadhav S, Goebel W Rand Homberg, Kleiner M (2005) Incremental sheet metal forming of preformed sheets. Proceedings of the ICTP 2005, Verona, Italy

Shim M, Park J (2001) The formability of aluminum sheet in incremental forming. Journal of Materials Processing Technology 113/1–3:654–658

Silva M, Martins P (2013a) Two-point incremental forming with partial die: Theory and experimentation. Journal of Materials Engineering and Performance 22:1018–1027

Silva M, Alves L, Martins PaF (2010) Single point incremental forming of pvc: Experimental findings and theoretical interpretation. European Journal of Mechanics - A/Solids 29:557–566

Silva M, Teixeira P, Reis A, Martins P (2013b) On the formability of hole-flanging by incremental sheet forming. Proceedings of the Institution of Mechanical Engineers, Part L: Journal of Materials: Design and Applications 227(2):91–99

Silva MB, Skjoedt M, Atkins AG, Bay N, Martins PAF (2008) Single-point incremental forming and formability/failure diagrams. J Strain Analysis 43:15–36

Silva MB, Skjoedt M, Bay N, Martins PAF (2009) Revisiting single-point incremental forming and formability/failure diagrams by means of finite elements and experimentation. J Strain Analysis 44:221–234

Silva MB, Nielsen PS, Bay N, Martins PAF (2011) Failure mechanisms in single-point incremental forming of metals. The International Journal of Advanced Manufacturing Technology 56:893–903

Skjoedt M, Hancock MH, Bay N (2007) Creating helical tool paths for single point incremental forming. Key Engineering Materials 344:583–590

Smith D (2009) Die Design Handbook. SME, Dearborn, Michigan, USA

Soeiro J, Silva C, Silva M, Martins P (2015) Revisiting the formability limits by fracture in sheet metal forming. Journal of Materials Processing Technology 217:184–192

Takano H, Kitazawa K, Goto T (2008) Incremental forming of nonuniform sheet metal: Possibility of cold recycling process of sheet metal waste. International Journal of Machine Tools and Manufacture 48:477–482

Tresca H (1964) On the yield of solids at high pressures. Comptes Rendus Academie des Sciences 59:754

Vallellano C, Morales D, García-Lomas FJ (2008) A study to predict failure in biaxially stretched sheets of aluminum alloy 2024-t3. Materials and Manufacturing Processes 23:3:303–310

Venkatesh V, Goh T (1986) A note on mathematical models of cup drawing by the guerin and marform processes. Journal of Mechanical Working Technology 13(3):273–278

Verbert J, Belkassem B, Henrard C, Habraken aM, Gu J, Sol H, Lauwers B, Duflou J (2008) Multi-step toolpath approach to overcome forming limitations in single point incremental forming. International Journal of Material Forming 1:1203–1206

Voswinckel H, Bambach M, Hirt G (2013) Process limits of stretch and shrink flanging by incremental sheet metal forming. Key Engineering Materials 549:45–52

Voswinckel H, Bambach M, Hirt G (2014) Improving geometrical accuracy for flanging by incremental sheet metal forming. International Journal of Material Forming 8:391–399

Wang H, Duncan S (2011) Optimization of tool trajectory for incremental sheet forming using closed loop control. Automation Science and Engineering (CASE) 2011 IEEE Conference:779–784

Wang NM, Wenner ML (1974) An analytical and experimental study of stretch flanging. Int Journal of Mechanical Sciences 16:135–143

Wang X, Cao J, Li M (2001) Wrinkling analysis in shrink flanging. ASME J Manuf Sci Eng 223(3):426–432

Wierzbicki T, Bao Y, Lee YW, Bai Y (2005) Calibration and evaluation of seven fracture models. International Journal of Mechanical Sciences 47:719–743

Wong CC, Dean TA, Lin J (2003) A review of spinning, shear forming and flow forming processes. International Journal of Machine Tools and Manufacture 43(14):1419–1435

Woodthrope J, Pearce R (1970) The anomalous behaviour of aluminium sheet under balanced biaxial tension. International Journal of Mechanical Sciences 12:341–347

Young D, Jeswiet J (2004) Wall thickness variations in single point incremental forming. J of Engineering Manufacture 218:204–210

Zhang GE, Yao J, Jack SH, Wu X (2003) Shrink flanging with surface contours. Journal of Manufacturing Processes 5(2):143 – 153

Zhang H, Zhang Z, Ren H, Cao J, Chen J (2018) Deformation mechanics and failure mode in stretch and shrink flanging by double-sided incremental forming. International Journal of Mechanical Sciences 144:216–222

Zhang Q, Xiao F, Guo H, Li C, Gao L, Guo X, Han W, Bondarev aB (2010) Warm negative incremental forming of magnesium alloy az31 sheet: New lubricating method. Journal of Materials Processing Technology 210:323–329

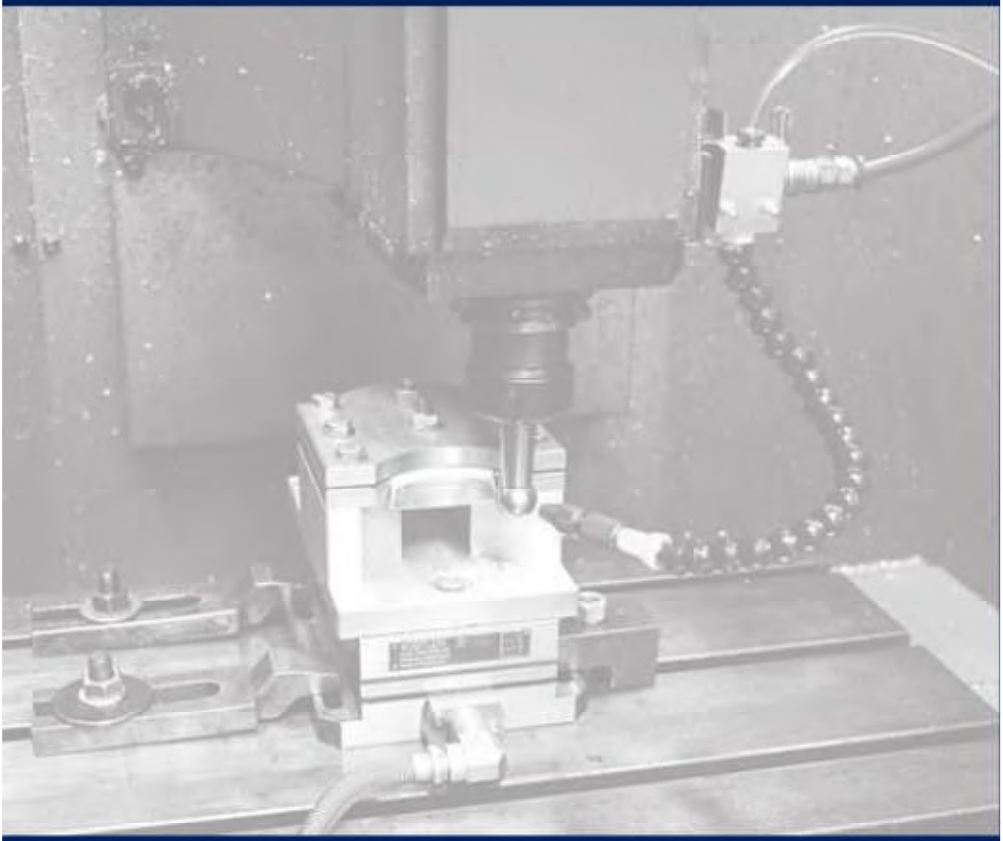

GOBIERNO DE ESPAÑA
MINISTERIO DE ECONOMÍA Y COMPETITIVIDAD

DPI-2015-64047-R